Die approbierte Originalversion dieser Dissertation ist in der Hauptbibliothek der Technischen Universität Wien aufgestellt und zugänglich.
http://www.ub.tuwien.ac.at

The approved original version of this thesis is available at the main library of the Vienna University of Technology.
http://www.ub.tuwien.ac.at/eng

DISSERTATION

A better understanding of the tunnel boring machine as a seismic source for Tunnel Seismic While Drilling

Ausgeführt zum Zwecke der Erlangung des akademischen Grades einer Doktorin der technischen Wissenschaften unter der Leitung von

Em.O.Univ.Prof. Dipl.-Ing. Dr.phil. Ewald Brückl
E120-3
Department für Geodäsie und Geoinformation

eingereicht an der Technischen Universität Wien
Fakultät für Mathematik und Geoinformation

von
DI Ingrid Schlögel
Matrikelnummer 0135109
Schickgasse 25/2/3
1220 Wien

Wien, am 4. September 2015

Abstract

An efficient tunneling requires timely and accurate predictions on the geological situation ahead the tunnel face. Hence, there is a growing demand in the development of geophysical methods to improve the prognosis on changes in the rock such as the occurrence of faults. To this regard, the seismic prediction system Tunnel Seismic While Drilling (TSWD) has been proposed, considering that the cutting process of the tunnel boring machine (TBM) itself is a source of seismic waves. However, the source mechanism underlying the origin of the seismic waves is not well understood. Therefore, within this thesis we analyze datasets collected at different tunnels sites. Here, I demonstrate that an adequate processing of the measured signals provide consistent results for the modeling of the seismic source, independently on the characteristic of the TBM and geology on site.

In this thesis, we investigate the validation of three hypotheses commonly assumed for the processing and interpretation of the seismic data in TSWD: i) the pilot sensor response to an individual event is a minimum delay wavelet; ii) additional seismic sources are neglected such as the reaction forces over the gripper, which are used to fix the TBM to the tunnel walls during drilling; and iii) the radiation pattern of the seismic waves due to the cutting process of the TBM represents a single force mechanism.

To achieve this, an attempt to determine the transfer function is shown to consider the propagation of the source wavelet from the cutter to the used pilot sensor position at the main bearing. The test data are not sufficient to determine the actual transfer function, but criteria are proposed to localize an optimum recording position on the TBM. In case of a second seismic source, it would be then necessary to quantify it for the analysis of the data collected in TSWD. My results reveal that the effect of grippers as a further source can be considered as negligible, however further research is needed to incorporate it in the modeling of seismic waves.

To investigate the source mechanism of the cutting process the seismic radiation pattern was observed at several tunnel sites in Austria, where TSWD was implemented. The data is based on 3-component geophones situated on the surface above the tunnel axis, as well as data recorded in boreholes at the tunnel wall in a two-tube tunnel system. The seismic receivers collected the forward and backward radiated wave field during the tunneling. For the analyses of the source mechanism the polarization of p-waves and s-waves and their amplitude ratio were determined. The observed seismic radiation pattern corresponds mainly to the single force mechanism. Smaller parts, especially p-waves radiated perpendicular to the tunnel axis in vertical direction, are explained by including tensile cracks, which occur during the cutting process.

Kurzfassung

Eine gute geologische Prognose vor der Ortsbrust ist besonders wichtig um einen effizienten Tunnelbau durchzuführen. Daher werden dort derzeit geophysikalische, hauptsächlich seismische, Methoden für die Erkundung von relevanten Strukturen, wie z.B. Störungen, unterstützend eingesetzt. Für den Vortrieb mit einer Tunnelbohrmaschine (TBM) wurde das „System Tunnel Seismic While Drilling“ (TSWD) entwickelt. Grundsätzlich nutzt diese Methode die durch den Schneidprozess generierten seismischen Wellen als kontinuierliche Quelle, die mit seismischen Aufnehmern registriert werden. Der zugrunde liegende Quellmechanismus wird aber bis jetzt aber noch nicht gut verstanden. In dieser Arbeit wurden daher die Daten von verschiedenen Tunnelprojekten analysiert, die in erster Linie zeigen, dass die seismischen Signale unabhängig vom TBM-Typ und der vorhandenen Geologie betrachtet werden können.

In dieser Arbeit werden drei Hypothesen untersucht, die derzeit für die Auswertung und Interpretation der TSWD Daten angenommen werden; i) die Antwort des Pilotsensors auf ein einzelnes Event ist ein Signal mit größter Energie am Anfang (minimum phase); ii) weitere mögliche seismische Quellen, wie die Gripper, die die TBM während des Vortriebs gegen die Tunnelwand stabilisieren, werden vernachlässigt; und iii) die ausgesandten seismischen Wellen des Schneidprozesses der TBM können durch eine Einzelkraft repräsentiert werden.

Um das zu erreichen wurde versucht eine Transferfunktion zu bestimmen, die die Übertragung des ursprünglichen erzeugten Signals an der Ortsbrust zu den Pilotsensoren, die am Hauptlager der TBM angebracht sind, wiedergibt. Die Testergebnisse zeigten, dass die Daten nicht ausreichend sind um die eigentliche Transferfunktion zu bestimmen, aber dadurch eine optimale Aufnahmeposition des Pilotsensors gefunden werden kann. Zusätzlich wurde untersucht, ob beim TBM Vortrieb eine zweite seismische Quelle wirksam ist, die bei der Analyse von TSWD eine Rolle spielt. Die Ergebnisse meiner Arbeit zeigen, dass für die bisherigen TSWD Anwendungen der Gripper als weitere Quelle vernachlässigt werden kann. Dies gehört jedoch weiter untersucht um in eine seismische Wellenmodellierung miteinbezogen werden zu können.

Für ein genaueres Verständnis vom Quellmechanismus des Schneidprozesses der TBM, wurde an verschiedenen Tunnelbaustellen in Österreich, wo TSWD eingesetzt wurde, das seismische Wellenfeld beobachtet. Daten von 3-Komponenten Geophone, die an der Oberfläche über der Tunnelachse platziert waren und von Bohrlochgeophonen, die in den Ulmen eines zweiröhrigen Tunnelsystems installiert waren, wurden gesammelt. Die seismischen Aufnehmer registrierten das nach vorne und nach hinten abgestrahlte Wellenfeld während des Tunnelvortriebs. Zur Analyse des Mechanismus

wurden für jeden Aufnehmer die Polarisation der P-Welle und der S-Welle und deren Amplitudenverhältnisse bestimmt. Diese zeigte, dass die Abstrahlcharakteristik überwiegend einem Einzelkraftmechanismus entspricht, aber auch geringfügige Anteile aufweist, die damit nicht erklärt werden können. Im speziellen treten P-wellen auf, die senkrecht zur Tunnelachse in vertikaler Richtung abgestrahlt werden. Diese werden durch das Hinzufügen von Zugrissen, die durch den Schneidprozess erzeugt werden, erklärt.

Acknowledgment

I want to thank the people, who supported me during the time, who helped me to go further and finally brought me to an end of this work.

I appreciate the time under the guidance of Prof. Brückl. His comments, advices and careful discussion were very helpful to go on in the work.

The field work would have been more difficult, without the assistance of the colleagues from Pöyry Infra GmbH. I want to thank the whole team for their great support at the tunnel sites.

Here, also Toni Lettenpichler has to be mentioned, who always had time and good advise for problems with the equipment.

Furthermore, I want to thank all former and active colleagues of the research group Geophysics. The technical discussions and the small talks were essential for the advance of my work, special thanks here to Werner Chwatal.

My stay at Colorado School of Mines was a great time. I want to thank Prof. Mooney, who made this possible and supported me during this time.

The love, encouragement and patience of my husband Günter guided me during this time.

Last but not least I want to thank Peter Lettenpichler, the little son of Toni Lettenpichler. He gave me the following great picture of a TBM at the beginning of the thesis, that accompanied me the whole time.

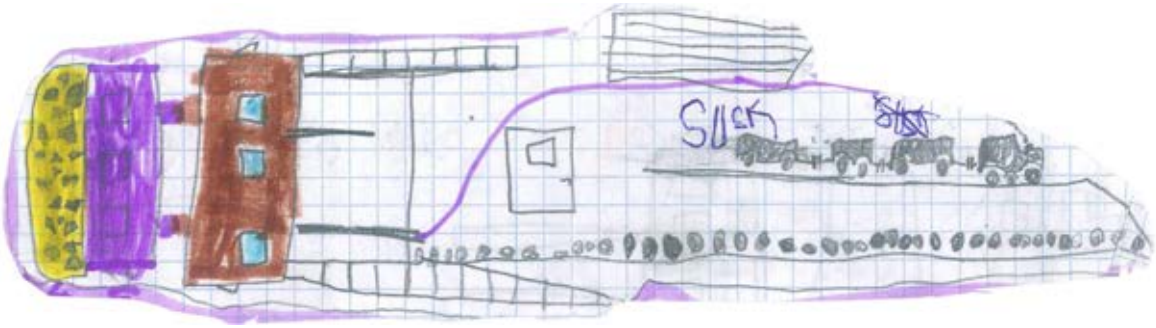

Contents

1. Introduction **1**

1.1. Seismic prediction systems in tunnels 2

1.2. Tunneling with tunnel boring machines (TBM) 5

1.3. Tunnel Seismic While Drilling (TSWD): concepts and limitations . . . 7

1.4. Thesis objectives 13

2. TSWD method **16**

2.1. Geometrical layout 17

2.2. Pilot Signal 18

2.3. Receiver signal and comparison with the pilot signal 22

2.4. Timing and positioning 24

2.5. Routine processing 25

2.5.1. Detection of times with active TBM 25

2.5.2. Minimum delay transformation 26

2.5.3. Determination of wave velocities 32

2.5.4. Removal of direct wave field 32

2.6. Interpretation 33

2.6.1. Prediction and classification 33

2.6.2. Examples 36

3. Closer inspection of the pilot sensor signal **39**

3.1. Criteria for the position of pilot sensors 39

3.2. Attempt to determine transfer function 43

4. Gripper as a possible seismic source **45**

4.1. Description and comparison of sensor signals 45

4.2. Comparison of the forward and backward recorded p-wavelet 46

5. Cutting process - the main seismic source **49**

5.1. Rock fragmentation models 49

5.2. Cutter force measurements 52

6. Observation of radiation pattern **55**

6.1. Receiver locations 55

6.2. Ray paths . . . 58
6.2.1. Definition of angles between the TBM and receiver position . . 58
6.2.2. Consideration of a weathered surface layer . . . 59
6.2.3. Rotation into of p- and s-wave directions . . . 60
6.2.4. Receiver position projected to focal sphere . . . 61
6.3. First break picking . . . 63
6.4. Seismograms of rotated field data with first breaks . . . 65
6.5. Polarization . . . 73
6.6. Amplitude Ratio P-wave to S-wave (P/S ratio) . . . 76

7. Analysis of source mechanism **80**
7.1. Description of the radiation pattern by single force . . . 80
7.1.1. Measured and calculated displacements . . . 83
7.2. Additional effect of tensile fractures . . . 85
7.2.1. Attempt to determine crack size . . . 92

8. Discussion **94**

9. Conclusions and outlook **99**

Appendix A. Original frequency spectrum of receiver signals **101**

Appendix B. Minimum delay transformation with gripper components **104**

Appendix C. First break picking **107**

Appendix D. Correlation with common wavelet **110**

List of Figures

1.1. VSP principle in tunnel 2
1.2. TSP Geometry 3
1.3. Principle of the RSSR migration 3
1.4. Prediction uncertainty 4
1.5. Gripper TBM 6
1.6. Double Shield TBM 7
1.7. Pilot signal and receiver signal 8
1.8. Scheme of TSWD 9
1.9. Generation of conventional seismic trace 11
1.10. Schematic image of seismic waves producing the same reflection 12

2.1. Map of Austria with construction sites 16
2.2. Geometrical layout TSWD 18
2.3. Cross view of TBM head Koralm with position metal cube 19
2.4. Accelerometers on TBM head 19
2.5. Autocorrelation of pilot sensors 20
2.6. Frequency spectra of pilot sensors on main bearing 21
2.7. Direction of geophone components 22
2.8. Detection of active TBM times 25
2.9. Comparison of frequency spectrum at geophone 28
2.10. Processed traces with axial pilot sensor and frequencies of cross section MQ11-Reisseck 29
2.11. Processed traces with axial pilot sensor and frequencies of cross section MQ39-Koralm 30
2.12. Processed traces with radial pilot sensor and frequencies of cross section MQ39-Koralm 31
2.13. Binning of traces and resulting reflections 32
2.14. Mapping of reflections 33
2.15. Daily update of the results 35
2.16. Prediction example of Koralm 37
2.17. Prediction example of fault zone with 60m 37
2.18. Prediction example of fault zone with 1m 38
2.19. Prediction example of Bärenwerk 38

3.1. Test at Bärenwerk: stroke points and receiver points on cutter head . . 41
3.2. Recorded signal and frequency spectrum of stroke test; Bärenwerk . . . 41
3.3. Test at Koralm: stroke points and receiver points on cutter head 42
3.4. Recorded signal and frequency spectrum of stroke test; Koralm 42
3.5. Estimation ofthe transfer function at Bärenwerk 43

4.1. Position of pilot sensors on Gripper TBM at Reisseck 45
4.2. Amplitude relations pilot sensors at Reisseck 46
4.3. Frequncy content of pilot sensors Reisseck 46
4.4. P-wavelet of forward and backward wave field 47

5.1. Scheme of cutting process 50
5.2. Measured forces during cutting process 53
5.3. Measured normal forces at Koralm TBM 53

6.1. Position of surface station and tunnel axis Reisseck 56
6.2. Position of surface station and tunnel axis Bärenwerk 57
6.3. Position of surface station and tunnel axis Koralm 57
6.4. Position of borehole station and tunnel axis Koralm 58
6.5. Definition of angles Theta and Phi 59
6.6. Influence of a weathered layer on ray paths 60
6.7. Definition of p-wave and s-wave direction of motion 61
6.8. Determination of angle Delta and Epsilon 62
6.9. Measured sections plotted on sphere with radius 1 62
6.10. First break picking of p-wave and s-wave 64
6.11. Seismograms of MQ40 - Koralm 67
6.12. Seismograms of MQ39 - Koralm 68
6.13. Seismograms of MQ41 - Koralm 69
6.14. Seismograms of HOTE - Reisseck 70
6.15. Seismograms of CUBE - Bärenwerk 71
6.16. Seismograms of OBEN - Koralm 72
6.17. Determination of polarization by correlation with common wavelet . . . 73
6.18. Correlation factor of polarization 75
6.19. Deleting of noisy data 76
6.20. Correction of P/S ratio 78
6.21. P/S amplitude ratio for all receivers 79

7.1. Radiation pattern p-wave and s-wave for single force 81
7.2. Amplitude values and P/S ratio over delta of a single force 82

7.3. Comparison P/S ratio of field data to model of single force 83
7.4. The body-force equivalent for a tension fracture in an isotropic medium 86
7.5. Radiation pattern p-wave and s-wave tensile fracture 87
7.6. Amplitude values and P/S ratio over delta for tensile fracture 88
7.7. Different P/S amplitude ratios including tensile fractures in various directions 89
7.8. P/S amplitude ratio of measured data and several models 90
7.9. Amplitudes of p-wave and s-wave of the forward radiated wave field . . 91
7.10. P/S amplitude ratio of measured data and several models on focal sphere 92

8.1. Number of values over Delta 96

A.1. Frequency spectrum of receiver stations at Reisseck - MQ11 101
A.2. Frequency spectrum of receiver stations at Reisseck - MQ10 101
A.3. Frequency spectrum of receiver stations at Reisseck- HOTE 102
A.4. Frequency spectrum of receiver stations at Reisseck- MQ09 102
A.5. Frequency spectrum of receiver stations at Koralm - MQ39 102
A.6. Frequency spectrum of receiver stations at Reisseck - MQ40 103
A.7. Frequency spectrum of receiver stations at Koralm - MQ40a 103
A.8. Frequency spectrum of receiver stations at Koralm - MQ41 103

B.1. Processed data with axial pilot sensor on gripper and frequencies of cross section MQ11-Reisseck 105
B.2. Processed data with radial pilot sensor on gripper and frequencies of cross section MQ11-Reisseck 106

C.1. sta/lta ratio of receiver stations MQ39 108
C.2. sta/lta ratio of receiver stations MQ41 108
C.3. sta/lta ratio of receiver stations CUBE 109
C.4. sta/lta ratio of receiver stations OBEN 109

D.1. Correlation with common wavelet of receiver stations MQ39 111
D.2. Correlation with common wavelet of receiver stations MQ41 111
D.3. Correlation with common wavelet of receiver stations CUBE 112
D.4. Correlation with common wavelet of receiver stations OBEN 112

List of Tables

2.1. List of construction sites 17
2.2. Frequencies Reisseck 23
2.3. Frequencies Koralm 24
2.4. Classification scheme 36

7.1. Calculated and measured displacement due to force 84

1. Introduction

In recent years tunneling with a Tunnel Boring Machine (TBM) became one of the main techniques applied for hard rock and soft ground tunneling worldwide. An excellent geotechnical prognosis is important on each tunnel site in order to prevent high costs in case of a failure and also damages to the machine and the operating staff in the tunnel. Geological and geophysical investigations, as well as drilling before tunneling have brought the quality of geotechnical prognosis to a high standard. However, the remaining risk during tunnel construction is still considerable. It is difficult to access the tunnel face for a geological prediction, moreover, drilling is expensive and time consuming. Thus, geophysical methods are good tools to support the prediction of geological and geotechnical risks in front of the tunnel face.

One such powerful technique is seismic imaging ahead of a tunnel face, which is based on vertical seismic profiling (VSP). This method has been developed in the field of hydrocarbon exploration and uses seismic wave fields generated by surface-sources and observed by geophone arrays in boreholes. By separation of down-going and up-going (reflected) wave fields, high resolution information about seismic velocities along the borehole and reflectors below the borehole can be achieved. These features make VSP a successful tool frequently used for detailed exploration of geological structures in the vicinity of and below a borehole.

The application of VSP to the prediction ahead of a tunnel is obvious: The vertical axis of the borehole is rotated to the (more or less) horizontal tunnel axis, the borehole is represented by the tunnel. Either there are many source locations at different tunnel chainages and few receivers the tunnel wall, or reverse. Figure 1.1 shows the physical principle and the field geometry. Three-component geophones are installed in boreholes on several cross-sections (receivers). The source points are along the tunnel axis in front of the geophone cross-sections. The recorded data contains the generated seismic waves (compressional wave = p-wave, shear wave = s-wave and tubes / or Rayleigh wave along the tunnel wall), which propagate directly back to the receivers and p- and s-waves, which are reflected at seismic impedance (seismic wave velocity x density) changes in front of the tunnel face. Different seismic impedance can, therefore, be related to fault zones, changing rock quality, fractured rocks, cavities, joints, and lithology changes. These changes can be accompanied by possible severe water inflow, which pose a risk for tunneling. The range of prediction is about 100 - 200 m ahead of the tunnel face. As the TBM moves on, the layout of the measurements moves on.

This method has been carried out over the last 20 years in tunnels with a conventional heading, but also in tunneling with a TBM (e.g.,Brückl et al. (2001)).

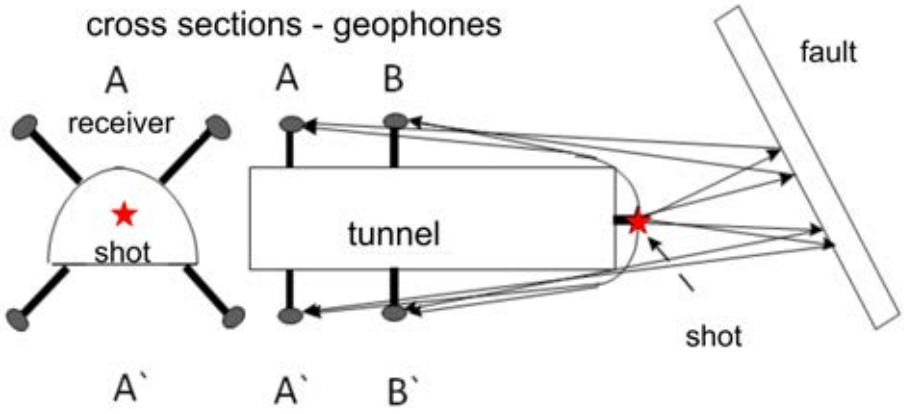

Figure 1.1.: Physical principle and field geometry of a tunnel VSP (Brückl et al., 2001)

1.1. Seismic prediction systems in tunnels

Several commercial products exist, which use this general layout for the prediction in hard rock with conventional and mechanized tunneling, such as: TSP - Tunnel Seismic Prediction (Dickmann, 2005), ISIS - Integrated Seismic Imaging System (Giese et al., 2002) and TRUST – True Reflection Underground Seismic Technique (Benecke et al., 2008). In addition, a system for boulder detection in soft ground, referred to as SSP - Sonic Softground Probing was developed by Kneib et al. (2000) and further improved by Gehring et al. (2010).

In the case of blasting several boreholes with a depth of 2-5 m are made in the tunnel wall (Dickmann, 2008). For the ISIS method, pneumatic hammers are installed on the grippers of the TBM (Lüth et al., 2008). Figure 1.2 illustrates only the interested wavefronts as parts of the full spherically spreading waves. The sources for TRUST are either blasts or special mechanical sources (vibrators), which are situated also in front of the geophone cross-sections (Benecke et al., 2008). TSP and TRUST makes use of the full spherically spreading waves from the blasting and evaluate the reflections of the p-wave and s-waves.

The ISIS method also observe Rayleigh-waves traveling along the tunnel lining which are converted at the tunnel face into s-waves. The reflected s-waves are again converted into Rayleigh-waves (Lorang et al., 2005; Bohlen et al., 2007) and registered. Figure

Figure 1.2.: TSP: Measurement layout of the 3D Tunnel Seismic Prediction method consisting of usually 4 receivers (RCV) and 24 shot points. (Dickmann and Krueger, 2014)

1.3 shows the wave path for a converted and reflected s-wave (RSSR). Further improvements in the seismic processing have been achieved by the implementation of the so-called Fresnel-migration (Buske et al., 2006), which allows a better spatial resolution of the seismic image of reflecting interfaces.

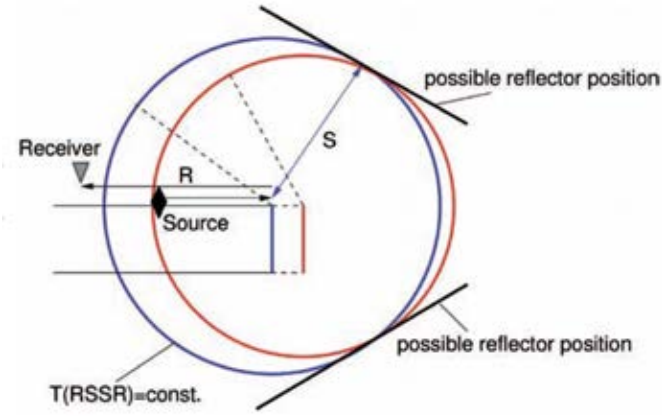

Figure 1.3.: Principle of the RSSR migration assuming two different tunnel face positions. The seismic source (black diamond) and the receiver (inverted triangle) can operate at a fixed location. The ray paths for an RSSR reflection are shown for the first tunnel face position (blue line): Black arrows indicate Rayleigh waves, blue arrows indicate s-waves. The isochrone of a RSSR reflection is represented by a circle around the edge of the tunnel face on the side of the source-receiver profile. (Lüth et al., 2005)

All these systems process the data according to the VSP-method by separation of the direct and reflected wave field. The velocity field of the direct wave field is determined by picking and analyzing the traveltimes of the first arrivals. Aligning these traveltimes horizontally (i.e. to a constant time), the direct wave field can be

eliminated by horizontal subtraction of a mean or by (f,k) filtering (Hardage, 2000).

The results of the methods provide a 2D or 3D overview of the reflections within the predicted distance (up to 150 m). TSP also include charts of computed rock mechanical properties within the prediction area. It exploits the information in the seismic wave field by separate p-wave and s-wave analysis and the 3D-Velocity based Migration and Reflector Extraction technology (3D-VMR). The 3D-VMR technology provides an adequate and detailed 3D image of the ground leading to a more reliable interpretation compared to conventional 2D approaches (Dickmann and Krueger, 2013).

A disadvantage of these systems is the stopping of the TBM for every measurement, which causes a slowing down of the heading. The processing of the data can most times be done by an outside expert. And as there are long intervals between the measurements, no continuous image of the reflection is available. Another fundamental problem is that there is a strong spatial ambiguity for the location of the reflectors (fault zones, petrologic boundaries, or similar). Figure 1.4 shows this problem of extrapolation for an inclined fault zone where the predicted intersection (dashed green line) is different to the real intersection (solid green line). Only reflecting horizons which intersect a straight tunnel axis orthogonally are imaged at their true intersection with the tunnel axis. Thus imposes major uncertainties on prediction (see Figure 1.4).

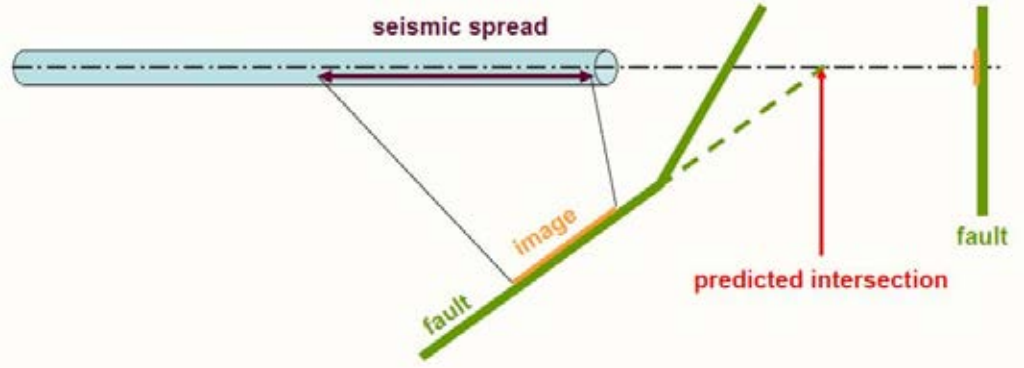

Figure 1.4.: Imaging the intersection with the tunnel axis imposes major uncertainties on prediction in case that the reflector has no continuous trend or is not perpendicular to the tunnel axis.

Both uncertainties of seismic prediction could be overcome by continuous recording of the seismic data. This allows a more efficient prediction regarding the uncertainties even without disturbing the heading. Real time processing and continuous update of prediction helps to reduce risks and, therefore, save money.

1.2. Tunneling with tunnel boring machines (TBM)

The use of tunnel boring machines (TBM) is one of main construction methods as tunnels are becoming longer and are used more frequently in urban regions. In contrast to conventional methods such as the New Austrian Tunneling Method (NATM), mechanized tunneling tends to be faster although the capability to cope with heterogeneous ground conditions is less. In soft ground modern TBMs are able to excavate at shallow depths underneath sensitive infrastructure even in poor ground conditions. A conventional TBM is a highly engineered unit that has to cope with various duties. The following description and figures of the TBM is based on the website of Herrenknecht.

In hard rock three main types of TBMs are used:

- Gripper TBM (open type)
- Single Shield TBM
- Double Shield TBM

Gripper TBM:
Before each stroke, the Gripper TBM is braced against the previously excavated tunnel with the laterally mounted gripper (Figure 1.5). Thrust cylinders are braced against the gripper unit and push the rotating cutterhead against the tunnel face. Buckets in the gauge area of the cutterhead are used to pick up excavated material and feed a machine belt which is placed right behind the cutterhead. Several shields stabilize the machine against vibrations during the boring process. The roof shield above offers protection against breaking rock cover also the main bearing of the TBM. After completion of a stroke, tunneling is interrupted and the gripping unit is moved forward.

Single shield TBM:
This kind of TBM moves forward using hydraulic jacks that thrust against prefabricated segment lining. A shield that overlaps on the lining segments provides safety against loose boulders and squeezing rock conditions. Steering is primarily done by controlling the jacking force between different set of thrust jacks.

Double shield TBM:
The double shield TBM combines the elements of a single shield TBM with a gripper TBM. It consists of two main components (Figure 1.6): a front shield with cutterhead, main bearing and drive, and a gripper shield with gripping unit and auxiliary thrust cylinders. The main thrust cylinders connect the two parts of the shield. They are

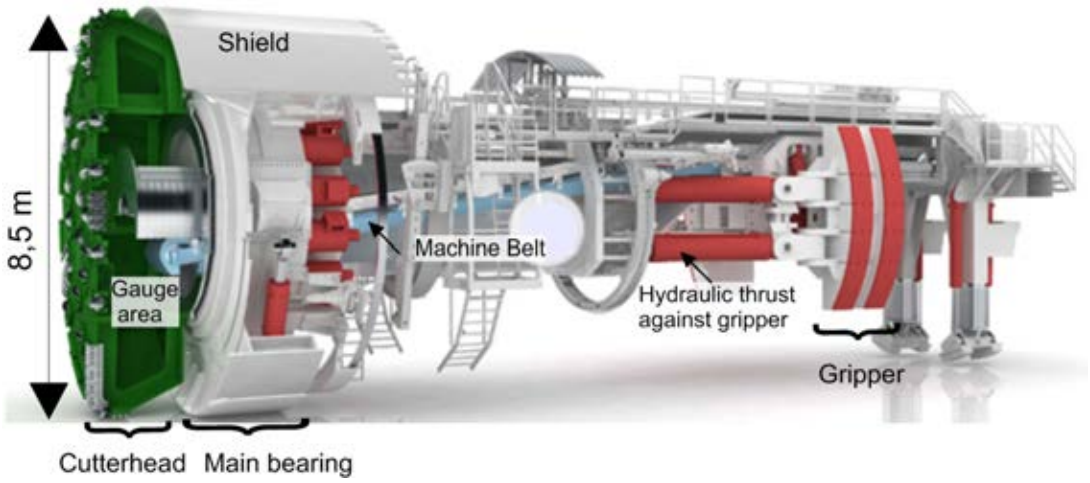

Figure 1.5.: Gripper TBM @ Herrenknecht.com

protected by the telescopic shield where the shield skins of the front and gripper shield overlap. In stable rock, the machine is braced radially against the tunnel with the gripper. When conditions get worse, it can be changed to a single shield arrangement (by locking front and gripper shield) and moving forward by pressing against segmental lining.

The reaction forces during the excavation process are transferred into the rock by the extended gripper. Simultaneously to tunneling, the segments are installed with the erector. The auxiliary thrust cylinders serve only to secure the position of the concrete segments placed. When the stroke is completed, the grippers are loosened and the gripper shield is pushed behind the front shield using the auxiliary thrust cylinders. Regripping lasts only a few minutes, which means that tunneling is almost continuous.

The main advantage of the double shield machine is the faster advance rate. When shoving forward in stable rock, the double shield machine can excavate rock and simultaneously erect the lining, which can lead to great time savings compared to the single shield machine.

The cutterhead is a rigid steel structure that supports the cutters and loads the muck onto a belt conveyor. Depending on machine size and site conditions, the cutterhead can be one piece or of sectional design. Replacement of worn discs on the cutterhead is performed by replacing the cutters held in special saddles by bolts or a wedge lock system.

Disc cutters have an important role in tunnel boring including the layout of cutters on the cutterhead (kerf spacing) and the shape of the cutterhead itself. The steel disc rings are mounted on a hub assembly, which comprises the bearing and seal arrangement. Cutter life varies extensively depending on the rock type and especially on its quartz

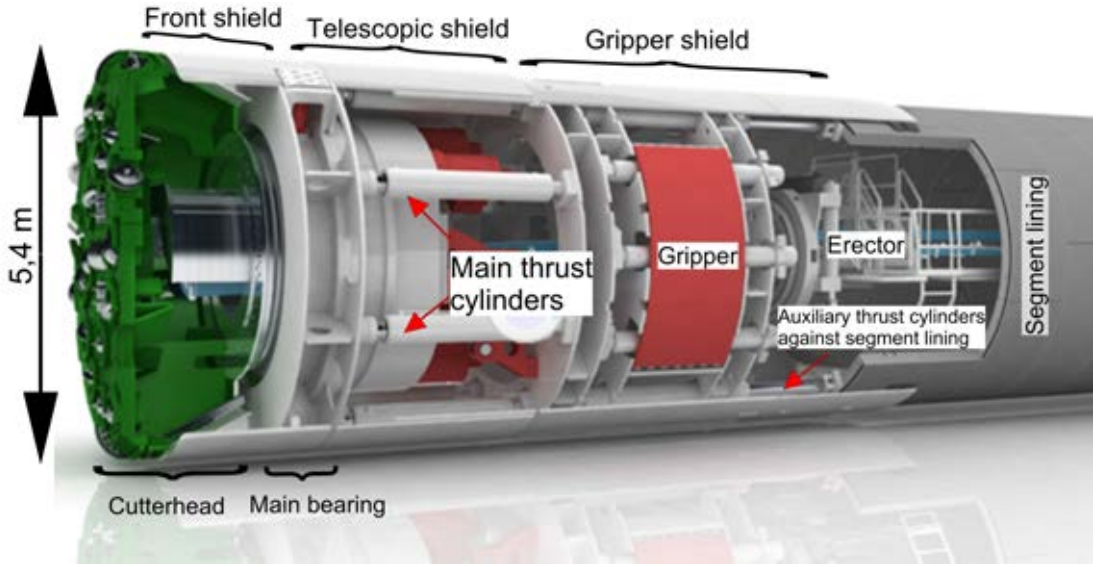

Figure 1.6.: Double Shield TBM @ Herrenknecht.com

content. The most popular disc shape today is the "constant section" ring, which means the disc footprint does not change significantly with wear ((Heinö, 1999). By pressing and rotating the cutters against the tunnel face they fragment the rock by forming chips. A more detailed description of this chipping process is given in Chapter 5 - Cutting process -the main seismic source.

1.3. Tunnel Seismic While Drilling (TSWD): concepts and limitations

The high penetration rate of a TBM (20-50 m/day) and therefore the need for a quick seismic acquisition tool has led to use the vibrations as a seismic source, which are produced at the cutterhead of the TBM (Petronio and Poletto, 2002). This method is based on results of the SWD - Seismic While Drilling (Poletto and Miranda, 2004) and named as "Tunnel Seismic While Drilling – TSWD" (Petronio et al., 2003). They installed a sensor on the TBM to measure the seismic noise of the TBM (pilot signal). The wave fields were recorded by sensors outside of the tunnel. The TBM produced energetic vibrations, which could be detected at offsets greater than 700 m. The cross correlation between the pilot signal and the data at the seismic stations showed coherent events, corresponding to p-and s-wave arrivals. They stated that the reflections ahead of the TBM cutting face can be detected to indicate the presence of lithological changes and or rock properties variations.

In a first research project in 2008, operated by the TU Wien and the company

Pöyry Infra GmbH, TSWD was implemented on a hard rock TBM at the gallery at Hieflau, Austria. Thereby the pilot signal was recorded with three-component (3C) accelerometers on the non-rotating part at the main bearing with a sampling frequency of 1000 Hz. The receiver sensors (two 3C borehole geophones) with 15 Hz natural frequency were installed in 5 and 10m deep boreholes at the right and left side wall of the gallery along one cross-section (Brückl et al., 2008). Figure 1.7 show the traces of the recorded pilot and receiver signal over 20 minutes. It can be clearly seen, when the TBM was moving forward.

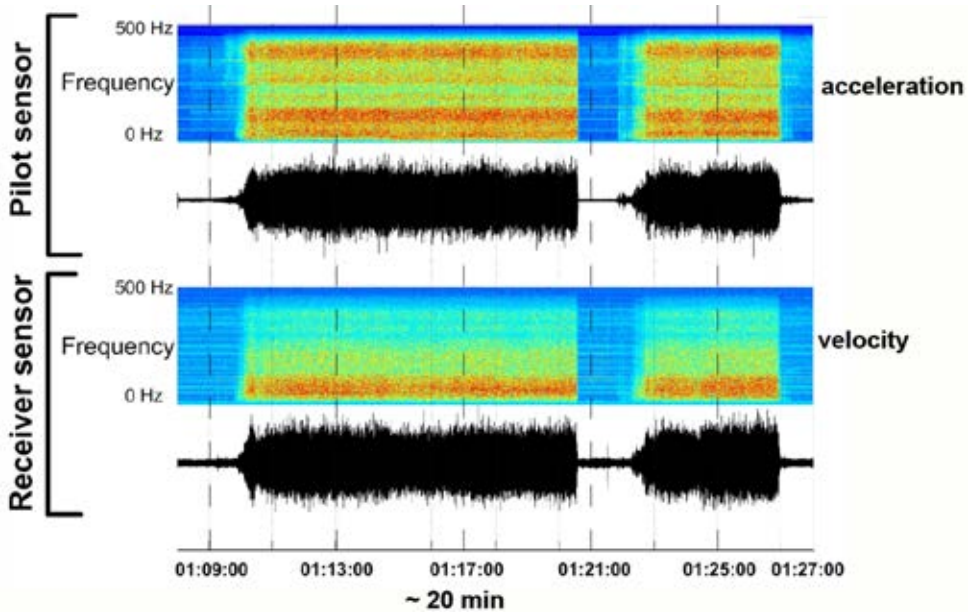

Figure 1.7.: The upper trace is the recorded signal of an accelerometer (pilot signal Sp), the lower trace is the recorded signal at an axial geophone (receiver signal Sr) over 20 min; the frequency content is shown above the traces.

A simplified sketch of TSWD is shown in Figure 1.8. It shows the position of the pilot sensor and receivers behind the TBM. For the prediction the reflected wave field (blue-red images) of receivers in the left and right tunnel wall, after elimination of the direct waves arrivals, are plotted along the tunnel axis. High amplitudes of reflections indicate changes in the rock properties within a prediction distance of 150 m.

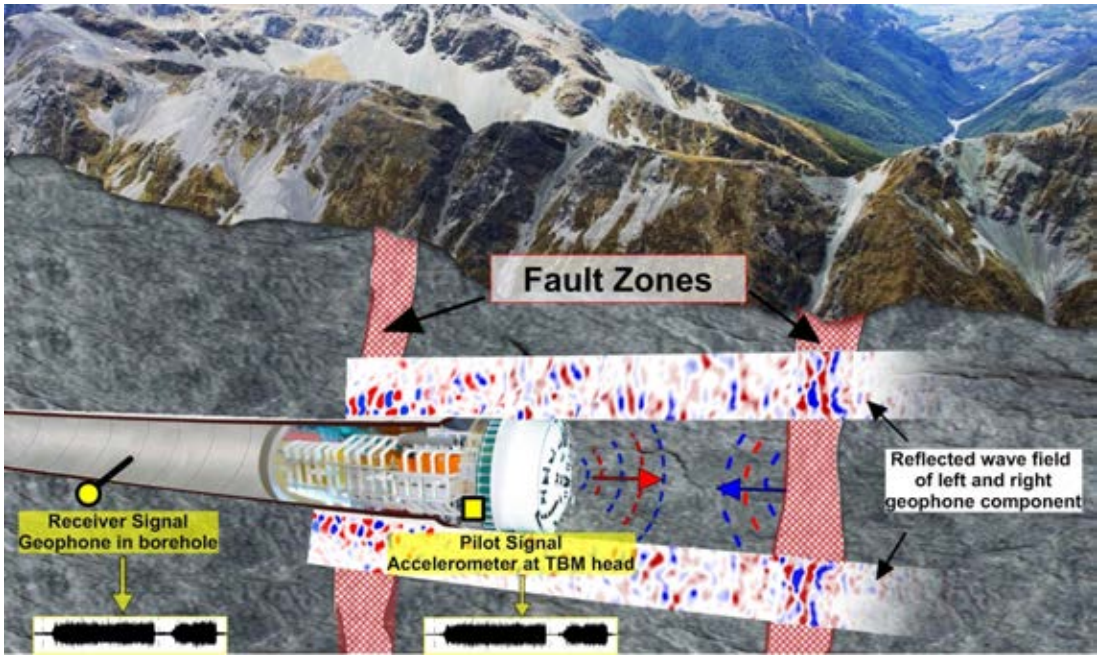

Figure 1.8.: Scheme of Tunnel Seismic While Drilling: Sensors at the TBM head collect continuously the pilot signal (yellow box); Geophones behind the TBM (yellow circle) collect the whole wave field (direct and reflected waves). With the resulting reflected wave field a prediction for changes in rock properties (e.g. fault zones) is possible until 150 m ahead of the TBM.

Generation of conventional seismic traces

The standard method to derive interpretable seismograms from this data is the correlation between the pilot- and the receiver signal (Poletto and Miranda (2004)). However an alternative method is applied, which is based on the assumption that the pilot signal (Sp) is a minimum phase wavelet (P) convolved with a random sequence of spikes (I). After calculation of the minimum delay transformation of the pilot signal, the filter is applied to the receiver signal (Sr) (Brückl et al., 2008).

The relations between the measured data (Sp and Sr) and a conventional seismic trace (T) are (equations corresponding to the frequency domain):

$$Sp = I \cdot P \tag{1.1}$$

$$Sr = I \cdot W \cdot G \cdot R = Sp \cdot P^{-1} \cdot W \cdot G \cdot R \tag{1.2}$$

$$T = W \cdot G \cdot R = Sr \cdot I^{-1} \tag{1.3}$$

$$\mathbf{T} = \mathbf{Sr} \cdot (\mathbf{Sp^{-1}} \cdot \mathbf{P}) \tag{1.4}$$

$(Sp^{-1} \cdot P)$ ... minimum delay filter
Sp ... recorded pilot signal;
Sr ... recorded receiver signal;
I ... Time sequence of impulses corresponding to initiated source wavelets produced by the cutting process;
P ... Pilot sensor response; transfered source wavelet of an individual impulse (assumed to be minimum phased);
G ... Green's function from source at tunnel face to distant receiver;
W ... Seismic source wavelet produced by cutting process at the tunnel face;
R ... Receiver sensor response;
T ... Conventional seismic trace.

As P is assumed to be minimum phase following calculations are done to obtain the seismic trace T out of 32 seconds recorded signal:
- Estimate the amplitude spectrum of the P-wavelet by using the autocorrelation of the pilot signal Sp
- Compute the phase spectrum of the P-wavelet through the Hilbert transformation of the power spectrum
- Compute the minimum delay filter ($Sp^{-1} \cdot P$)
- Filter the receiver signal Sr to obtain the seismic trace: $T = Sr \cdot (Sp^{-1} \cdot P)$ In the following chapters this process is named a minimum delay transformation.

Figure 1.9 shows explicit the steps of a 32 second long recorded signal to the conventional seismic trace.

The resulted seismograms contained signals with frequencies up to 200 Hz and the signal to noise ratio was excellent up to the maximum source-receiver distance of about 1 km. The wavelet of the first arrival has a nearly constant shape regardless of the source-receiver distance and it was not influenced by the very different geologic conditions. The first arrivals could be removed almost completely from the data and reflected signals could be traced from about 200 m to less than 10 m ahead of the TBM drilling head. This new achievement implied a significant reduction in prediction uncertainty. It could be shown that the TSWD-method is working excellent for the prediction of fault zones (Brückl et al., 2010).

Within this study the recording units were not synchronized in time and no prediction in time was done. However, it was the basis for a continuous applications with nearly real time prediction in several tunnels in Austria.

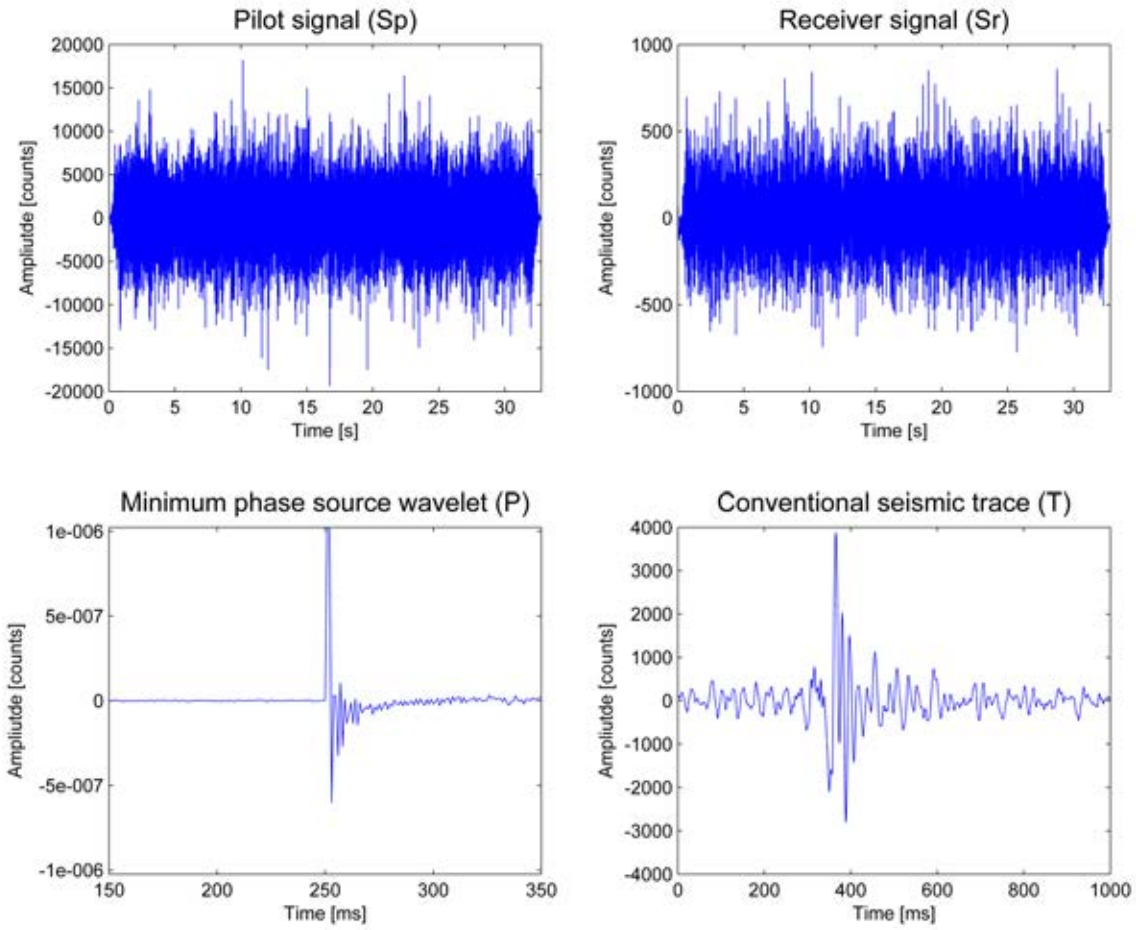

Figure 1.9.: Generation of a conventional seismic trace T: the continuous signals are cut in sections of 32 seconds. For this time section the minimum phase source wavelet P is generated and the receiver signal Sr is filtered with P/Sp.

Limitations

The major restriction of the interpretation accuracy is the frequency range (< 400 Hz) of the recorded pilot signal (Chwatal et al., 2011). This limits the spatial resolution, which is usually $\frac{1}{4}$ of the spatial wavelength, and therefore the information of the thickness of the predicted fault zones. Results of the first numerical modeling efforts show that the beginning of fault zones can be detected for small thicknesses, but the thickness itself has to be unassigned. Seismic traces with a maximum frequency content of 100 Hz resolve the thickness of faults only if they are wider than 20 m (Rabensteiner, 2012).

For the current positions and construction of the pilot sensors, the main signal frequency content is mostly smaller than 400 Hz, for the recorded geophone it is smaller than 150 Hz. Therefore the accuracy of the prediction is about 10 m for the beginning of structures.

Other problems are non-orthogonally faults: dip angles with more than 60°are difficult to detect, because for flat reflections the separation of reflected wave field from first arrivals becomes less efficient.

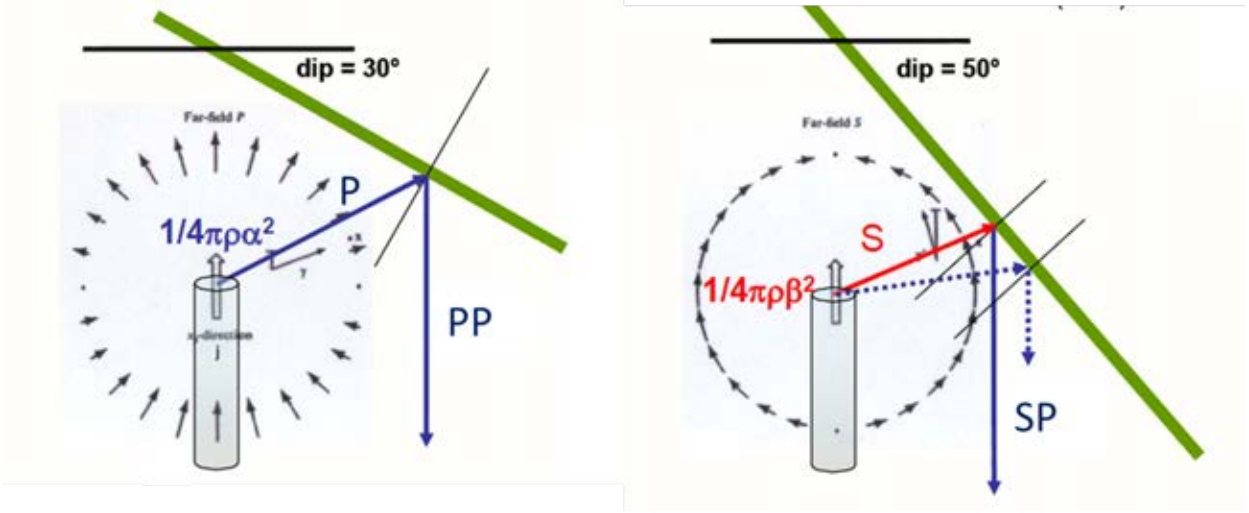

Figure 1.10.: Schematic images (top view) of different seismic waves producing the same reflection, the shown far field radiation pattern is a single force model after Aki and Richards (2002); PP-reflection of boundary with a dip of 30°(left side): SP-reflection of boundary with a dip of 50°(right side).

Another uncertainty comes from the propagation of different waves generated by the source. It is possible that an observed reflection is coming from a PP-reflection (p-

wave is reflected as p-wave) and/or from a SP converted reflection (s-wave is reflected as p-wave) at the same distance but with a different dip (Figure 1.10). This kinematic ambiguity can lead to a wrong interpretation of the dip, but hence to an incorrect intersection with the tunnel axis (Chwatal et al., 2011).

1.4. Thesis objectives

At the begin of the work, November 2011, the company Pöyry Infra GmbH implemented TSWD at a hydro power plant at Reisseck. Two further projects at Bärenwerk and Koralm followed. First aims were to find an adequate geometrical layout, optimum handling of the data (data transmission and processing) and a useful presentation of the results. The processing had to be partly automated to make it faster. Another task was to synchronize the data in time, which was technically difficult in long tunnels (> 3 km). In Chapter 2 - TSWD method - the different projects are described, including the state of the art in layout, timing, processing and results.

For the processing and interpretation of TSWD, the following hypothesis and assumption have been made so far (Brückl et al., 2010):

- The TBM cutterhead, like a drill-bit, represents a single force source that generates compression p-waves in forward and dilation p-waves in backward direction of the tunnel (Poletto and Miranda, 2004).
- The pilot sensor response to an individual seismic event at the tunnel face is a minimum delay wavelet.

And further, simplifications were made:

- Other source locations, such as the gripper, are not considered until now.

Since the usable wave lengths of the seismic waves are larger than the tunnel diameter, the tunnel itself is neglected. These adjustments are not compulsive for every TBM and rock condition and until now have not been investigated.

The assumption that the pilot sensor response (P) is a minimum delay wavelet, has a big impact on the interpretation (begin of structures) and polarity of the reflections. Therefore a further focus in this thesis is set on the pilot signal. It is essential to know how good the recorded pilot signal represents the entire source process. Considering that the origin of the vibrations are the cutters, there must be an influence by the TBM

itself, which brings the signal to the registration unit. Within the scope of this work, the pilot signals of the different applications of TSWD are analyzed (see Chapter 2.2 - TSWD method). Through tests on the TBM an optimum recording position on the TBM can be found. An attempt to determine a transfer function to the pilot sensor location is also shown.

Grippers connect the TBM with the surrounding rock and transmit the reaction forces during drilling into the rock. They are a possible further seismic source. The signal of sensors on the grippers are described and their role as a source is discussed.

The focus at this thesis is to prove the hypotheses of a single force mechanism is true, has to be adapted, or dismissed. The objective is to gain a better understanding and characterization of the TBM itself as a seismic source.

The main goal of TSWD processing is to produce interpretable seismic traces, which can be efficiently managed. Hereby, the quality of the seismic traces and interpretation mainly depends on the knowledge of the source function and the corresponding radiation pattern of the seismic waves in all directions. The uncertainties regarding the resolution, thickness or ambiguous wave paths can be eliminated by modeling seismic images of different types of faults and changing conditions in front of the tunnel face.

Several specific questions regarding the source should be answered in this thesis:

- How does the radiation pattern of a TBM look like, and is it comparable to the pattern of a single force mechanism?
- What are the source mechanism of the seismic signals and how can they related to the drilling process?

These questions can be answered by measuring and analyzing the seismic signals of a working TBM. Thereby it is important to register the forward and backward radiated wave field. This data is gained by measurements of 3-component geophones, which were installed at the surface and situated directly above the tunnel axes with a lateral offset. In addition, data from borehole geophones in the wall of one tube in a two-tube tunnel could be used. The data sets contain the forward and backward radiated wave field, as the TBM in the other tube passes their positions. Based on these data sets the spatial distribution of the polarization and amplitude ratio of p-waves and s-waves can be determined to characterize the radiation pattern.

The general consideration is that the source of the seismic waves is the cutting process, whereby cutters on the TBM head are pressed against the tunnel face and rotated to split the rock. This cutting process generates seismic waves radiating into

the rock mass and vibrations propagating to the main bearing. The vibrations can be efficiently measured at the main bearing and used as the pilot signal.

The literature research related to the cutting process will address/determine different possible source mechanisms. Their characteristic radiation patterns (also including the proposed source mechanisms - single force) are modeled and described. The analysis of source mechanism is based on the comparison of the field data with the modeled ones.

This work was not part of an official financed research project. However, I was strongly supported by the company Pöyry Infra GmbH. I was allowed to use the data and partly the equipment to make measurements only in the framework of their TSWD projects and the approval of their clients. The time and access to the tunnel was limited during the projects, as it was not allowed for monetary reasons to stop or interfere with the drilling activities. Dependent on the given project situation the measurements were organized as best as possible.

2. TSWD method

The results of the research project at Hieflau (Brückl et al., 2010) proved that TSWD can be implemented for the prediction of structures ahead of the TBM. Since 2011 it was applied at several different tunnel construction sites in Austria and is currently under operation in a 32 km long railway tunnel in the Koralm massive.

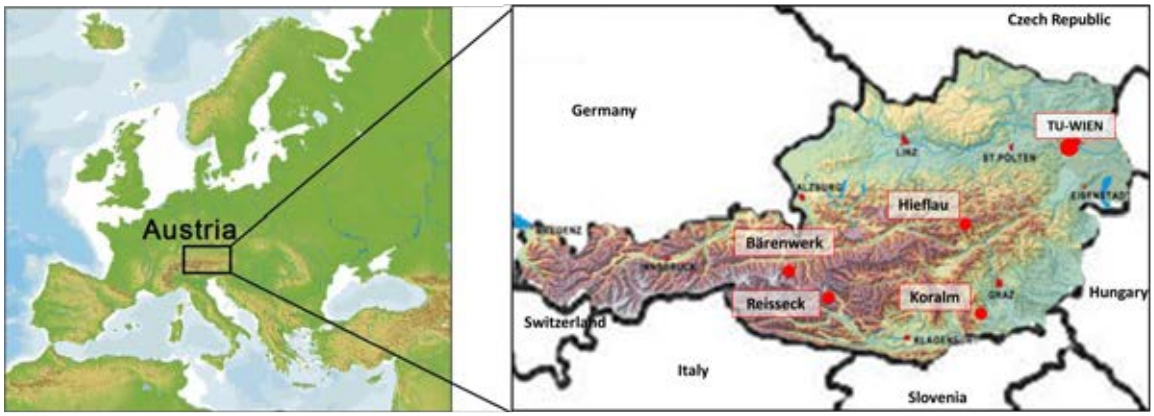

Figure 2.1.: Location of the tunnel construction sites, where TSWD was implemented in Austria.

The table 2.1 lists the main facts of each project. Several different types of TBM's were used as different geological conditions demanded open or shielded TBM's made by Wirth, Aker-Robbins, Robbins and Herrenknecht. The diameter of the tunnels varied from 4 to 10 m. At least 1000 m of tunneling were accompanied by TSWD over several months at each site. The highest advance rates were up to 37 m per day. As the railway tunnel project at Koralm has two tubes, two similar TBM's, named TBM-north and TBM-south, are working at the same time with varying distance to each other.

In the next chapters the geometrical layout, as well as the routine processing and results of TSWD are shown. Special focus is made on the registration of the pilot sensor. The registered wave field at the geophone receiver is described in detail and also different combination for the correlation of the pilot sensor data and receiver data. Finally the interpretation concept and some examples of the different tunnel projects are presented.

Table 2.1.: Main facts about the construction sites at Hieflau, Reisseck, Bärenwerk and Koralm, where TSWD was or still is implemented.

	Facts	**Hieflau**	**Reisseck**	**Bärenwerk**	**Koralm**
Project	Construction site	Hydropower plant	Hydropower plant	Hydropower plant	Railway tunnel
	Start End Duration	Jun.08 Sep.09 17 mo.	Nov.11 Mai.12 8 mo.	Apr.13 Mai.13 1.5 mo.	Feb.13 [Jun.2016] 26 mo. -
	Diameter of tunnel	6.2 m	6.2 m	3.8 m	9.9 m
	Geology	Limestone	Gneiss	Phyllite	Gneiss
	TBM type	Robbins DS Shielded	Wirth TB-703E Gripper	Herrenknecht Gripper	Aker-Robbins Shielded
TSWD	Measuring section	717 m	2523 m	1092 m	4147 m
	advance rate	-	13.5 m/d	25 m/d	15 m/d

2.1. Geometrical layout

The actual geometrical installation layout for the seismic instruments consists of a seismic monitoring registration unit with accelerometers at the head of the TBM and registration units with 3C-geophones behind the TBM (Figure 2.2). At least two accelerometers (parallel and radial to the tunnel axes) are mounted on the main bearing for recording the vibrations of the cutting head during drilling. The 3C-geophones are installed in deep boreholes (5 m) on the right and left tunnel-side walls at cross-sections, in order to get a good receiver signal. The boreholes for the receivers must be deep enough to ensure, that tube / Rayleigh waves traveling through the rock along the tunnel wall are not recorded. Furthermore, placing geophones in deeper boreholes will improve the signal to noise ratio. The deployment of receivers rather distant from the cutting head should allow recording without logistic problems, such as cable run, since the receivers stay at one cross-section up to several weeks.

The measurement cross-sections advance with the TBM and are rebuilt at a spacing of 100 to 200 m, normally in the maintenance shift. The distances are chosen depending on the advance-rate and the expected geological structures. No further construction work is necessary apart from drilling the holes for the measurement cross-sections.

The central position is the electrical control cabinet, mounted somewhere on the TBM with the data recorders (Reftek 130). They collect the signals from the accelerometers at the TBM head and those from the 3C geophones, sampled with at least 1000 Hz. At this place a server can be installed, which stores the data and trans-

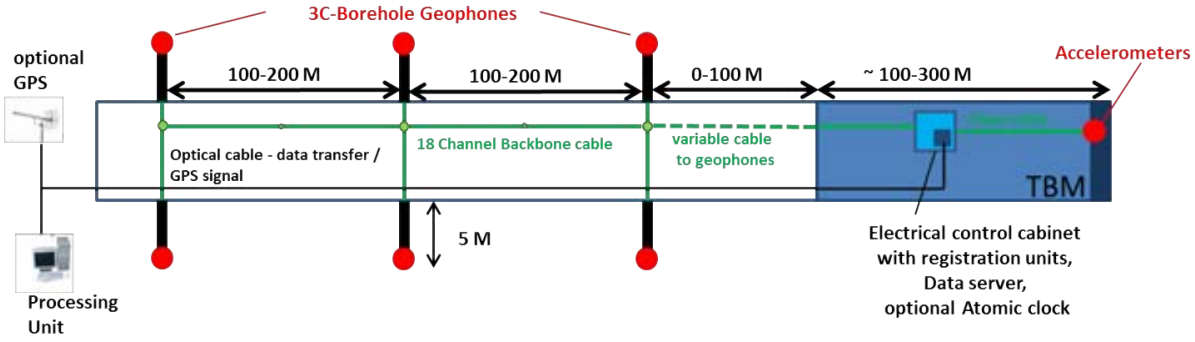

Figure 2.2.: General geometrical layout of a TSWD registration system

fers them in real time via a connection to the processing unit outside of the tunnel.

The equipment has to be very robust since environmental conditions in tunnel construction sites, caused by mud, water, dust, vibrations and EMC-safety precautions are critical. According to the site situation and the particular TBM type it is necessary to adapt the TSWD layout. The general layout of TSWD was adapted and improved during the different projects.

2.2. Pilot Signal

The cutting process described in chapter 5 is regarded as the source for the radiated seismic waves, and also induces vibrations of the machine. Until now these vibrations have not been recorded next to the cutters or on the rotating cutter head due to technical reasons. Therefore the position of the pilot sensors were always on the non-rotating part, the main bearing. The induced vibrations are transfered over the cutter head and bearing to the sensor location.

This chapter describes the recorded pilot signal at different TBM's.

Figure 2.3 shows the position of the pilot sensor of the TBM at Koralm. The cubes are welded on the non-rotating part (main bearing) of the TBM head approx. 3 m behind the tunnel face, but avoiding close proximity of background noise generating equipment such as transformers, electrical motors and / or band-conveyors for example. In order to prevent high amplitudes as a result of the metal – metal contact, a damping material was placed underneath the cubes. For redundancy purposes, two cubes are mounted on the left and right sides, which are individually connected to the recorders with fastened cables.

Two to three accelerometers in orthogonal directions are installed in a metal cube

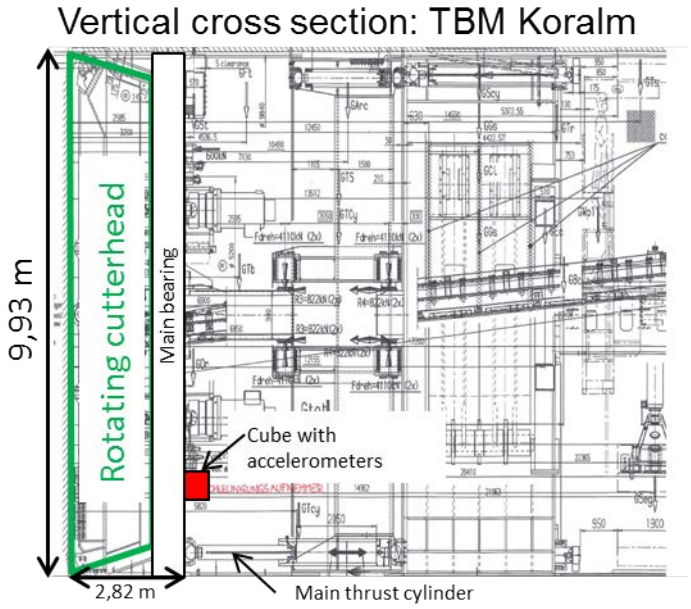

Figure 2.3.: Cross view of TBM head at Koralm with the position of the metal cube with accelerometers fixed on the main bearing 2.82 m behind the tunnel face.

(Figure 2.4). At least one sensor is aligned parallel to the tunnel axis. To avoid overloaded signals or too little amplitudes different sensitivities (+/- 5g and +/- 50g) are used to guarantee a good pilot signal, independent of the TBM type and geological condition. Tests where the pilot signal was sampled with higher frequencies (up to 32.000 Hz) proved that no significant frequencies higher than 500 Hz arrive at the pilot sensors.

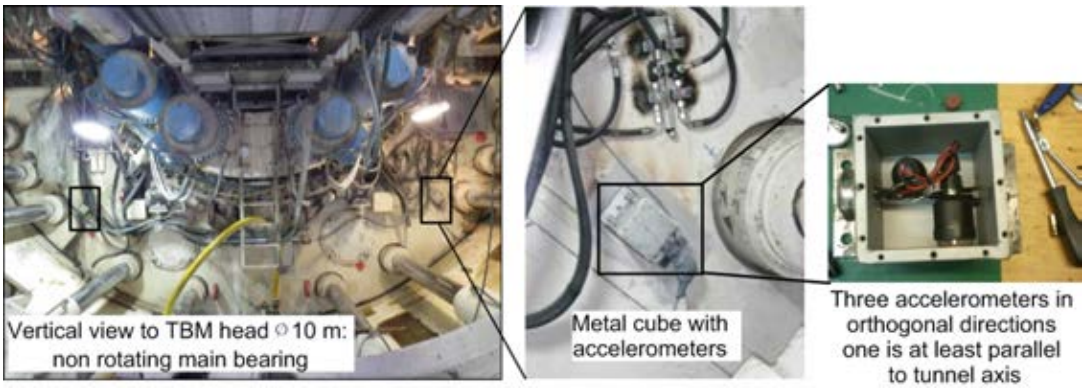

Figure 2.4.: Metal cube with accelerometers fixed on the non rotating part of the TBM head (main bearing) approx. 3 m behind the tunnel face at Koralm.

At the TBM at Reisseck only axial pilot sensors were installed, whereas at Bärenwerk and Koralm also radial directed sensors exists. The amplitudes of the axial components

are always larger than the radial components with a maximum factor of 1.3. The highest frequencies for all pilot sensors are up to 300 Hz. The maximum values differ for each TBM, but are between 70 Hz at Reisseck, 40 Hz at Bärenwerk, 170 Hz at Koralm-south, and 150 Hz at Koralm-north. Three to four local maxima are visible. The radial components have lower frequencies and show only two to three local maximums. Main radial frequencies are at Bärenwerk 40-70 Hz, 100 Hz at Koralm-south and 70 Hz at Koralm-north. The frequency spectra are shown in Figure 2.6. Although the TBM's at Koralm-south and north are similar, the difference in the frequency spectrum can be related to different locations on the TBM main bearing. In the autocorrelation of the components (Figure 2.5) the lower frequencies of the radial components are also clearly shown.

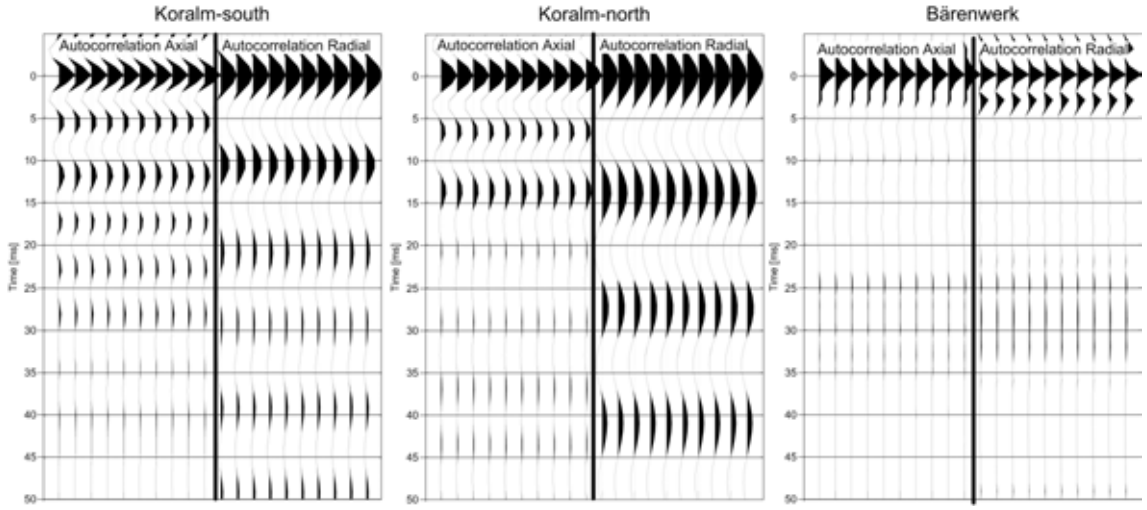

Figure 2.5.: Autocorrelation of axial and radial piltot sensors at the main bearing; Koralm south, Koralm-north and Bärenwerk: the radial components have lower frequencies, at Bärenwerk the difference is smaller.

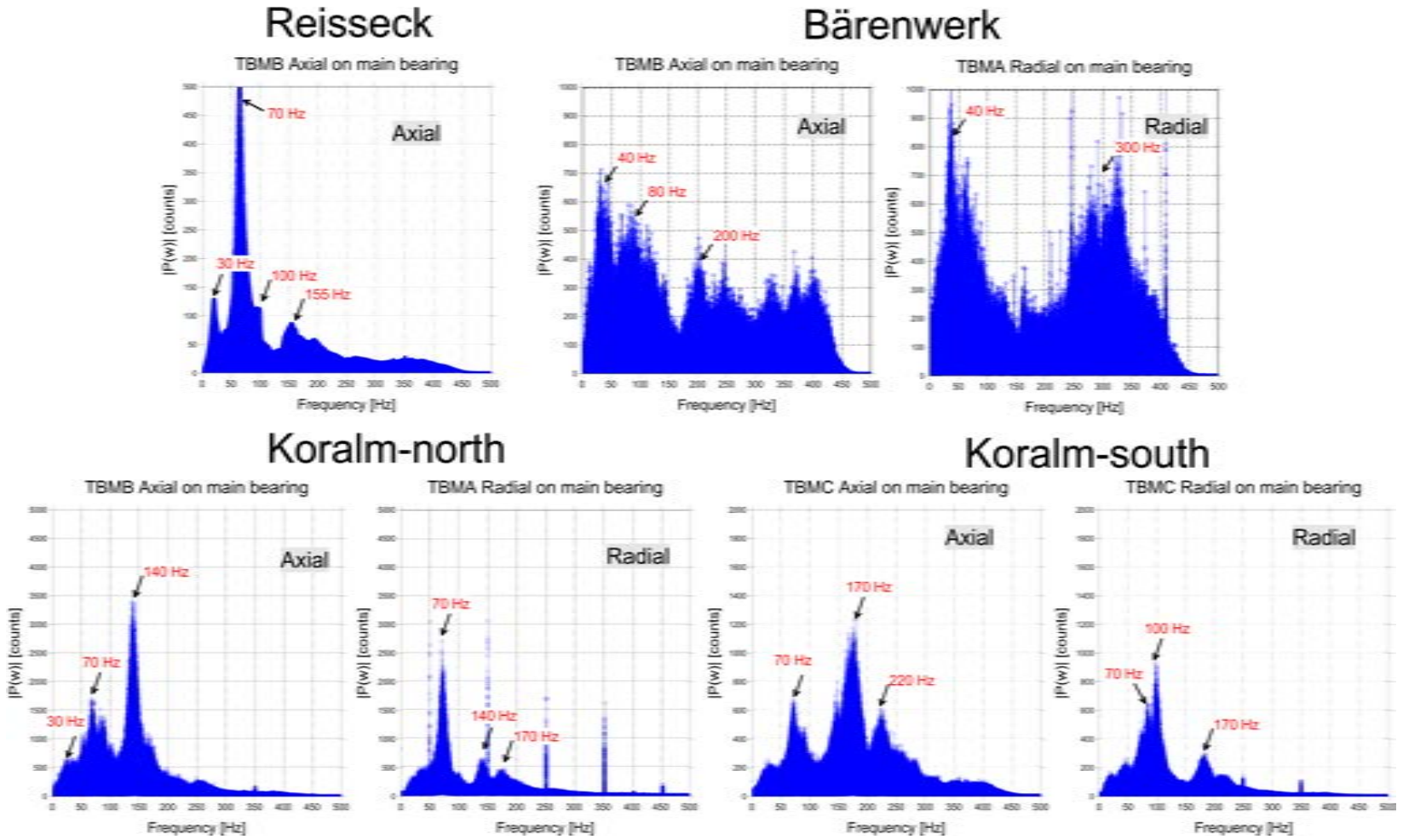

Figure 2.6.: Frequency spectra of the axial and radial pilot sensors at the main bearing of Reisseck, Bärenwerk and the two TBM's at Koralm. The black arrows and red numbers indicate maximums.

2.3. Receiver signal and comparison with the pilot signal

A so called measurement cross-section consists of two re-usable exactly aligned 3-component geophones with a natural frequency of 15 Hz. Around the 3-4 o' clock and 8-9 o' clock position at the sidewalls they are put into boreholes, at least 6 m deep and 2 inch wide, every 100 to 200 m. Both, right and left borehole geophone, data streams are truncated electrically into one cable, routing those streams to their recording devices in the electrical cabinet on the TBM. At least two cross-sections should be active to guarantee sufficient data for the prediction. The orientation of the geophone components are:

- Axial - A: parallel to tunnel axis in advance direction
- Radial - R: horizontal to the right (in regard to the advance direction)
- Tangential - T: vertical down

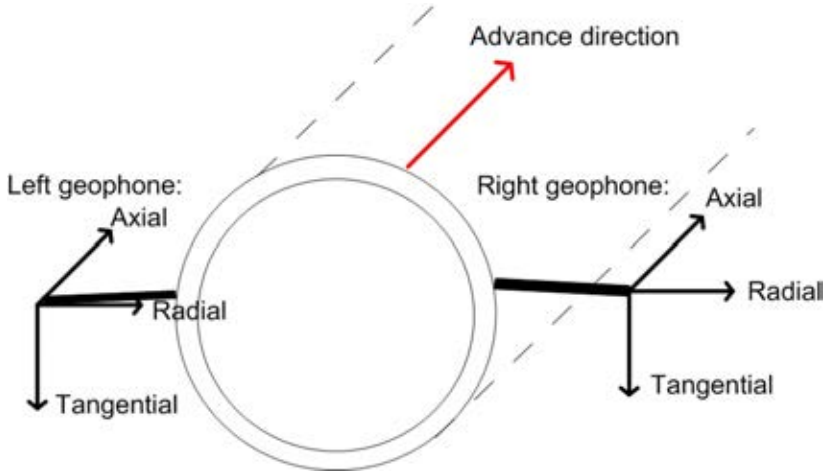

Figure 2.7.: Directions of the receiver geophone components Axial, Radial and Tangential in regard to the tunnel axis and advance direction

As representative examples the frequency spectra of some geophones at different cross-sections and tunnel projects are analyzed and compared to each other.

All receiver data contain frequencies only up to 200 Hz. Only if the TBM is very near (<100 m) frequencies up to 250 Hz occur. In general the nearer the TBM is to the geophones, the higher the frequencies are. The axial component has the widest frequency range before the radial and tangential components. The following example

at Reisseck shows that a maximum frequency at every receiver component is around 60-70 Hz. Higher frequencies are only present in the axial components despite the surface station HOTE, where the TBM was just 70 m below the geophones. The frequency spectrum of the components are presented in Appendix A. Table 2.2 shows frequency peaks and range of pilot sensors and geophones at several cross sections (MQ9-11) and the surface station HOTE at Reisseck for a certain position of the TBM. The offset ranges from 70 - 700 m. The maximum peaks are marked with thick letters.

Table 2.2.: Frequency peaks of cross-sections MQ09-11 and the surface station HOTE at Reisseck

Component	Frequency	Range
	Pilot sensor	
Axial	30 Hz, **70 Hz**, 100 Hz, 155 Hz	250 Hz
	MQ11 - 300 m behind	
Axial	**40 Hz - 70 Hz**, 120 Hz	170 Hz
Radial	30 Hz, **60 Hz**	120 Hz
Tangential	**30 Hz**	110 Hz
	MQ10 - 500 m behind	
Axial	30 Hz, **70 Hz**, 140 Hz	160 Hz
Radial	**30 Hz-70 Hz**	100 Hz
Tangential		no data
	MQ09 - 700 m behind	
Axial	30 Hz, **70 Hz**	120 Hz
Radial	**30 Hz**	100 Hz
Tangential	**30 Hz**	80 Hz
	HOTE - 70 m above	
Axial	30 Hz, **60 Hz**, 120 Hz	150 Hz
Radial	45 Hz, **70 Hz**	110 Hz
Tangential	45 Hz, **70 Hz**, 120 Hz	120 Hz
	HOTE - 550 m behind	
Axial	30 Hz, **60 Hz**, 120	125 Hz
Radial	**50 Hz**, 70 Hz, 100 Hz	110 Hz
Tangential	30 Hz, **70 Hz**	110 Hz

Table 2.3 lists the frequency peaks and range of pilot sensors in axial and radial direction and geophones at several cross sections (MQ39, MQ40 and MQ41) at the Koralm tunnel, where the TBM was just next to MQ40 and the other cross sections 200 m away. As the data contain a lot of electrical noise from the power supply, a predictive deconvolution filtering was applied to remove 50 Hz.

Table 2.3.: Frequency peaks of cross-sections MQ39 - 41 at Koralm

Component	Frequency	Range
	Pilot Seonsor	
Axial	30 Hz, 70 Hz, **140 Hz**	250 Hz
Radial	**70 Hz**, 140 Hz, 170 Hz	250 Hz
	MQ39 - 200 m behind the TBM	
Axial	**55 Hz**	100 Hz
Radial	**55 Hz**	100 Hz
Tangential	**40 Hz**	80 Hz
	MQ40 - 30 m to the TBM	
Axial	40 Hz, 120 Hz, **170 Hz**	220 Hz
Radial	**40 Hz**	150 Hz
Tangential	**40 Hz**, 120 Hz	150 Hz
	MQ41 - 200 m in front of the TBM	
Axial	**40 Hz**, 120 Hz	130 Hz
Radial	**40 Hz**, 150 Hz	180 Hz
Tangential	**40 Hz**, 120 Hz	130 Hz

The frequency content of the pilot sensor and the geophone sensors are in the same range. The maximum values are below 250 Hz. The axial components and sensors show higher frequencies than the other directions. The high frequencies arenormally related to the p-waves, and the lower ones to the s-waves. This can be seen in the data set. If the TBM is very near, the frequencies are higher at all components. A separation of the p-wave and s-wave is more difficult there.

2.4. Timing and positioning

The timing and synchronization of the registration units is an essential part of the method. During the last two four years different techniques were used. Standard practice is to transmit the GPS signal from an antenna outside through an optical fiber cable to the recorders, which can be impractical in long tunnels. Therefore, a version with an atomic clock was developed, which is directly connected to the recorders. It simulates the GPS signal and guarantees also the synchronization in absolute time. The accuracy of the atomic clock is also sufficient for long operational periods of 3-5 months without permanent synchronization with the GPS. In case of surface measurements with GPS timing, the synchronization is assured. Timing with atomic clocks is also very useful in case two TBM's are in operation (e.g. at the Koralm

tunnels) and have to be synchronized. The TSWD data in time is then positioned at the correct tunnel chainage from the available TBM machine datasets provided by the TBM contractor.

2.5. Routine processing

In the following chapter the main steps are described from the raw data to the final results. The raw data of every recording unit (Reftek 130) can either be stored on compact disc and then transmitted to the processing unit, or is directly transfered to a server, which is connected to a local network. To realize a near real time prediction, the processing is partly automated.

2.5.1. Detection of times with active TBM

As the recording data register continuously 24 hours per day, the processed data is minimized to times, when the TBM was active. A code has been written, which detects these time sections (called events) on a pilot sensor data with a simple short-time average to long-time average ratio (sta/lta). Figure 2.8 shows an example over one hour with three detected events. When this ratio is bigger than a certain threshold value (green line in figure 2.8), an event is marked until the value is smaller than the thresh off value (red line in figure 2.8). This reduces traces, which contain only noise.

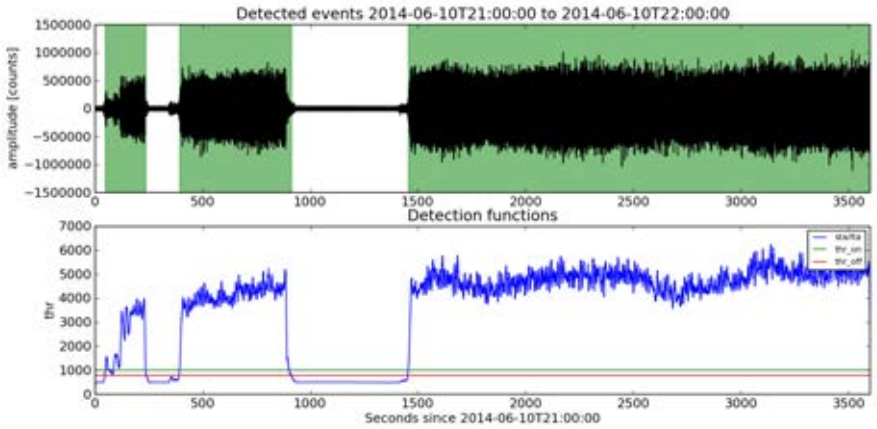

Figure 2.8.: Signal of a axial pilot sensor within one hour; Time sections, when the TBM is active, are detected with the help of an sta/lta-ratio.

2.5.2. Minimum delay transformation

The main steps of further processing are described in Brückl et al. (2010). First an automatic process cuts out time windows of 32 sec to 1 min of the pilot and receiver data at the same absolute time. Second, it calculates the minimum delay filter and finally it applies this filter to the receiver signal (see chapter 1.3). The actual tunnel chainage is added automatically for each trace. The results of this procedure are seismic traces with a nominal shot distance in the range of millimeters and centimeters.

The data is afterwards imported to the software PROMAX, which is used to perform further processing steps. After the elimination of traces with low signal-to-noise-ratio, the traces are stacked to 1m bin size (Figure 2.10).

In this section, results are presented after the minimum delay transformation with different axial and radial pilot sensor data at the main bearing. Differences and similarities are shown and discussed.

The axial section contains most of the p-wave after the minimum delay transformation with the axial pilot sensor. Figure 2.10 shows the traces and their frequency content of a right geophone at MQ11 over an offset of 255 until 300 m. The radial and tangential sections contain most of the s-wave. The p-wave is slightly visible on the radial component. As the axial components show the higher frequencies than the radial and tangential components, the p-wave can be related to the higher maximum peaks at 70 and 120 Hz, whereas the lower ones are related to the s-wave ($<$ 50-70 Hz).

Another example of the minimum delay transformation with an axial pilot signal at Koralm is shown in Figure 2.11. The seismic section of the axial components have peaks at, 30-70 Hz, 120 Hz and 160-170 Hz in front of the TBM and 30-70Hz, 80Hz behind the TBM. When the TBM is just next to the geophone, the higher frequencies at 170 Hz are more pronounced. They can be related to the signals with 100 m offset to MQ40. The radial and tangential component at MQ39 have a lower frequency range of 30-80 Hz. The axial components contain more s-wave, which has not been observed in the other tunnels. However, the TBM used here is a double-shield TBM with continuous lining. Thus, it is assumed that the observed 's-wave' is in reality the tube wave along the tunnel lining, which reaches deeper than 4 m.

The use of the radial pilot sensor improves the s-wave in the radial and tangential components, but the axial component has nearly no p-wave (Figure 2.12). Therefore, the radial sensor is not used for the TSWD processing. Possibly it can improve the s-wave processing, which has not be done until now.

It was mentioned in the limitations of the TSWD method (see Introduction) that

the resolution of the beginning of structures in front of the TBM is limited to approx. 10 m. It depends on the frequency content of the registered signals at the geophone cross-sections. The highest frequency range off an axial geophone component at a cross section is 200 Hz (see Chapter 2.3 - Receiver signal) and the maximum is always are under 100 Hz. It has to be mentioned that the geophones records also surrounding noise in the tunnel, which is probable high frequent and lies within the analyzed signal.

There the range for the axial receiver at MQ11 (Reisseck), with a distance of about 300 m to the source, is about 170 Hz . After the minimum delay transformation the frequency range of the axial component is approx. 120 Hz (Figure 2.9). The frequency range is here reduced by 30% of the original spectrum.

The original frequency range is 100 Hz for the axial component of MQ39 with a distance of 200 m to the TBM. After the minimum delay transformation it is around 90 Hz. Here the reduction is only 10% of the original spectrum.

Therefore a maximum increase of the actual resolution is probable limited to 30% . In numbers, the maximum resolution would be approx. 7-8 m.

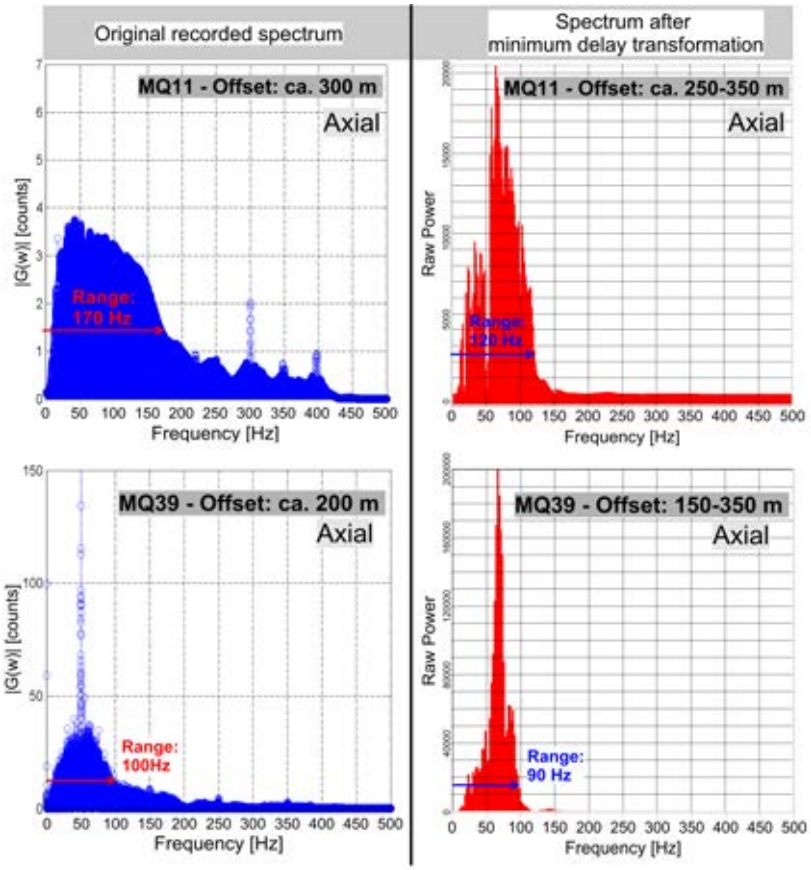

Figure 2.9.: Comparison of the rang of frequency spectra at the axial geophone MQ11 (Reisseck) and MQ39 (Koralm) before and after the minimum delay transformation.

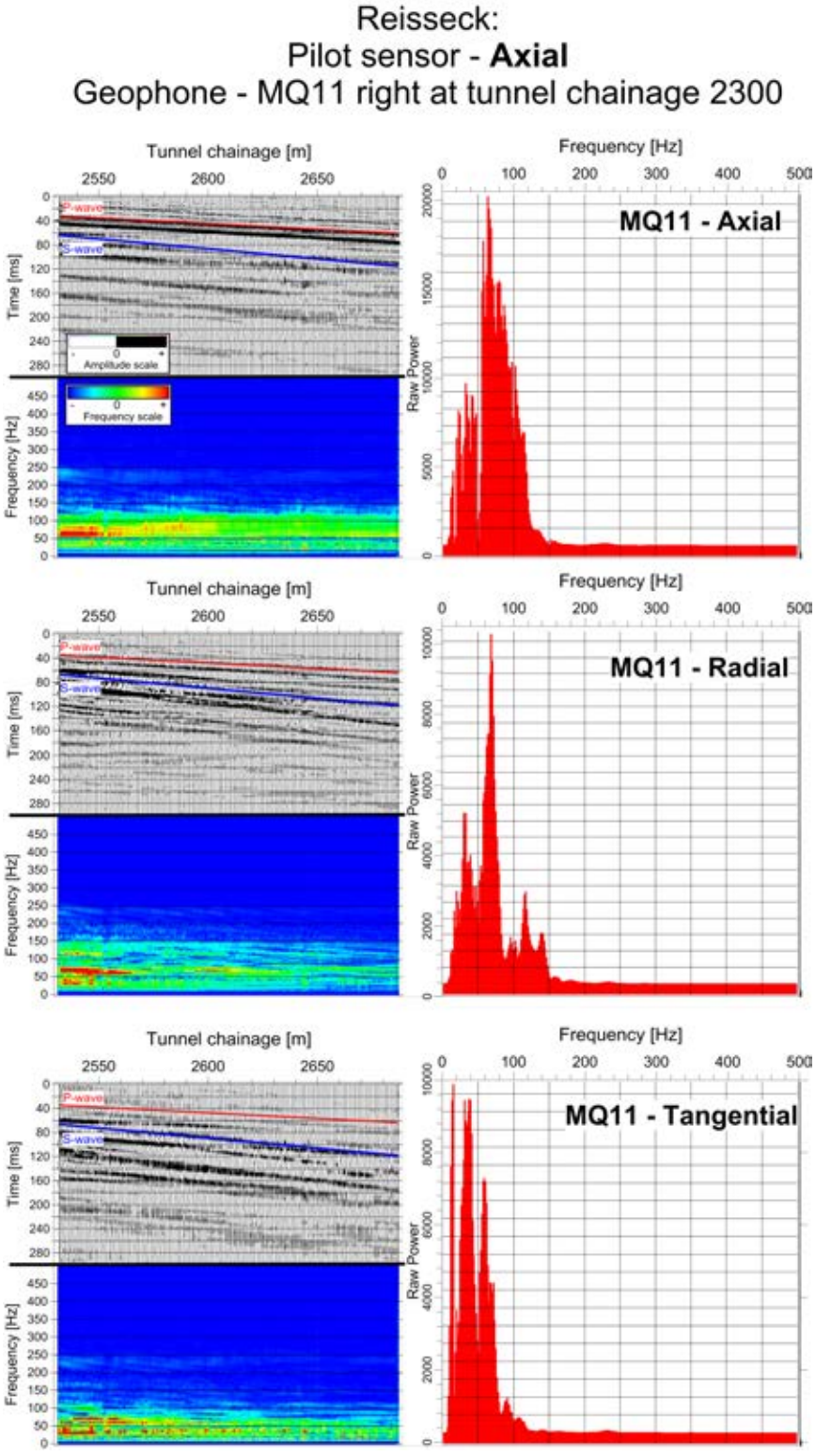

Figure 2.10.: Processed traces and their frequency content (offset: 255 - 400 m) of the right geophone components of MQ11 at Reisseck. The red and blue lines in the seismic section show the first break of the p- and s-wave. The axial component with a dominant p-wave has frequencies up to 120 Hz, the radial component with more s-wave than p-wave has its frequency maximum at 70 Hz. The lowest frequencies are in the tangential component, where only s-wave is visible.

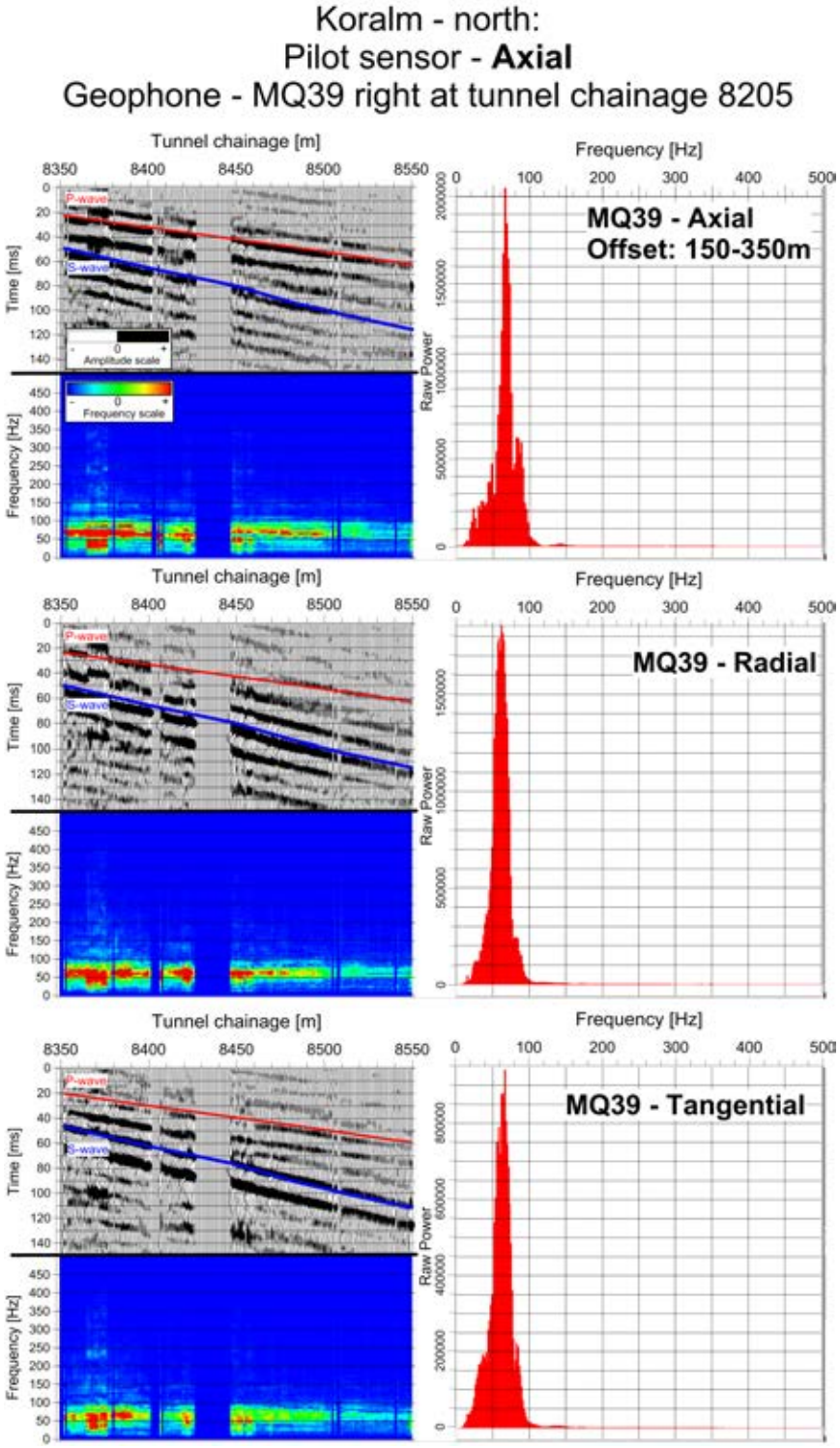

Figure 2.11.: Processed traces and their frequency content (offset: 150 - 350 m) of the right geophone components of MQ39 at Koralm. The red and blue lines in the seismic section show the first break of the p- and s-wave. The axial component with a dominant p-wave has frequencies up to 100 Hz, the radial component with only s-wave has its frequency maximum at 70 Hz. The lowest frequencies are in the tangential component, with dominating s-wave and a very small p-wave.

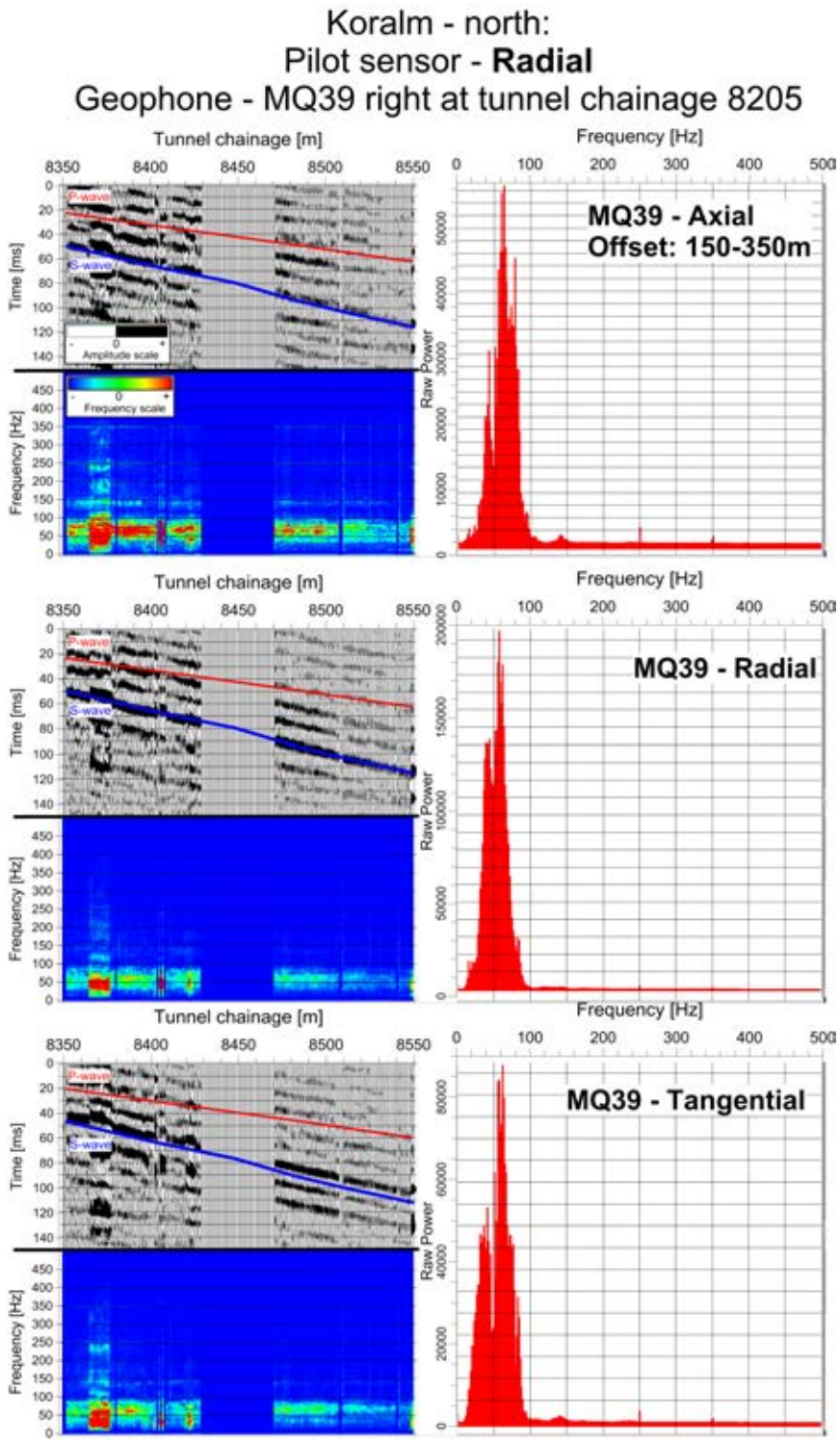

Figure 2.12.: Processed traces and their frequency content of the right geophone components of MQ39 at Koralm. The red and blue lines in the seismic section show the first break of the p- and s-wave. The axial component has nearly no p-wave amplitudes, whereas the s-wave on the radial and tangential components are very strong.

2.5.3. Determination of wave velocities

The direct arrivals of the p-wave and the s-wave are manually picked. Thereby the picks are set at the beginning of the p-wavelet and s-wavelet, as a consequence of the minimum delay assumption. Afterwards the amplitudes are normalized. As the signals are synchronized in time, a determination of the p-wave velocity and the s-wave velocity of the already drilled section can be done. These velocities are shown in the final result for documentation and comparison with the encountered geology (Figure 2.19).

2.5.4. Removal of direct wave field

Subsequently, the first breaks are aligned horizontally and then removed by subtraction of the mean, or with f-k filtering. Thus, the resulting seismograms contain only the reflections from structures ahead of the tunnel face (Figure 2.13 down).

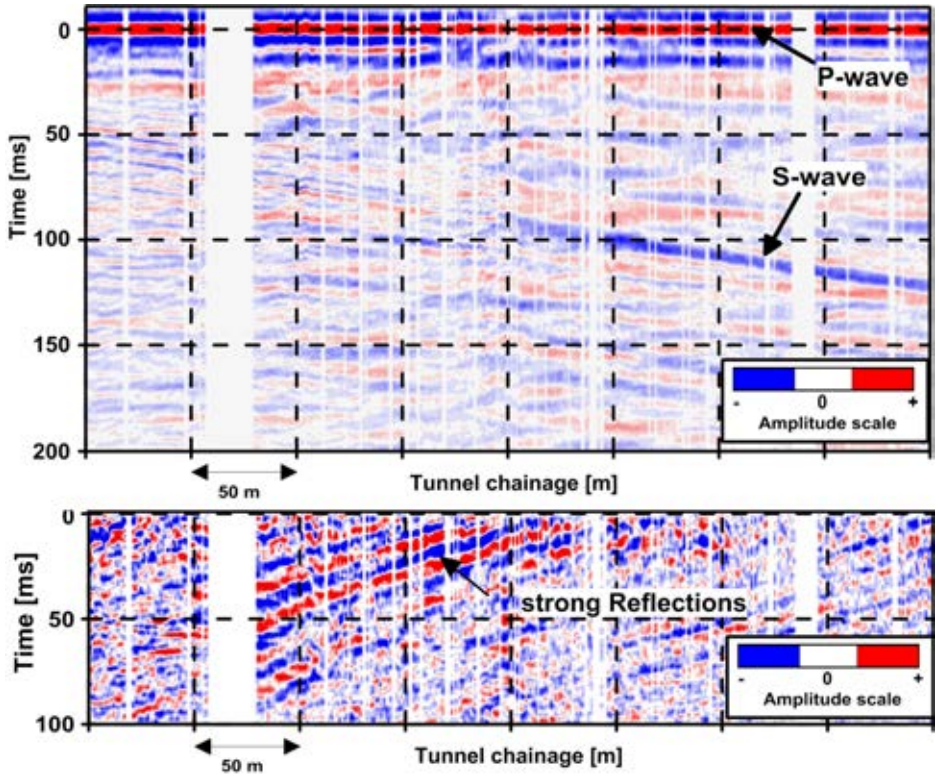

Figure 2.13.: top: seismic traces recovered by application of minimum delay filter for the axial component, aligned to the first P-wave arrival with a source interval of 1m; p- and s-wave arrivals are marked by arrows; down: reflecting wave field for the same receiver and component after removal of first arrivals of p- and s-wave (Brückl et al., 2010).

2.6. Interpretation

The results can be better explained to technicians and geologists and also compared with other prognoses, if the arrivals of the reflected wave field are rotated by using a seismic velocity. The p-wave velocity (v_p) of the last 100-200 m is used, since the main information is gained from the p-wave reflection. During the ongoing processing, it is necessary to adapt this velocity to the changing rock material. Therefore, a reflection is not displayed after 30 ms, but rather in a prediction distance of 60 m (with v_p = 4000 m/s) to the current TBM position, where prediction distance = time * $\frac{v_p}{2}$ (Chwatal et al., 2011). A possible discontinuity perpendicular to the tunnel axis, for instance, can be seen as a vertical reflection line (Figure 2.14). This image changes if the discontinuity is inclined to the tunnel axis, which is related to the apparent velocities. The exact declination and inclination of faults can principally be calculated with an additional 3-component processing.

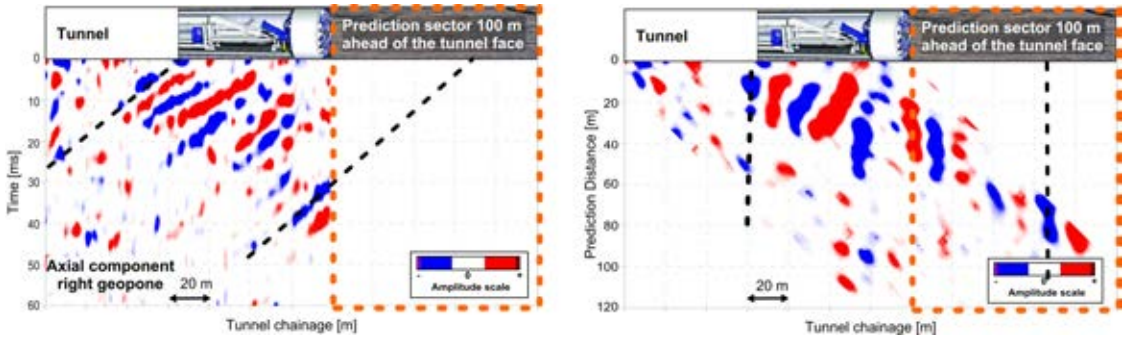

Figure 2.14.: By using a seismic velocity the reflections are rotated according to prediction distance = time * $\frac{v_p}{2}$. A orthogonal discontinuity is then mapped as a vertical line. left: mapping based on time domain; right: mapping based on prediction distance.

2.6.1. Prediction and classification

The results (sections) from the individual cross-section (separated into left- and right-hand geophones or sides) are displayed on a plan view of the tunnel. The axial components are often preferred for the assessment since these deliver the most reliable results for steeply dipping fault zones. To assess the intersection of the reflection with the tunnel axis is an essential part of the prediction for determination of the distance between the fault zone and the current tunnel face.

The sections image seismic reflections with various amplitudes, which give the information of the velocity and density contrasts ahead of the tunnel face. If these amplitudes are very low, the rock is homogeneous and no fault zones or changing rock

conditions are expected. Reflections with higher amplitudes indicates fault zones, a change in lithology and rock conditions, in which the tunnel is drilled. The intersection of fault zone with the tunnel axis is identified with the beginning of the reflected wavelet.

The prediction has to be evaluated and classified for the tunnel construction. The constructors are just interested in possible dangerous zones for the machine in order to be prepared while tunneling. Therefore, a classification of the reflections is done via a traffic light system (green- yellow- red), which is based on the actual geological situation. This needs to be discussed and interpreted in detail with the geologists on site. In a case of the yellow classification, it is proposed to make additional drillings before the TBM is reaching this zone. This improves 1) the prediction and 2) the resolution of the structures/faults ahead.

TSWD results in a geophysical forecast window of 100 - 150 m ahead of the current tunnel face. As the data is continuously processed, the results can be updated regularly. For large tunnel sites this must be done daily (Figure 2.15). Reflections indicating structures can, therefore, be followed and predicted until they cross the tunnel axis. A change in direction and consequently location of these structures along the axis can be determined.

The classification scheme of the project in Reisseck is shown in the Table 2.4. The corresponding geological interpretation was made in close cooperation with the geologists on site. The yellow zones correlated with changes in the seismic velocity and showed a close relation to the faults and fault zones. The TSWD at the Koralm tunnel site was continuously correlated with the drilling during the first 5 km. The evaluation of this section showed that the seismic systems can predict all important and relevant faults and structures. As a consequence they reduced the number of drilling up to 33%. The expensive and time consuming drilling is now only made when the seismic predicts yellow zones (Radinger et al., 2014). The prediction is an ongoing process. The knowledge and experience of geophysicists and geologists helps to improve the results during tunneling. An actual comparison with the encountered geology, discussion of earlier structures, and evaluation of the proper processing steps are essential for a successful prediction.

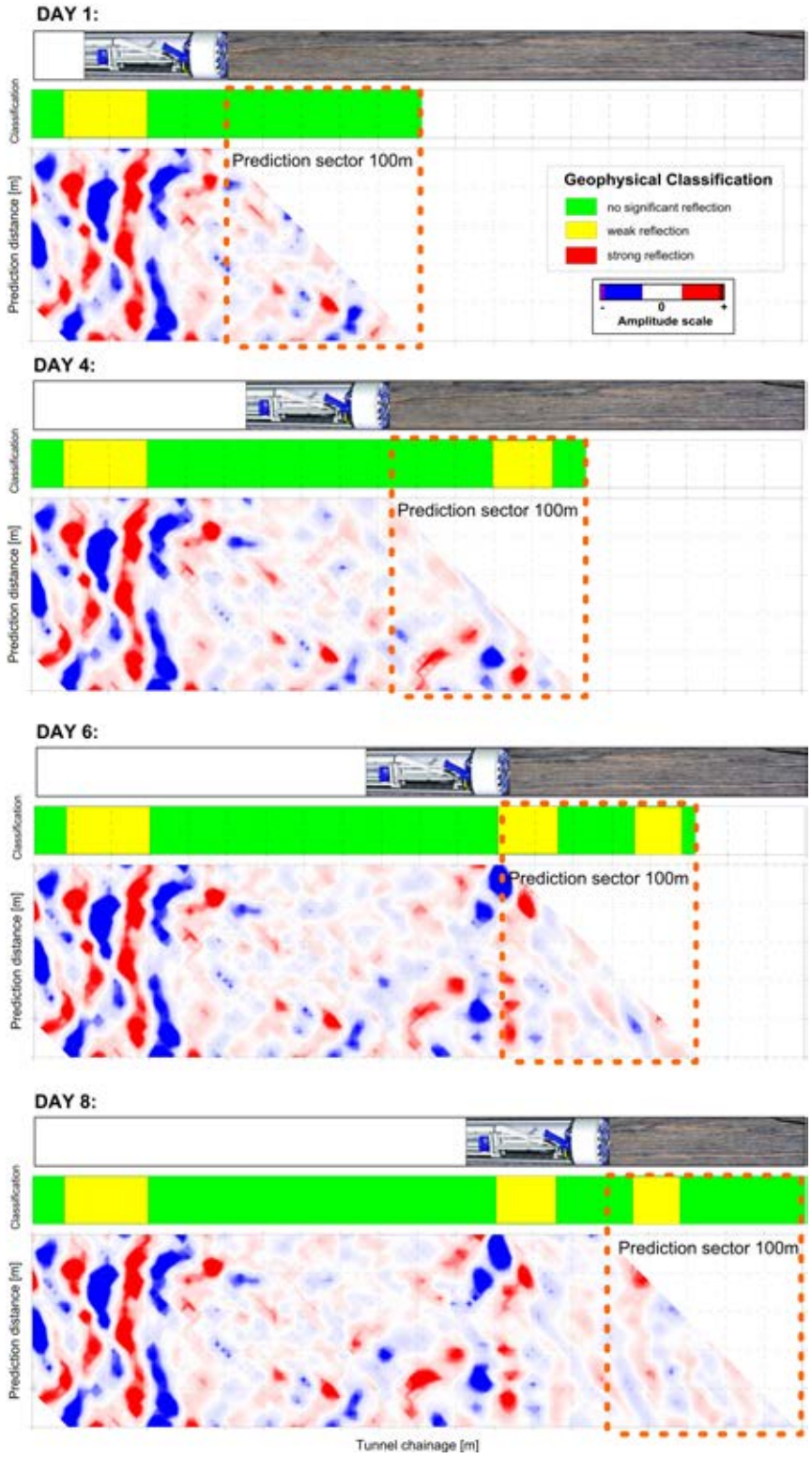

Figure 2.15.: Through a daily update of the results reflections can be followed and predicted correctly until they cross the tunnel axis.

Table 2.4.: Classification of TSWD prognoses like a traffic system with green, yellow and red zones

TSWD prognosis	**geophysical Classification**	**Geological Description**
green zone	no significant reflection	little disjointed and/or lightly weathered rock
yellow Zone	weak reflection	moderate fractioning and/or open joints and/or weathered rock
red Zone	strong reflection	Fault zone with loose material and/or strong jointed rock and/or strong weathered rock

2.6.2. Examples

The TSWD results have always been compared with the encountered geology. Not only changes in the rock quality and faults were determined, also slight changes in lithology were detected. There is a good resolution of fault zones wider than 10 m. Minor faults can be also detected, although the location accuracy is limited to 10 m.

For the daily result it is also helpful to stack the amplitudes along the vertical axes (prediction distance) resulting in the so-called seismic tunnel tape (Figure 2.16). It highlights the sections with high amplitudes, especially the nearly vertical inclination of reflections/structures to the tunnel axes. This also supports the classification.

Figure 2.19 shows the reflection image of a fault zone compared to the geology and seismic velocities that were obtained afterwards. This fault zone (dashed lines) is characterized by high amplitudes. Also, the increase in the seismic velocities and the geology confirm the prediction.

The next example (Figure 2.17) shows a 60 m long fault zone with several steep faults within a gneiss. The reflections could be clearly seen only within 50 m prediction distance.

The reflected wave field in Figure 2.18 corresponds to a 1 m wide fault and a lithology change. It was possible to see the beginning of this fault. However, since the resolution of the seismic data is about 10 m, it was not possible to determine the thickness.

TSWD is able to detect 80 % of the prominent and construction relevant faults or transition zones at the different tunnel sites (Kreutzer et al., 2012; Radinger et al., 2014). These authors state that by using a seismic system such as TSWD, the number and extent of the probe drillings needed can be optimized, which is favorable for overall construction progress. Limitations are already discussed in the introduction (Chapter

1.3). Structures, which dip very gently or strike at an acute angle to the tunnel axis, have been found to be unfavorable. The continuous incorporation and evaluation of all geological-geotechnical tunnel data naturally improves the knowledge and, thus, also the prediction certainty.

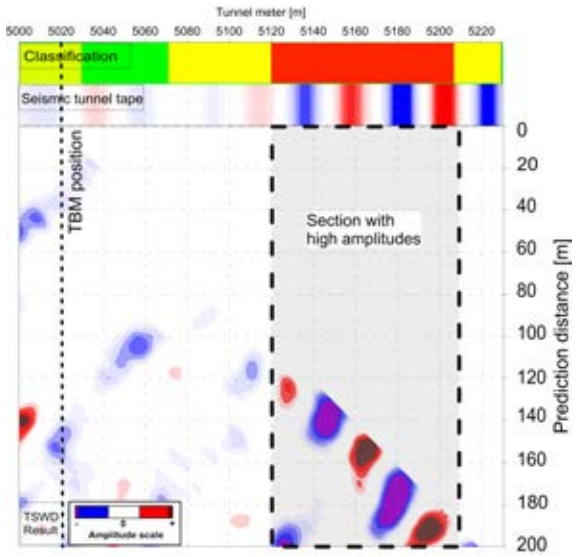

Figure 2.16.: The figure shows the reflecting wave field of the axial component with the corresponding seismic tunnel tape and the classification scheme at the Koralm site. High amplitudes indicate a fault zone. The prediction distance is shown up to 200 m.

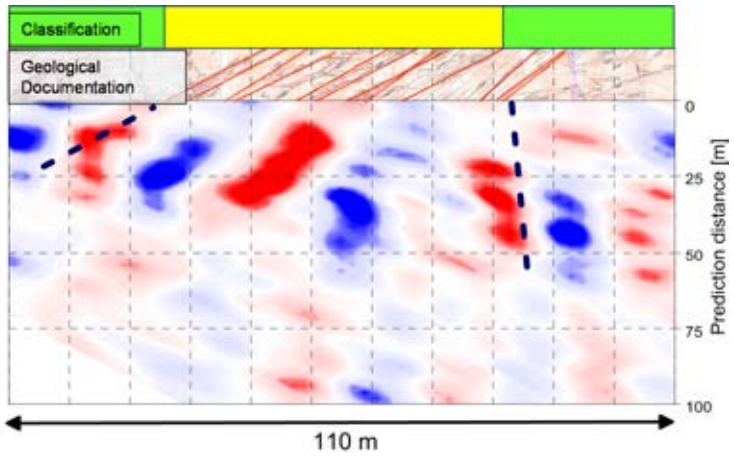

Figure 2.17.: Example result with classification at Reisseck; fault zone with 60 m, the dashed lines indicate the beginning and the end of the fault zone.

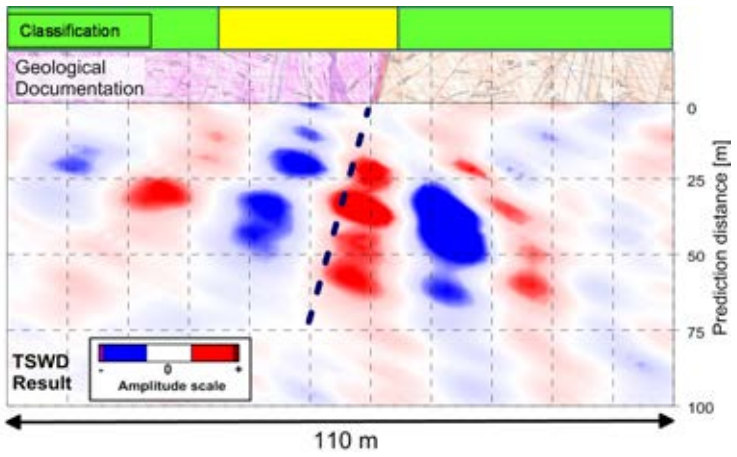

Figure 2.18.: Example result with classification of Reisseck; Lithology change and a 1 m wide fault

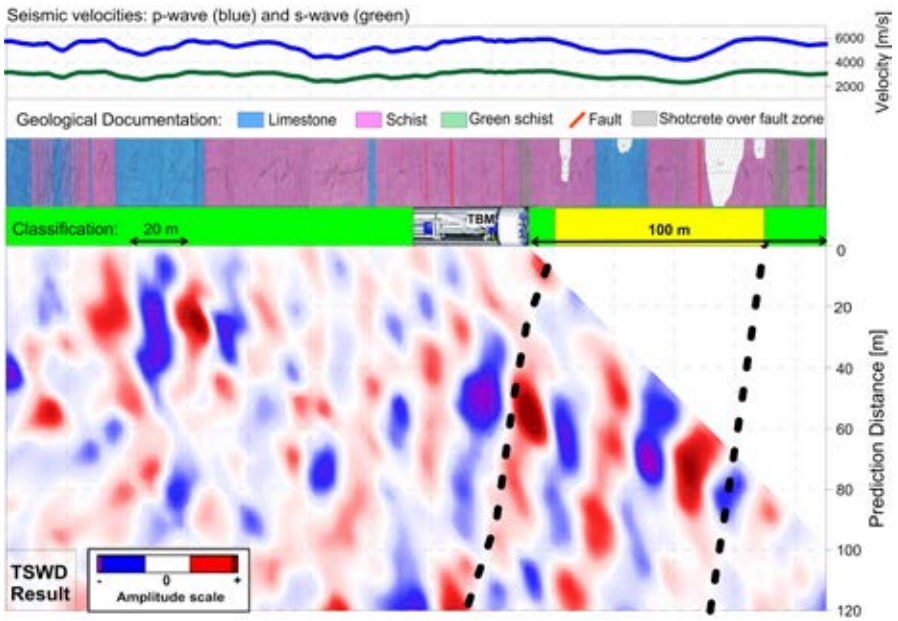

Figure 2.19.: Example Bärenwerk: reflection image of a 100 m wide zone with several faults, classification, encountered geology and seismic velocities of the p- and s-waves obtained after drilling; the reflections are presented with positive and negative amplitudes; dashed lines indicate a fault zone.

3. Closer inspection of the pilot sensor signal

The assumption, that the pilot sensor response (P) is a minimum delay wavelet (see Introduction), was not proved so far. However, it determines the first break picking on the begin of the wavelet and also the interpretation of the reflections. This chapter shows results of sledge tests on the cutterhead. By consideration of the minimum wavelet, criteria were found, which identify good positions for the registration on the main bearing. Considering that the origin of the vibrations are the cutters, there must be an influence of the TBM itself, which brings the signal to the registration unit. An attempt to determine a transfer function is also shown.

3.1. Criteria for the position of pilot sensors

It is not clear without any knowledge of the actual TBM machine and its interaction with the rock during the cutting process, which recording position of the pilot sensors is the best. Therefore a test was performed, which recorded the signals of several strokes next to cutters at different receiver positions at the TBM head (on cutterhead and main bearing). By generating signals with a hammer stroke next to the cutters, which are regarded as source point for the seismic waves, the recorded signal at the main bearing should correspond to these criteria:
- maximum energy is at the beginning (consequence of a minimum delay wavelet)
- short signal length (no long pulse oscillation)
- broad frequency spectrum.

This test was performed at the TBM at Bärenwerk and Koralm. Here the pilot sensors were already installed, as it was logistically not possible to make the testing before. So this test should also optimize the actual position of the pilot sensors (receiver point F). As space and measuring time was limited within the TBM head, the stroke points next to cutters and receiver points were also limited.

The figures 3.1 and 3.2 show the layout and results of the test at Bärenwerk. Signals from sledgehammer strokes adjacent to 11 disc cutters (red points in Figure 3.1) were collected with a sampling rate of 32 kHz at position A and simultaneously other parts of the main bearing. All together five positions are described (positions B-F: blue

points in Figure 3.1). The same accelerometers, which are used to record the pilot signal, were fixed with a magnet to the metal TBM body parallel to the tunnel axis (axial). The stroke positions were on the backside of the plate, where the cutters are mounted, as it was not allowed to go behind the cutterhead. Position B, C, D were near the tunnel wall on the rotating part of the cutter head, position E and F were on the main bearing.

Figure 3.2 shows the reflection strength and frequency spectrum of the recorded traces at position A-F and above the maximum amplitude values, the green boxes indicates the signal length. The signals were resampled with 1000 Hz, as the used sampling rate in the TSWD -method is limited to this value. By comparison the different receiver positions following statements are possible:
Position A: energy at at the beginning, short impulse length, broad frequency spectrum and highest amplitudes;
Position B: energy at the beginning but longer impulse length;
Position D: low energy all over the length of the signal, longest impulse length and a narrow frequency range;
Position D: energy at the beginning but longer impulse length and a narrow frequency spectrum;
Position E: energy at the beginning, short impulse length, frequency spectrum similar to A and highest amplitudes;
Position F: energy is at the beginning, the impulse length is short, broadest frequency spectrum although the position is farer away than at E.

Until now it is technically not feasible to install sensors on the rotating TBM head, such as positions A-D. The best position regarding the minimum phase shape and impulse length is position E. Similar results were obtained for the position F, but with a broader frequency spectrum.

This test was repeated at the TBM of Koralm-south. The next figures 3.3 and 3.4 show again the layout and results of the test, as described in the pictures before. The receivers were all situated on the main bearing - more or less at the same plane. The position F and G correspond to the actual pilot sensor position for the TSWD-method. A comparison with a receiver next to a cutter was not realized, as the recorded signals were over amplified. Regarding the criteria, the best positions are positions F, G and H with high amplitudes, short impulse lengths and a broad frequency spectrum. The worst position is the position E, here the energy is not at the beginning.

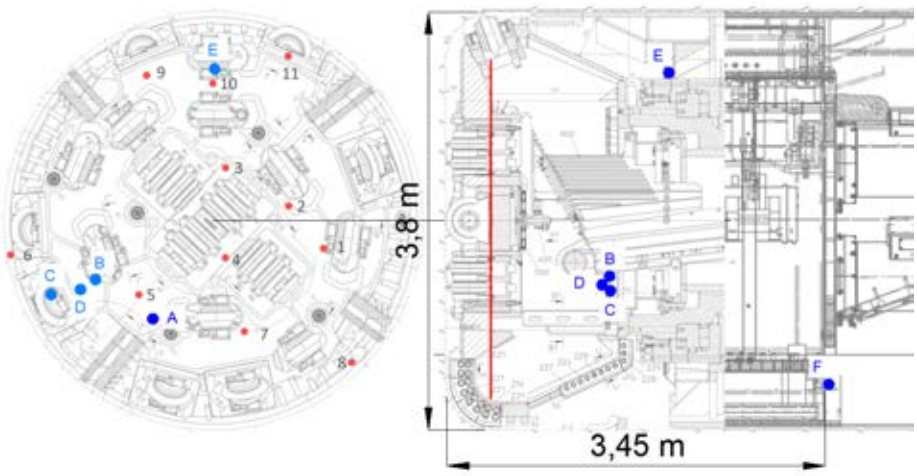

Figure 3.1.: Test layout at Bärenwerk; red points: stroke positions on cutter head, blue points: receiver positions along the TBM, the red line indicates the stroke plane on the cutter head; light blue points correspond to the receiver position in a front view.

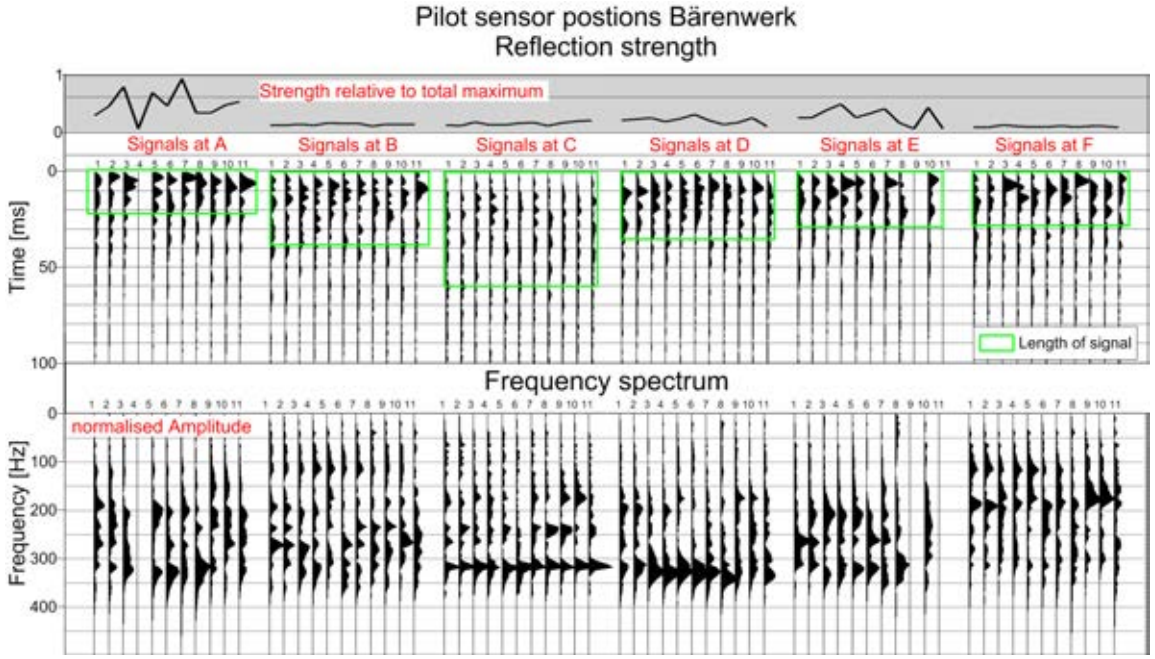

Figure 3.2.: Comparison of reflection strength and frequency spectrum of each stroke point at receiver positions A-F; green boxes indicates the signal length; TBM Bärenwerk

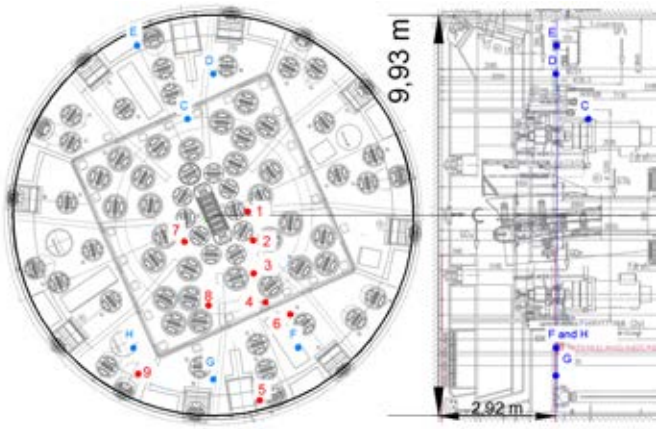

Figure 3.3.: Test layout at Koralm; red points: stroke positions on cutter head, blue points: receiver positions along the TBM; light blue points correspond to the receiver position in a front view.

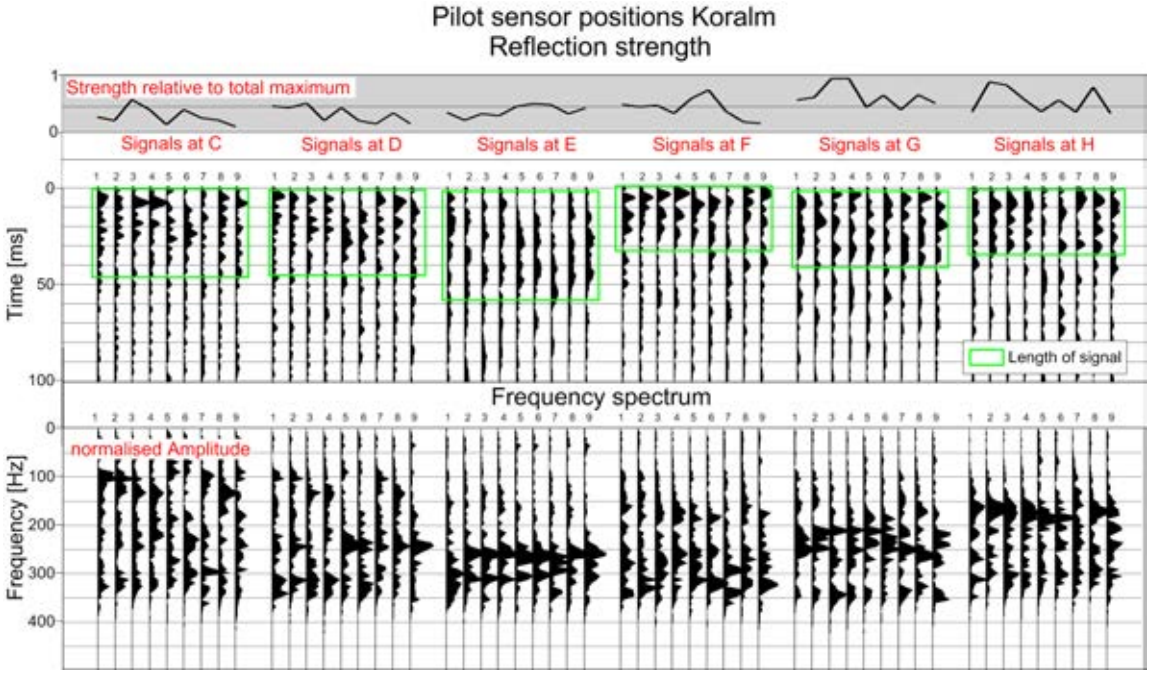

Figure 3.4.: Comparison of reflection strength and frequency spectrum of each stroke point at receiver positions C-H; green boxes indicates the signal length; TBM Koralm-south

3.2. Attempt to determine transfer function

Considering that the source points of vibrations are the cutters (here represented by the signals at position A) there must be an influence of the TBM itself bringing this signal to the registration unit which can be called a transfer function. An attempt to determine this transfer function was done with the data of the hit test at Bärenwerk for the position F (actual location of pilot sensor).

The transfer function (TF) between the position on the cutterhead A and the main bearing at F was estimated by dividing the Fast Fourier Transformed signal (FFT) of the position F with the FFT of the signal at the position A.

$$TF = \frac{FFT(F)}{FFT(A)} \tag{3.1}$$

During tunneling, the vibrations are generated simultaneously at each cutter positions and are registered at one point. Therefore, the eleven signals were summed up and the mean value was calculated for the positions A and F. To get the source signal on the cutter head, the pilot signal on the position F has to be multiplied with 1/TF in the frequency domain. This function is limited to frequencies lower than 30 Hz and larger than 350 Hz, as the signal strength of the position F is very low, therefore, only noise would be increased.

Figure 3.5 shows the mean frequency spectrum of position A and F and the function 1/TF.

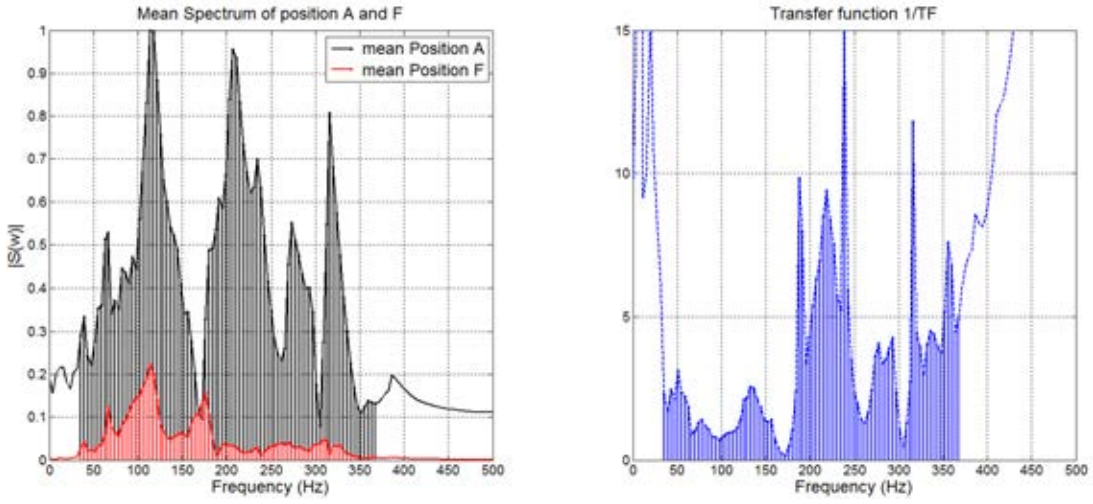

Figure 3.5.: Scaled mean frequency spectrum of the position A (black lines) on the cutter head and the position F (red lines) on the main bearing - left picture, the inverse transfer function in the right picture.

In our processing, the seismic trace T is generated according to Chapter 1.3 - TSWD

concepts and limitations - by filtering the receiver signal Sr with a compress filter (P/Sp), where P is the pilot sensor response to an individual event (P_{atA} at the position A) and Sp is the recorded pilot signal at the position F. The pilot sensor response is there now referred as (P_{atF}). Thus, the equations can be written as:

$$Sp = I \cdot P_{atF} \tag{3.2}$$

$$T = Sr \cdot \frac{P_{atA}}{I \cdot P_{atF}} \tag{3.3}$$

Assuming that the calculated transfer function TF of the stroke test is also valid for the recorded pilot sensor signal, we can rewrite the last equation to

$$T = Sr \cdot \frac{P_{atA} \cdot TF}{I \cdot P_{atF}} = Sr \cdot \frac{P_{atA}}{Sp} \cdot TF \tag{3.4}$$

The already processed data only has to be multiplied with the transfer function in the frequency domain. This should sharpen the signal, as the wavelengths are shorter and the frequencies increased. This should be also valid for the reflected wave field. Nevertheless, after applying the transfer function to the data, none of these objectives were detected in the processed data.

This implies that the determined transfer function by this sledge test is not sufficient to determine the actual transfer function during the cutting process. This can have several reasons: stroke points were limited and did not cover the whole front face; it was not allowed to stroke directly on the disc cutters; the transfer function for each point was too different to be summed up.

Another study of the transfer function on a soft ground TBM showed similar results (Walter, 2013). This work states that the comparison between striking similar types of cutting teeth, yields dissimilar results and, therefore, a distinct transfer function could not be realized.

4. Gripper as a possible seismic source

The reaction forces due to the thrust forces and rotating of the TBM head are compensated by the gripper. This is maybe another source for seismic waves, however as mentioned in the hypotheses in the Introduction, they had not been regarded until now. Therefore accelerometers (axial and radial to the tunnel axis) were installed on grippers, approx. 7.3 m behind the tunnel face (Figure 4.1) at Reisseck, where an open gripper-TBM was used. Only this data set is available, as in the other projects no further sensors were installed on grippers.

4.1. Description and comparison of sensor signals

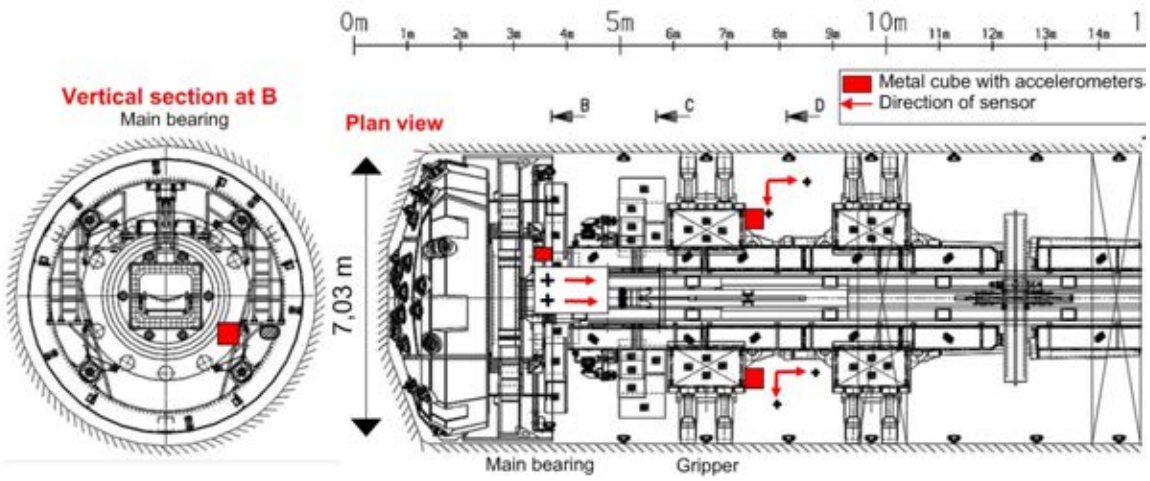

Figure 4.1.: Position of accelerometers at the gripper TBM - Reisseck; scheme of position in vertical and horizontal section; in each cube are two accelerometers in axial and on the gripper also in radial direction

Only the axial and radial component of the right gripper (TBMR-A and TBMR-R) could be analyzed. The left gripper was not activated all the time due to technical reasons. Figure 4.2 shows an appropriate section of the signal and also the axial pilot signal of the main bearing. The amplitudes of the axial gripper sensor TBMR-A is approx. 1/5 of the amplitude of the axial sensor at the main bearing and has 3 times larger values than the radial component. The main frequencies are < 200 Hz for every pilot signal. The main peak for the axial sensor at the main bearing is at 70 Hz. The

maximum peaks are the same for the gripper position, whereas the higher peaks appear at 110 Hz and 155 Hz (Figure 4.3).

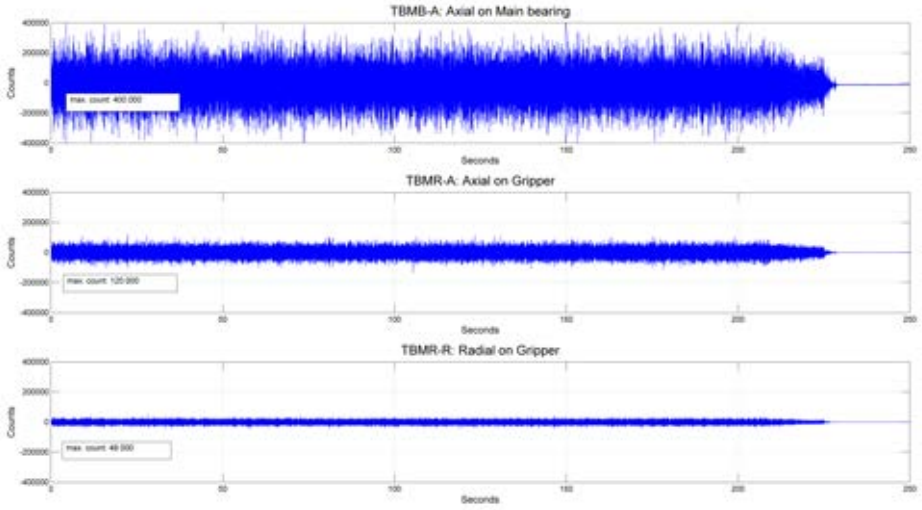

Figure 4.2.: Comparison of amplitudes of the axial component at the main bearing TBMB-A with the axial and radial component at the right gripper TBMR-A and TBMR-R. The highest amplitude has TBMB-A. The axial component of the gripper is 3 times larger than the radial component.

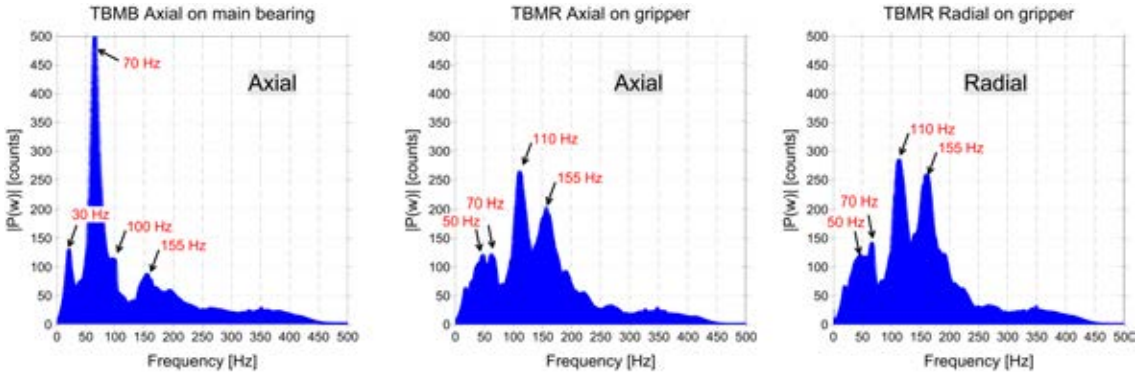

Figure 4.3.: Frequency content of axial component at main bearing TBMB-A and the two components on the right gripper TBMR-A and TBMR-R.

4.2. Comparison of the forward and backward recorded p-wavelet

The minimum delay transformation with the gripper components at Reisseck shows similar results as with the main bearing components, although the s-wave is imaged

clearer (see Appendix B). Therefore, the signal on the gripper can be regarded as a worse recording position for the signals coming from the cutter head. On the other hand, if the grippers are a further source for seismic waves, this position would be optimal. Dependent on the TBM-type, they are 7-10 m behind the cutterhead.

In general, if several sources radiate seismic waves, which differs in space, a receiver would record the superposition of these waves. The signals would differ in amplitude, phase, frequency and have different traveltimes. In case of a TBM, the traveltimes are first shorter for the cutterhead signals, but for the backward radiated waves, the traveltime of the gripper signals are shorter. Therefore the recorded signal at a receiver in front of a the TBM (forward radiated wave field) should be different to the recoded signal, when the TBM has already passed the receiver stations (backward radiated wave field). The largest difference would be on a receiver parallel to the tunnel axis (Petronio and Poletto, 2006).

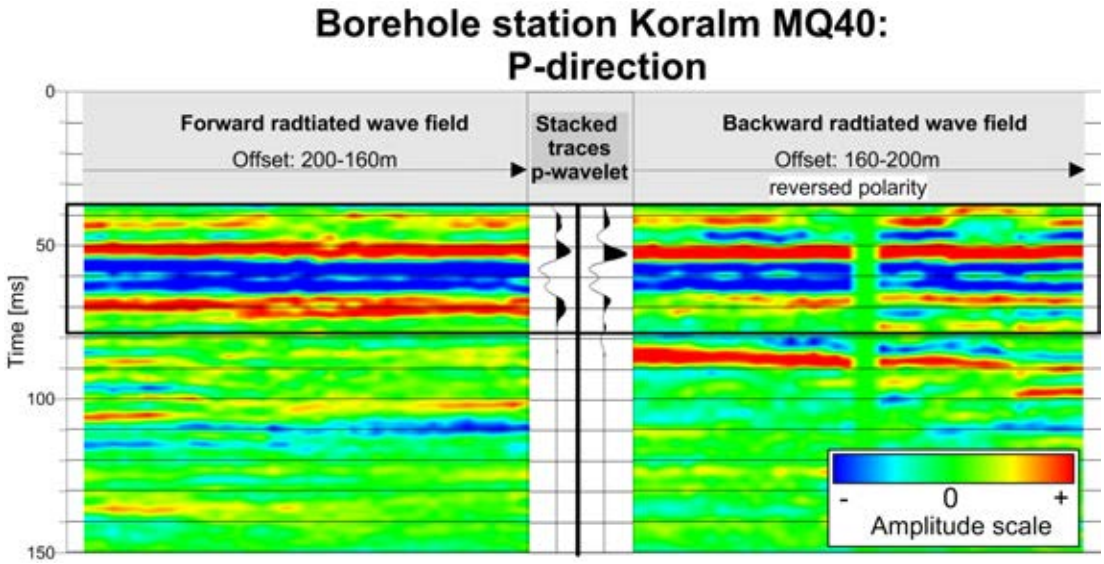

Figure 4.4.: Data of the borehole station MQ40 at the tunnel Koralm; the left side shows in p-wave direction rotated data of the forward radiated wave field (in advance direction of the tunnel). The section is 40 m long and the offset varies from 200 to 160 m. The data with the same offset, but for the backward radiated wave field (against the advance direction) is shown on the right side. The amplitudes are reversed. The stacked traces of each section are shown in the middle. All traces were aligned to the p-wave.

Figure 4.4 shows the p-wavelet on traces recorded at the cross-section MQ40 of the tunnel Koralm. This receiver was chosen, as the geophones are situated deep within the solid rock, so there is no influence of a free surface, and the TBM-north passed the position. The minimum delay transformation was done with an axial component on the main bearing. The traces are within the same offset in forward and backward

position to the TBM. The p-wavelet is around 30 ms long and has a different polarity in the backward section. Therefore the traces are reversed presented in the backward section. The stacked traces of these 40 m have almost identical p-wavelets. There is just a slight difference in the strength of the amplitude, but not in the shape of the wavelet. Thus it can be concluded, that the signals are generated by one source, the TBM cutterhead. Within the scope of this thesis, the grippers are therefore not considered as a further source.

Certainly, this is maybe not valid for each TBM and rock condition, as the use of the grippers depend on the TBM type. The recorded data set at Reisseck has significant amplitudes. It cannot be excluded that the transmitted forces into the rock is relevant. However, this data set could not be compared with similar data, as in the course of the projects no further sensors were placed on the grippers.

5. Cutting process - the main seismic source

The disc cutters are pressed against the tunnel face, which leads to fracturing of the rock. We assumed that this is the source of the seismic waves. For a better understanding of the cutting process as seismic source it is necessary to know the directions of applied forces, the direction of the occurring cracks and their failure modes, as this determines the seismic wave radiation pattern.

As already mentioned in the introduction, we hypothesized that the source mechanism for tunneling with a TBM is a single force. It means that a force is acting in axial/advance direction of the tunnel. Further mechanism were not considered until now. Within this chapter studies relating to the cutting process are presented. Possible source mechanism, which results in generation of seismic waves, are pointed out and discussed.

5.1. Rock fragmentation models

Many studies regarding the hard rock cutting process have been documented (Lindqvist et al. (1984), Cook et al. (1984), Pang and Goldsmith (1990), Mishnaevsky JR (1995), Gehring (1995)). They all agree that in general the contact pressure between the disc cutter and rock pulverizes the rock beneath the cutter and forms a crushed zone. With each pass the thereby formed kerf is deepened in the tunnel face. The stresses from the thrust of the cutter are transmitted into the adjacent rock causing further cracks initiated from the crushed zone. Cracks propagate, also parallel to the free surface with increasing penetration. When cracks between two cutters coalesce, they form a so-called chip. This kind of rock fracturing with disc cutters is named chipping process. Normally the chips should be formed after 2-3 passes of a cutter. To achieve the best performance the distance between two adjacent tracking cutters (kerf spacing) and cutterload must have suitable values for each rock type.

The complexity of rock fragmentation with disc cutters is still under research to yield a closer model to the reality. The focus is the development of fragmentation models, which determines the creation of the crushed zone, the development and direction of the cracks and their failure modes. The failure mechanism of rock cutting have been investigated mainly by means of indentation testing, which is suitable for the

disc cutting (Lindqvist et al. (1984), Cook et al. (1984), Howarth and Bridge (1988a), Pang and Goldsmith (1990), Gertsch (2000)). The reviews of Lawn and Wilshaw (1975) and Mishnaevsky JR (1995) give a good overview of indentation fracture in brittle solids. The observations made by nearly all researches have confirmed the existence of the crushed zone, which is developed due to the high normal forces under the cutters, whereas the formation and mechanics of the induced cracks are topic of many discussions.

Lindqvist et al. (1984) observed the development of indention fractures continuously in a scanning electron microscope (SEM). He described a long median crack and cracks in radial directions. Further the length of the cracks is a function of the pressure, which in turn is a function of the cutter normal force. Rostami and Ozdemir (1993) presented a model for a standard 17 inch disc cutter, with tensile cracks and a dominant median crack. The authors assumed that the tensile fracture initiation and propagation is the principal means of chip formation, and consider it to be the major failure mode. They noted, that around the crushed zone also shear stresses occur and therefore a mixed failure for chip formation is closer to reality.

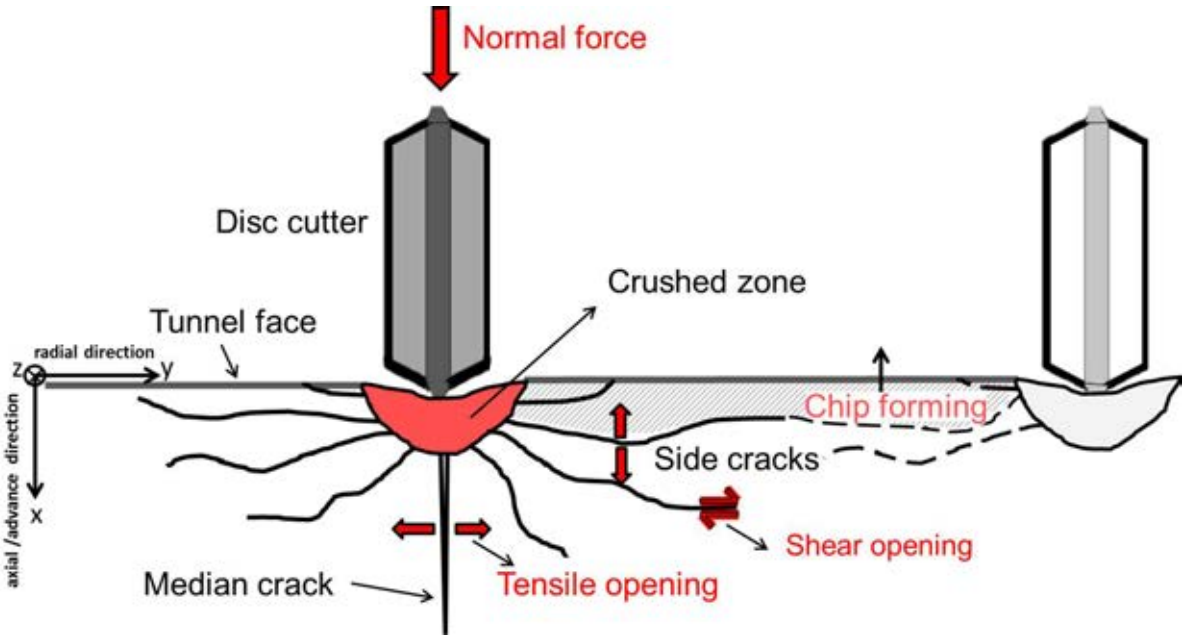

Figure 5.1.: Rock fragmentation and chip formation by disc cutters (modified after Rostami and Ozdemir (1993)). Red arrows show the direction of force and the possible generation of tensile and shear cracks.

The work of Zhang et al. (2003) is one the rare studies of rock specimens, that were exposed to disc cutting. They analyzed rock cores taken from a tunnel face in Sweden and reported also deep median cracks as well as distinct lateral cracks. Similar results

were found by Howarth and Bridge (1988b). The resulting directions of the cracks of the mentioned work were gained from testings under no or low confinement level, which is not comparable to the situation at the tunnel face. There the confinement is closely related with high overburden, which results in high primary stresses.

The tensile behavior or the crack has also been described by Cook et al. (1984), who carried out stamp indentation tests with acoustic emission (AE) measurements and different confinement levels. In the study the author correlated the expansion of the crushed zone with AE events and observed a transition form split tensile failure at no confinement to a lateral cracking system at higher confinement levels.

The change of the crack direction under higher confinement level was investigated by Chen and Labuz (2006). They observed large median crack at low confinement levels, whereas the direction of cracks turns into a lateral direction at higher confinement levels. Similar results of cutting process under high stress confinement are described by Innaurato et al. (2007).

Entacher et al. (2015) showed on examples on full scale and small scale cutting tests, that the crack directions differ significantly depending on the confinement situation. They reported that in a non-confined or insufficiently confined situation, a large median crack will be pre-dominant. Passive confinement is defined at the state of the first cut in scaled rock cutting tests or of an undamaged tunnel face in areas with low overburden. Thereby cracks develop mostly in the lateral direction. In contrast to this, active confinement, which is representative of a tunnel with high overburden. Due to the added pressure, cracks develop almost horizontally. The same confinement situation in foliated rock completely changes the crack pattern due to pronounced planes of weakness. The authors mentioned that situation at a tunnel face is typically a combination of all varying confinement. The confinement depends not only on primary stress, but also on the position of the cutter (center, inner or outer area on cutter head), rock mass properties and pre-damage of the tunnel face.

Despite the experimental work, there exists various attempts to study the rock failure by numerical simulations. Huang et al. (1998) reports results of a numerical analyses with a Finite Element Method (FEM)-code to investigate the influence of different confinements on the development of and initiation of tensile fractures. Liu et al. (2002) presented their 2D-FEM code R-T^{2d}, which is able to simulate the fracturing within heterogeneous material and different confinement levels. They say that the side crack initiate from the crushed zone are driven by tensile stress associated with the zone, which finally intersect with the free surface to form a chip. Both simulation showed, that the direction of the tensile cracks are dependent on the confinement level.

Further research and modeling of the rock failure consider different rock properties,

anisotropy and confinement level using FEM codes (Wang et al. (2011) and Ma et al. (2011)). Gong et al. (2005) presented a Distinct Element Method (DEM) to model the rock fragmentation. Others use DEM-codes such as PFC (Particle Flow Code) (Thuro and Schormair (2008),Su and Akcin (2011)). Tan et al. (1997) and Marji et al. (2009) simulate fracturing with the Displacement Discount Method (DDM).

Most of the results of the presented studies address fracturing with a single indenter or cutter. They show that the side cracks vary in direction due to different rock properties, consideration of confinement and the numerical possibilities. The failure modes are mainly described as tensile, but also shear failure is mentioned. However the chipping process is determined by the interaction of adjacent cutters (Wang 2011, Moon and Oh 2011), differing rock properties (e.g. anisotropy effects), stress conditions and also by operation of the TBM (e.g. applied thrust force, torque, revolution per minute). The influence of the wear of the cutters has to be considered and is also subject of the TBM performance prediction. There is vast literature regarding the performance prediction, for instances Gehring (1995), Cigla and Ozdemir (2000), Gertsch et al. (2007), Rostami (2008) and Schneider et al. (2012). Some researchers take the wear of the cutters into account. Their models prove the influence on rock fragmentation Thuro and Schormair (2008), to mention one.

5.2. Cutter force measurements

Some of the mentioned papers in chapter before compare the failure process with corresponding forces or energy input. It is generally accepted that the majority of cutting energy is consumed in the formation of the crushed zone and that only a few percent (3-15 %) are consumed for crack propagation and thus for efficient chipping. (Lawn and Wilshaw (1975), Lindqvist et al. (1984), Mishnaevsky JR (1995), Gehring (1995)). A typical force - displacement curve of indentation and cutting tests have a sawtooth shape with a number of significant force drops Entacher et al. (2012). Figure 5.2 present their result of measured forces in three directions: normal force F_N, rolling force F_R and side Force F_S during a cutting test. The diagram shows that most of the applied force is acting normal to the rock face.

Entacher et al. (2015) hypothesized that force peaks and subsequent sudden energy release with a rate above a certain threshold indicates trans granular mineral breakage in the direct proximity of the cutter tip, i.e. within the crushed zone. Initiation of cracks or chipping consumes only small parts of the total cutting energy. These events cause irregularities in the force graph such as changes in slope, e.g. less steep further

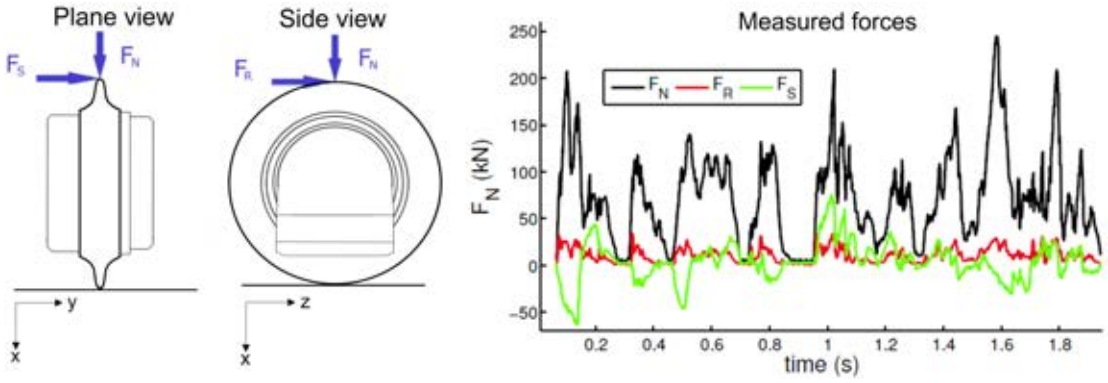

Figure 5.2.: left: Definition of cutting forces directions; right: measured forces during a linear cutting test (Entacher et al., 2012)

force increase or steep force drops but at much smaller rates.

These results are from testings in laboratory scales. The applied forces at cutters on a TBM are usually derived by dividing the total thrust by the number of cutters, which gives an approximate average loading of 250 kN for a typical 17" cutter. However, laboratory cutting tests infer that the loading of a cutter oscillates strongly and can reach peaks that are a multiple of the average forces.

One of the first measurements of cutting forces on the TBM were carried out by Samuel and Seow (1984) and Zhang et al. (2003). Theses measurements were only possible for short periods of drilling. To gain a continuous recording of the cutting forces Entacher et al. (2012) developed a measuring system for forces of an individual disc cutter on the TBM in real time.

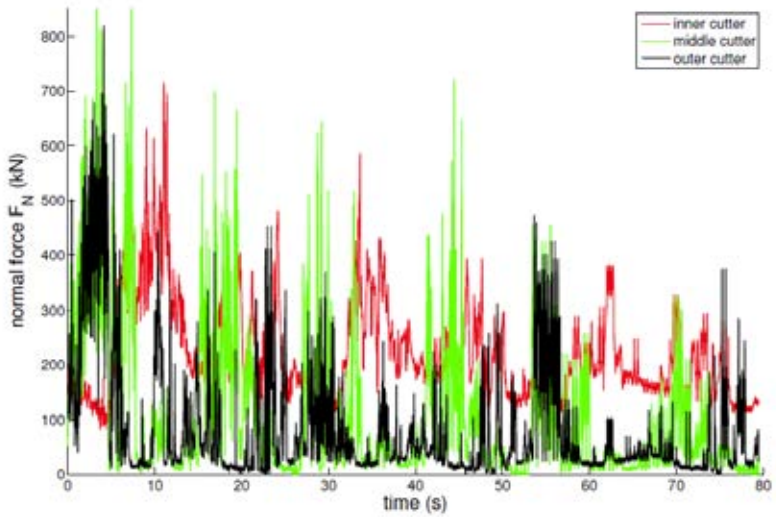

Figure 5.3.: Normal Force F_N plottet against time, Entacher et al. (2013)

Results of an first application on the TMB at Koralm (Entacher et al., 2013) revealed that peak forces are a multiple of average forces and that the distribution of forces across the tunnel face can be very irregular. It is also dependent on the position on the TBM head (inner, middle and outer position in Figure 5.3). They correlated the measured forces with the encountered geology at the tunnel face and showed a good correlation between compacted and fractures zones.

Based on the literature, it is possible to assume seismic sources. Most of the cutting energy is needed to form the crushed zone beneath the cutter. Thereby huge normal forces in axial direction (parallel to the tunnel axis) occur. This is regarded as the main seismic source mechanism, which can be described as a single force in axial direction. A further possible source of seismic waves are the induced cracks, which are formed with the rest of the energy in various directions. Depending on the level of confinement median or radial cracks might occur. The failure mechanism of the cracks is mainly describe as tensile fracture, but also shear cracks can occur.

6. Observation of radiation pattern

This chapter describes the measurements of seismic waves radiated by the TBM and recorded by geophones, which were situated above the tunnel axis on the surface and in boreholes in the tunnel wall. The exact location and registration parameters are described. For the comparison of the different receivers a spatial coordinate system had to be implemented to determine the ray paths. A weathered surface layer was assumed for the ray path determination of the surface receiver. The influence of the free surface on the amplitudes is not considered. As the receiver components had different directions, the seismograms were rotated in the p-wave and s-wave directions and presented afterwards. All further results are based on the rotated data set. By analyzing the polarization of the first motion of p-wave and s-wave the radiation pattern can be described. With the help of the amplitude ratio of the p-wave to s-wave further information regarding the source mechanism is gained.

6.1. Receiver locations

The field data are the recordings of 3-components geophones, which are installed at the surface, situated directly above the tunnel axis and also with lateral offset. Additional, borehole geophones are placed in the wall of one tube of a two-tube tunnel. The data sets contain the forward and backward radiated wave field, as the TBM passed their positions.

The surface receivers were three 15-Hz single geophones, which were installed in a wooden cube to form a 3-component system. This wooden cube was fixed with a long nail to the rock. It was tried to place this cube at least on rocks and not in the soft soil on the surface, as the locations were in a rocky environment. Two horizontal components (axial and radial) and one vertical component (tangential) were installed. The continuous recording system was a Reftek 130 with a sampling rate of 1000 Hz, the same settings as for TSWD. Each station was equipped with a GPS antenna. Therefore the exact position in a local coordinate $x_{rec}, y_{rec}, z_{rec}$ system is known. The directions of the geophone components were measured with a magnetic compass. The axial direction was approx. aligned to the tunnel axis. The clients of the tunnel sites provided the coordinates for the tunnel axis as well as the positions of the borehole receivers. The tunnel axis coordinates $x_{tbm}, y_{tbm}, z_{tbm}$ refer to the center of the tunnel tube and will be named in the following as tunnel axis (TA).

The figures 6.1 to 6.3 show maps and location of the surface receivers. They include also the direction of the geophones components. At Reisseck and Koralm the surface station could be placed nearly above the tunnel axis with an overburden of 100 and 250 m. At Bärenwerk the surface position was approx. 120 m beside the tunnel axis and approx. 120 m above. Figure 6.2 shows also the geophones stuck in the wooden cube. The stations were installed at a distance of max. 350 m in advance to collect also the forward radiated wave field. The TBM passed the locations in the underground and the records were stopped after further approx. 300-400 m of tunneling. Only at Reisseck the direction of the tunnel axis changes in the beginning. The other tunnel axes were more or less in a straight line in regard to the receiver positions.

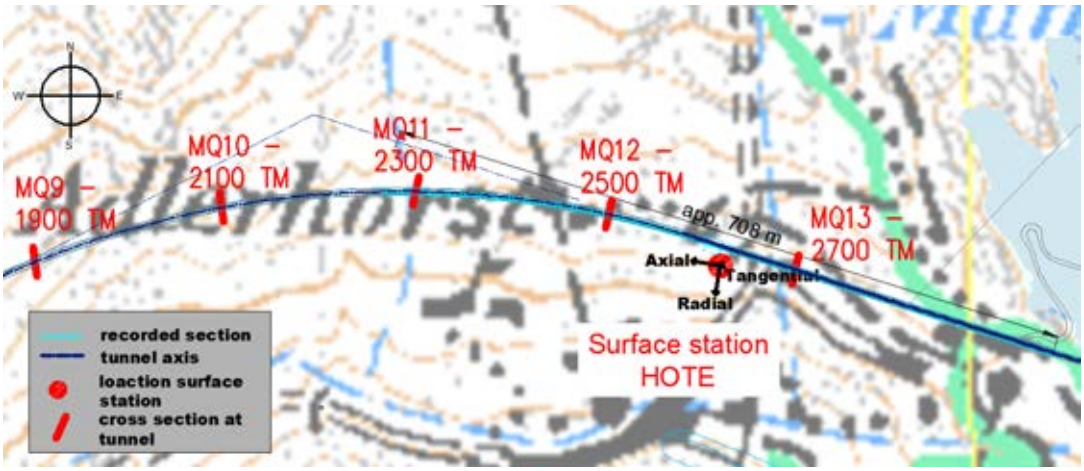

Figure 6.1.: Map of the tunnel axis at Reisseck including measured section and position of surface station HOTE and cross sections along tunnel.

The TSWD system at Koralm was installed at the TBM-south, but during the advance the TBM-south had to stop, whereas TBM-north went on. So pilot sensors were installed on the TBM-north and synchronized in time with a second atomic clock. As the TBM-north moved forward it passed the measuring cross-sections MQ39, MQ40 and MQ41, which were installed in the tunnel tube south. The distance between the two tunnel tubes is only 40 m. So the second TBM was a very good source to measure the forward and backward radiated wave field on the right geophones (right - if you look in advance directions). In the scope of this work the left geophones were not analyzed due to a not known influence of the existing tunnel.

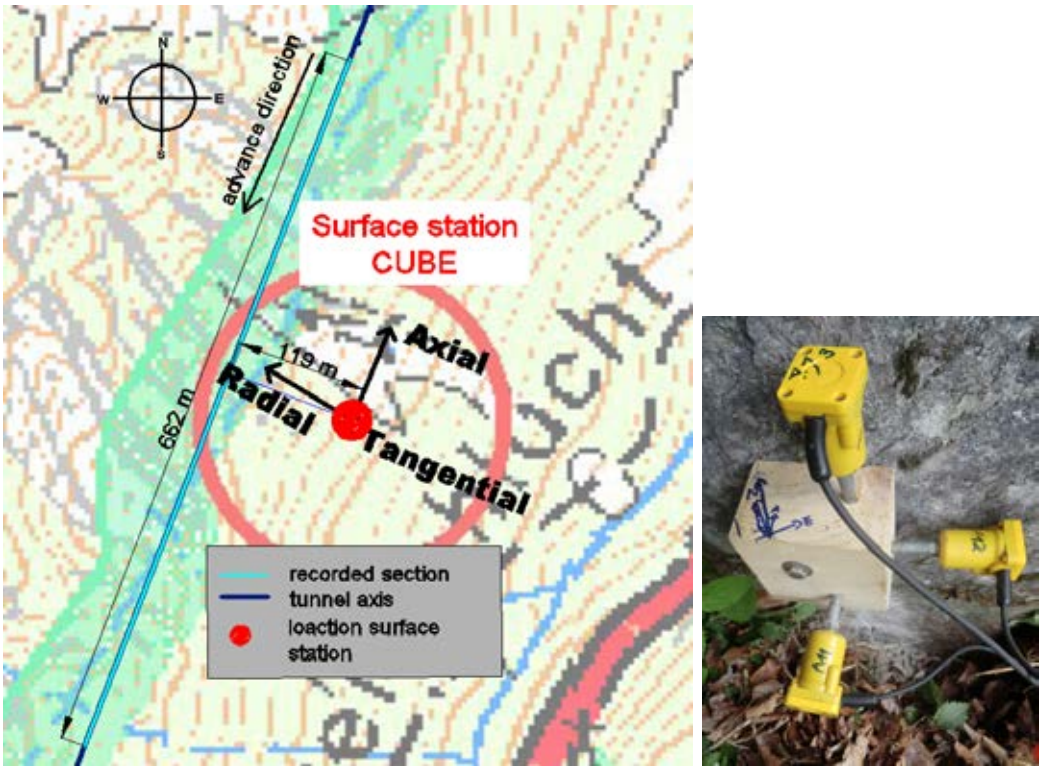

Figure 6.2.: Map of the tunnel axis at Bärenwerk including recorded section and position of surface station CUBE and the geophones stuck to the wooden cube.

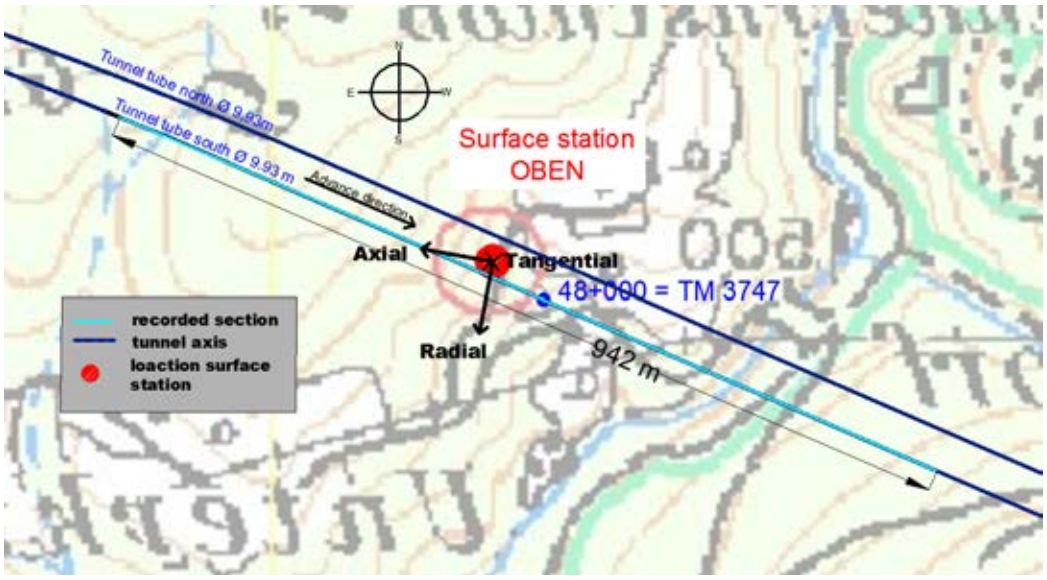

Figure 6.3.: Map of the tunnel axis at Koralm including recorded section and position of surface station OBEN.

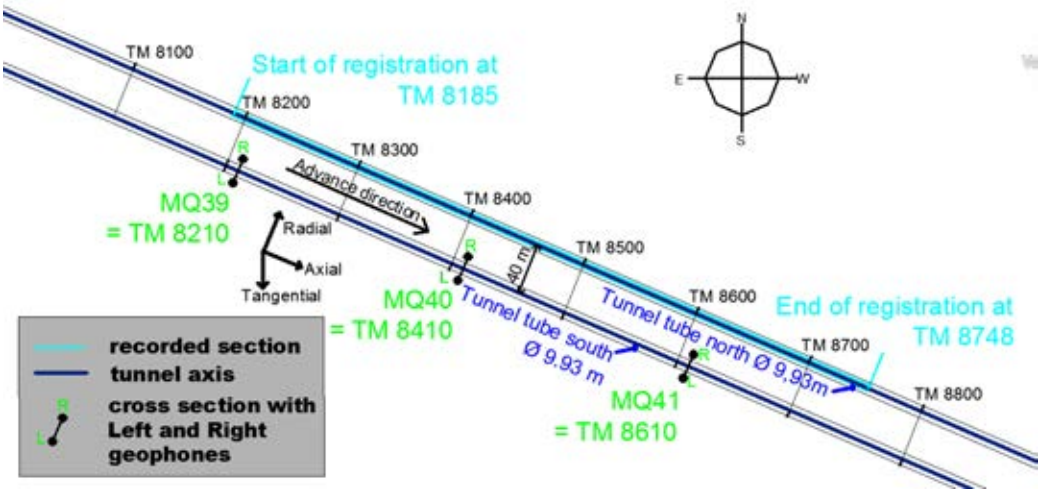

Figure 6.4.: Map of the tunnel axis at Koralm including the measuring cross-sections MQ39, MQ40 and MQ41, as well as the recorded section.

6.2. Ray paths

6.2.1. Definition of angles between the TBM and receiver position

For the comparison of the different receiver data first a space - fixed coordinate system was implemented, which has it's center at the tunnel axis (TA). The receiver is fixed, whereas the TBM is moving along the tunnel axis. This axis corresponds to the x-axis, the direction DR, which is perpendicular to the tunnel axis in a horizontal plane, to the y-axis. The direct wave path (rr), from the TBM position at the tunnel axis to the receiver location, can therefore be determined in space with the angles Theta and Phi (Figure 6.5). The angle Theta is defined in the horizontal plane as the angle from the radial direction (DR) in clockwise direction towards the tunnel axis (TA). It defines the horizontal ray path, so at Theta = 90° is the path in the direction of the tunnel axis. The dip angle Phi starts from the horizontal plane upwards to the vertical axis (V). As the bin size for the seismic trace is 1 m, the angles Theta and Phi are determined for each drilled meter.

The direct wave path (rr) can be determined as followed:

$$rr = \sqrt{(x_{rec} - x_{tbm})^2 + (y_{rec} - y_{tbm})^2 + (z_{rec} - z_{tbm})^2} \tag{6.1}$$

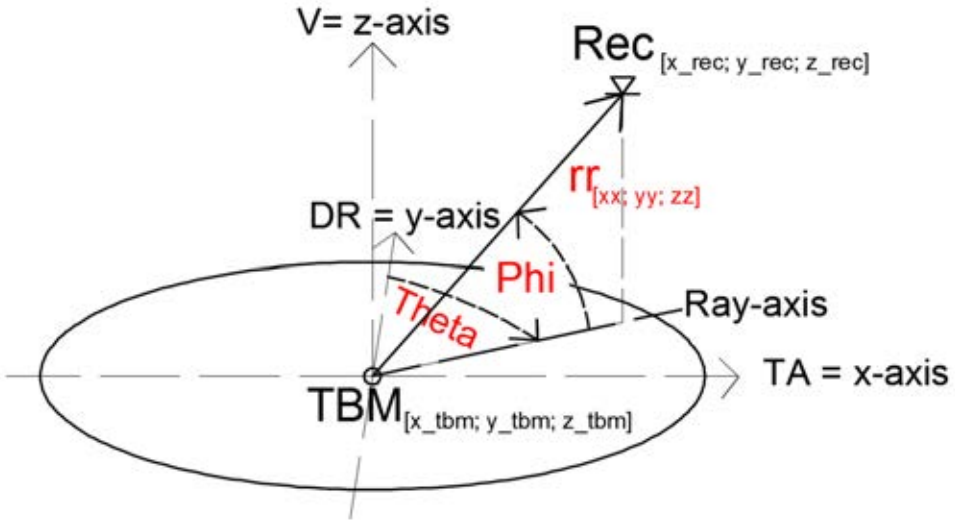

Figure 6.5.: Definition of angle Theta and Phi between the TBM positions on the tunnel axis and the receiver position. TA is the tunnel axis and corresponds to the x-axis, DR direction is perpendicular to the tunnel axis in the horizontal plane and corresponds to the y-axis, V is the vertical axis corresponding the z-axis.

6.2.2. Consideration of a weathered surface layer

The assumption of the direct wave path is only valid in full space - so for the borehole stations MQ39-41. For the surface receivers a weathered layer has to be considered, which changes the incidental angles of the direct waves (Figure 6.6). With a model containing a 5 m thick weathered layer with a p-wave velocity (v2) of 1000 m/s the angles for the new dips in the surface layer (Phi2) and in the solid rock layer (Phi1) with a p-wave velocity (v1) of 5000 m/s were determined according to Snell's law that determines:

$$\frac{sin(Phi1)}{v1} = \frac{sin(Phi2)}{v2} \tag{6.2}$$

A routine calculated the corresponding angles for all incidental angles at the source point between 0 – 90 ° with a step size of 0.01°. The difference of the absolute lengths of the generated paths within layer 1 and layer 2 and the direct path (rr) is determined. The minimum difference determine the correct Phi1 and Phi2 values.

The new Phi2 angles are between 78° - 90°, so nearly vertical to the surface. Therefore the vertical components (tangential) should contain most of the p-wave amplitudes.

Most times the receivers were situated not on flat surfaces. So the model is just a simplified one, which does not account the slope of the surface and layers in the

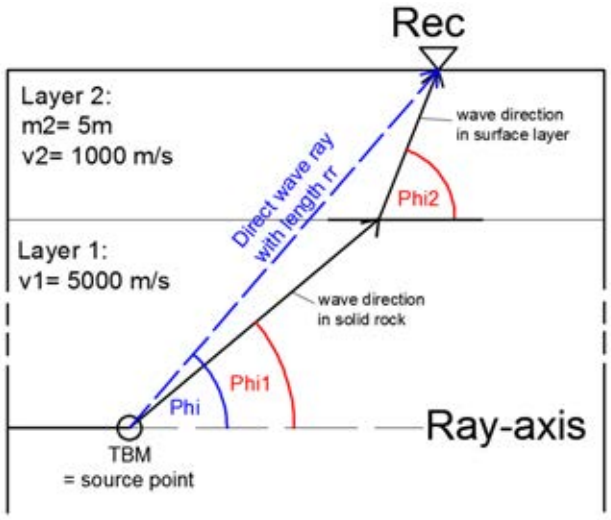

Figure 6.6.: A weather layer with a thickness of 5 m is assumed under the surface stations. Therefore the incidental angle Phi changes according to Snell's law. The new angles Phi1 and Phi2 are determined.

subsurface. This simplified model is used for all three surface stations, as the rock velocities were in the same range. A short refraction seismic profile at the receiver location would have helped to obtain the real layers with velocities and thickness. However in the scope of this work these measurements were not available.

6.2.3. Rotation into of p- and s-wave directions

The radiation pattern describes the first motions of the p-wave and s-wave. Therefore the field data sets had to be rotated into the corresponding p-wave and s-wave directions of motion.

The directions are determined as followed:

P - direction: polarization along the path from TBM to receiver (rr)

S1 - direction; polarization in the plane of P - direction and the tunnel axis (TA)

S2 - direction; polarization perpendicular to P and S1 - in order to generate a right-hand system.

The p-wave runs along the direct path (rr) in full space, for the surface stations, the calculated directions due to the surface layer was considered. The S1-direction lies in the plane, which is determined by the tunnel axis and the P-direction. Thereby the direction is chosen according to the positive polarization direction of the s-wave in the single force model (see the given s-polarization direction in a plane in Figure 1.10).

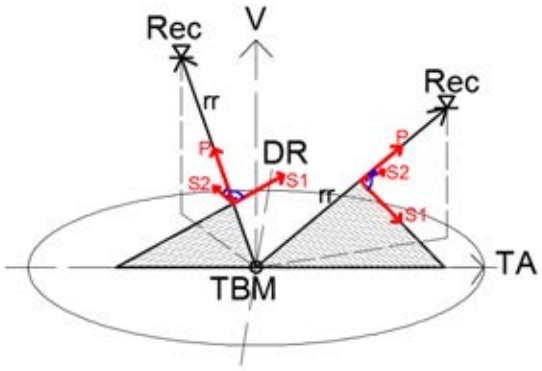

Figure 6.7.: Definition of direction of P, S1 and S2. The P-wave direction is the path (rr) from the source (TBM) to receiver position, S1 lies in the plane of the tunnel axis (TA) and the P-wave direction, S2 is perpendicular to P and S1; Two positions and their corresponding P-S1-S2 directions are shown one in and one against the advance direction.

6.2.4. Receiver position projected to focal sphere

It is convenient to display the radiation pattern of seismic source mechanism on the focal sphere, which has a infinitesimal radius around the source point. The observations, of course, are at station some finite distance from the source. Thus it is needed to convert the observations at the receiver stations to hypothetical ones surrounding the source (Stein and Wysession, 2003). In this system the TBM position is fixed at the center and the receiver moves relative to the TBM. The angle Delta is therefore the ray's angle of incidence at the source point along the tunnel axis to the receiver (Figure 6.8). It corresponds to the angle Theta.

The measured sections are now determined through Epsilon, which corresponds to Phi and Phi1 and ranges from 0-360° starting from the horizontal plane in clockwise direction. Delta lies in the plane of the ray path and the tunnel axis. The values range between -90° to 90°, where negative angles correspond to the backward radiated wave field and the positive angles to the forward radiated wave field. The angle 0° is perpendicular to the tunnel axis.

Figure 6.9 shows the measured sections of the surface and borehole receivers on a sphere with a dimensionless radius 1.

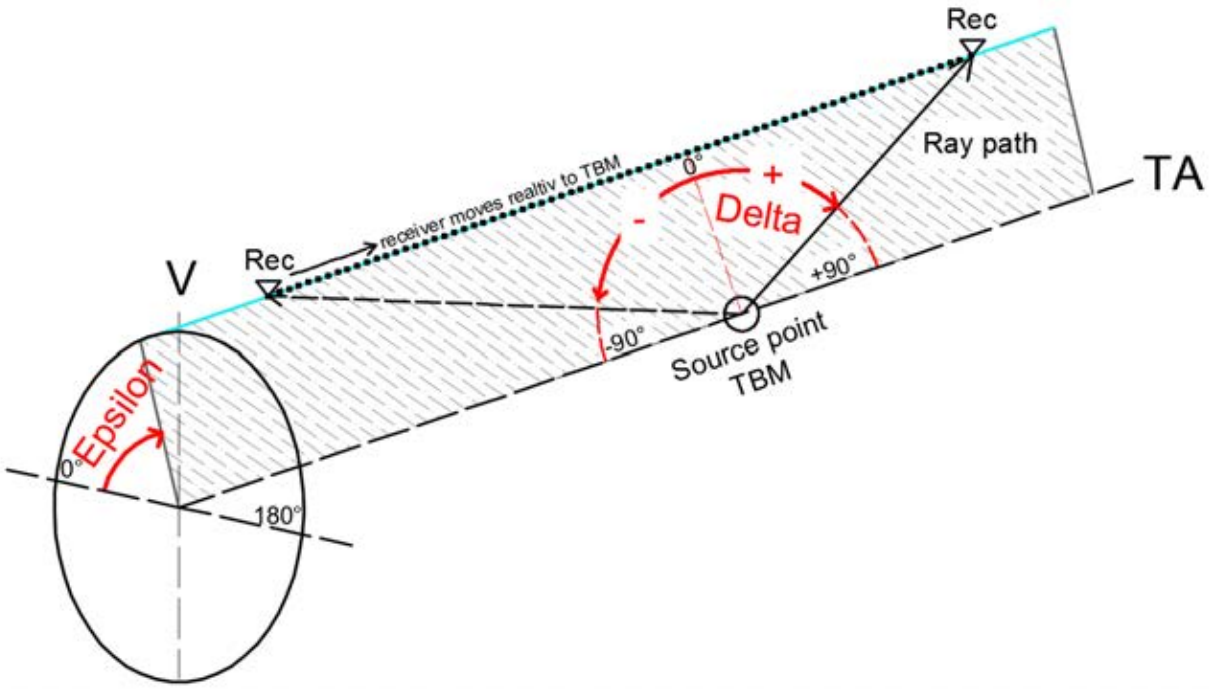

Figure 6.8.: Determination of angle Delta and Epsilon between the TBM position in the center and the receiver locations. In this example the angle Epsilon is always the same, but this is not necessarily valid for every recording position.

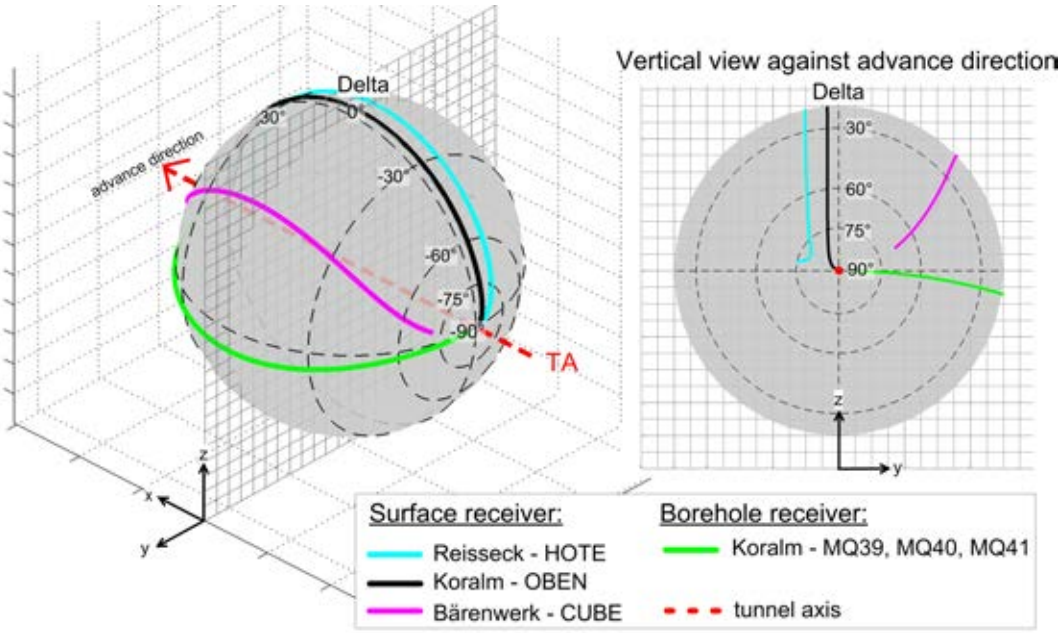

Figure 6.9.: The measured sections of the surface receivers and borehole receivers are plotted on a sphere with radius 1 in different views. The positions are determined by Epsilon and Delta.

6.3. First break picking

Before analyzing the first motions of the p-wave and s-wave, the traveltimes of the first break picks had to be determined. With the help of a sta/lta ratio (short time average – long time average) applied on the reflection strengths, the first break picks were set for the p-wave and the s-wave. The sta- and lta - values were generated with a different length of smoothing of the reflections strength for each trace. The beginning of the maximum is considered as the beginning of the p-wave and s-wave wavelets. Only in sections where the determination is clear, the first break picks were set (Figure 6.10). The picking on the reflection strengths guaranteed, that the first breaks were set without any polarity predetermination of the waves.

The borehole receivers in the tunnel were very close to the source (min. 35 m), so the travel times for p- and s-waves are very short. As the wavelets for the p-wave are very long, they overlap in the near offsets with the s-wave wavelets. For Delta values between -40° and +40° (offsets up to 80 m) the p-wave first break could not be determined. These limitations are not valid for the surface receivers as the travel times are three times longer for the nearest offsets and therefore the p- and s- wave wavelets are separated. In general the s-wave first breaks are clearer in the near offsets but get worse in the far offsets.

The surface data has been already aligned to the p-wave. This picking was done individually on the raw data. The sta/lta ratio should confirm or correct the existing first break picks. Figure 6.10 shows two examples, one for a the borehole receiver (MQ40) and one surface receiver at Reisseck (HOTE). The results of the other receiver stations are shown in Appendix C.

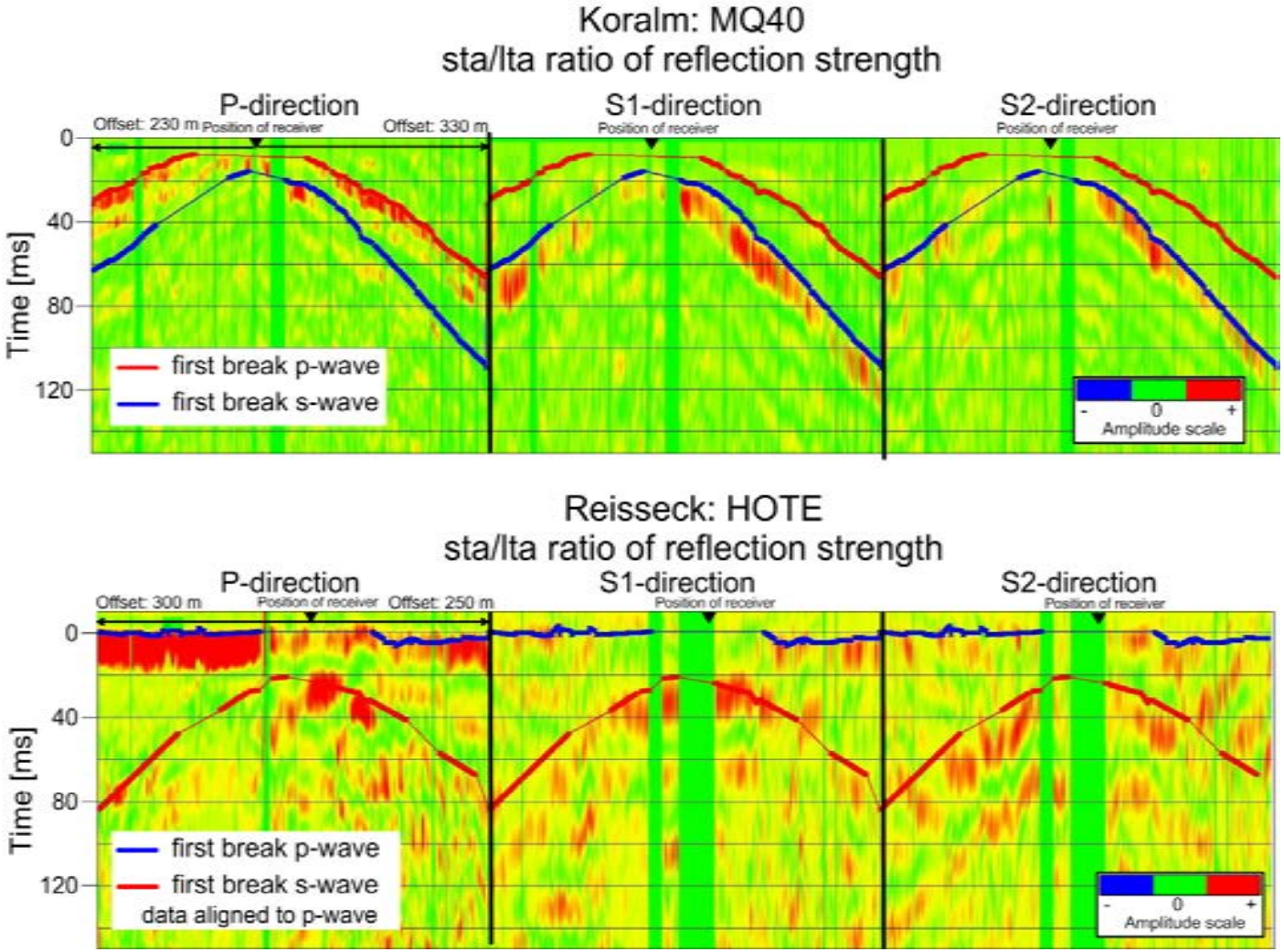

Figure 6.10.: Sta/lta ratio of the reflection strength for borehole receivers MQ40 on all components. The first breaks for p-wave and s-wave were set at the beginning of the maximum; the data of the surface station HOTE was already aligned to the p-wave. At near offsets the p-wave first break could not be determined.

6.4. Seismograms of rotated field data with first breaks

Figures 6.11 - 6.13 present the rotated data into p- and s-wave directions of the borehole stations. At MQ40 it was possible to collect the forward (positive Delta) and backward (negative Delta) radiated wave field, as the TBM passed this cross-section. MQ39 only contain the backward and MQ41 only the forward radiated wave field. After the first break picking the breaks were interpolated for the uncertain sections (black lines with square = p-wave, with dot = s-wave). The traces with small offsets are not shown in the P-direction, as it was not possible to separate the p- and s-wave signals. The amplitudes are normalized, but no further filtering is done. Above each seismogram the corresponding angle Delta is plotted.

There is a clear change in the polarization of the p-wave in the p-direction in the seismogram of MQ40. The wavelength of the p- wave is smaller than the s-wave wavelength. The s-wave at the S1-directions does not change its polarization, but the signals in the forward section is no so clear as in the backward section. This is also valid for the S2-direction, where the signal in general has more correlation noise (amplitude maximums before the first break). A change of the wavelengths from the backward to the forward section is not seen.

In the seismograms of MQ39 the p-wave polarization is only negative as only the backward section is registered. The S1- and S2-direction are very similar and clearly reveal the positive polarization of the s-wave.

In the forward section at MQ41 the p-wave polarization is only positive, such as the s-wave at the S1- and S2-directions. On the S2-direction also a weak p-wave is visible.

The surface stations seismograms are aligned to the p-wave. In the S1 and S2 directions p-wave amplitudes are also visible, which can be due to not exactly determined ray paths (discussed in Chapter 6.2.2 Consideration of a weathered surface layer). The full dataset is presented, as the receivers were at least 110 m above the TBM positions, so the p-wave and s-wave are clearly separated.

In the seismograms of HOTE (Figure 6.14) the p-wave is strong at large offsets, whereas at near offset the p-wave nearly disappears and the s-wave dominates. The wavelength of the p-wave is smaller in the forward section and the polarization changes. The signals in the seismogram of CUBE in Figure 6.15 are generally less frequent than all the others. The p-wave first break is very weak, the s-wave dominates in all sections. Only at far offsets the p-wave is stronger. In the S1-seismogram the s-wave is only clearly detectable in the backward radiated, in the S2-seismogram only in the forward radiated section. Figure 6.16 shows the results of the surface station at Koralm. It contains the longest measurement section over 900 m. The p-wave is clearly revealed

in the backward section, but in the forward section it is very weak. At near offsets the s-wave dominates. In general the data quality is the lowest of all receiver stations. This can be related to the bad coupling to the underground on the surface.

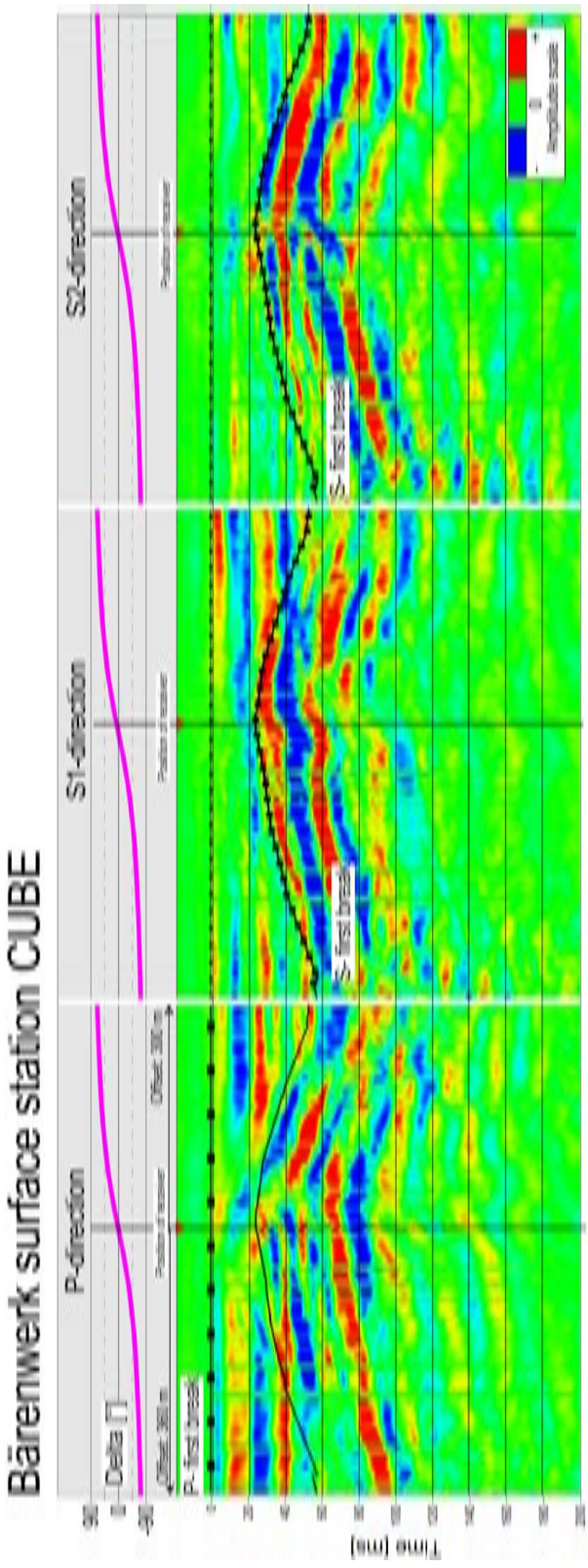

Figure 6.15.: Rotated seismograms of the 3C- surface-geophone CUBE; above the seismograms the corresponding angle Delta is shown. Data is aligned to p-wave, the black lines indicate the p- and the s-wave first break picks.

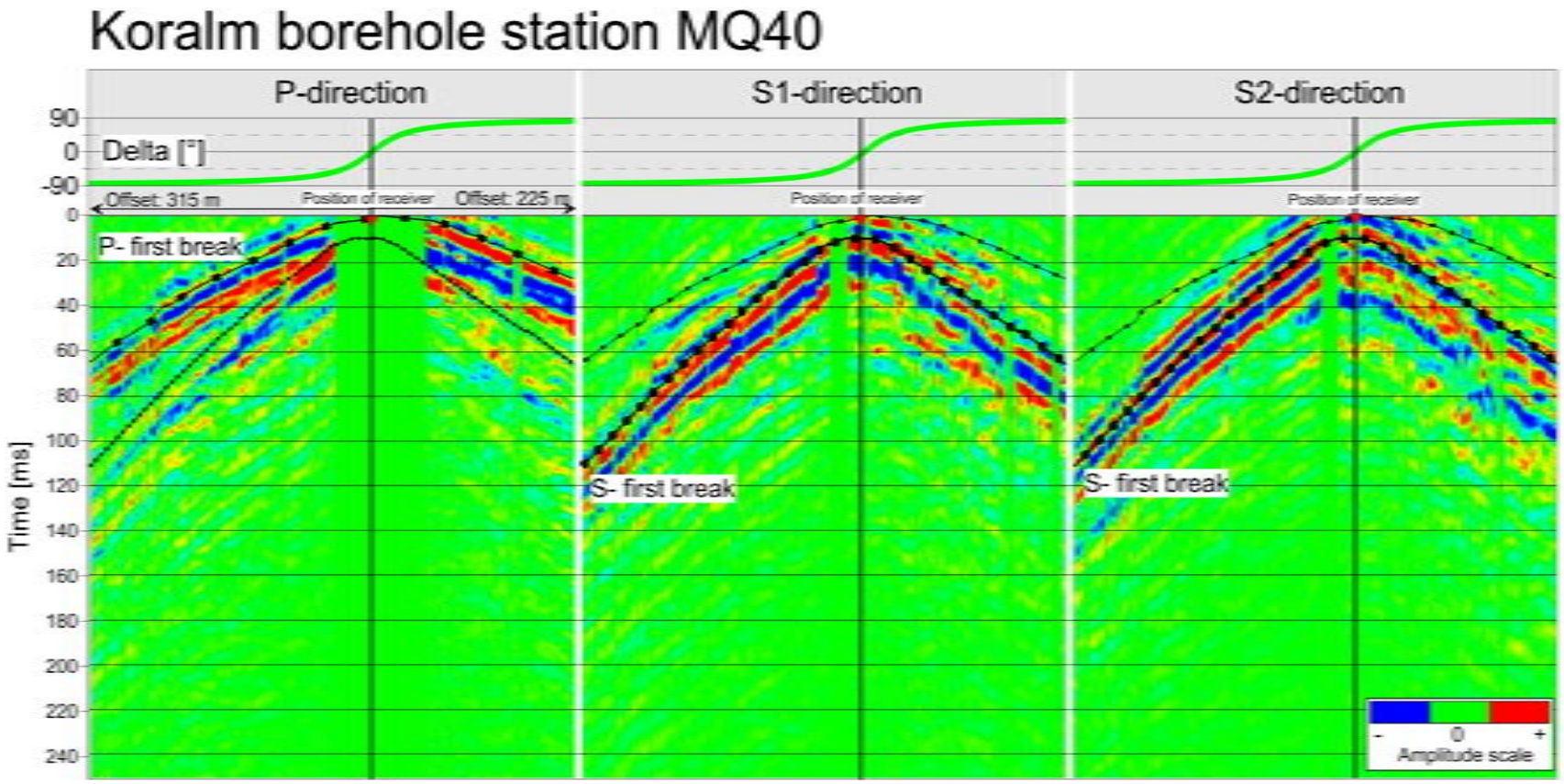

Figure 6.11.: Rotated seismograms of the 3C- borehole-geophone MQ40; above the seismograms the corresponding angle Delta is shown. The black lines indicate the p- and the s-wave first break picks.

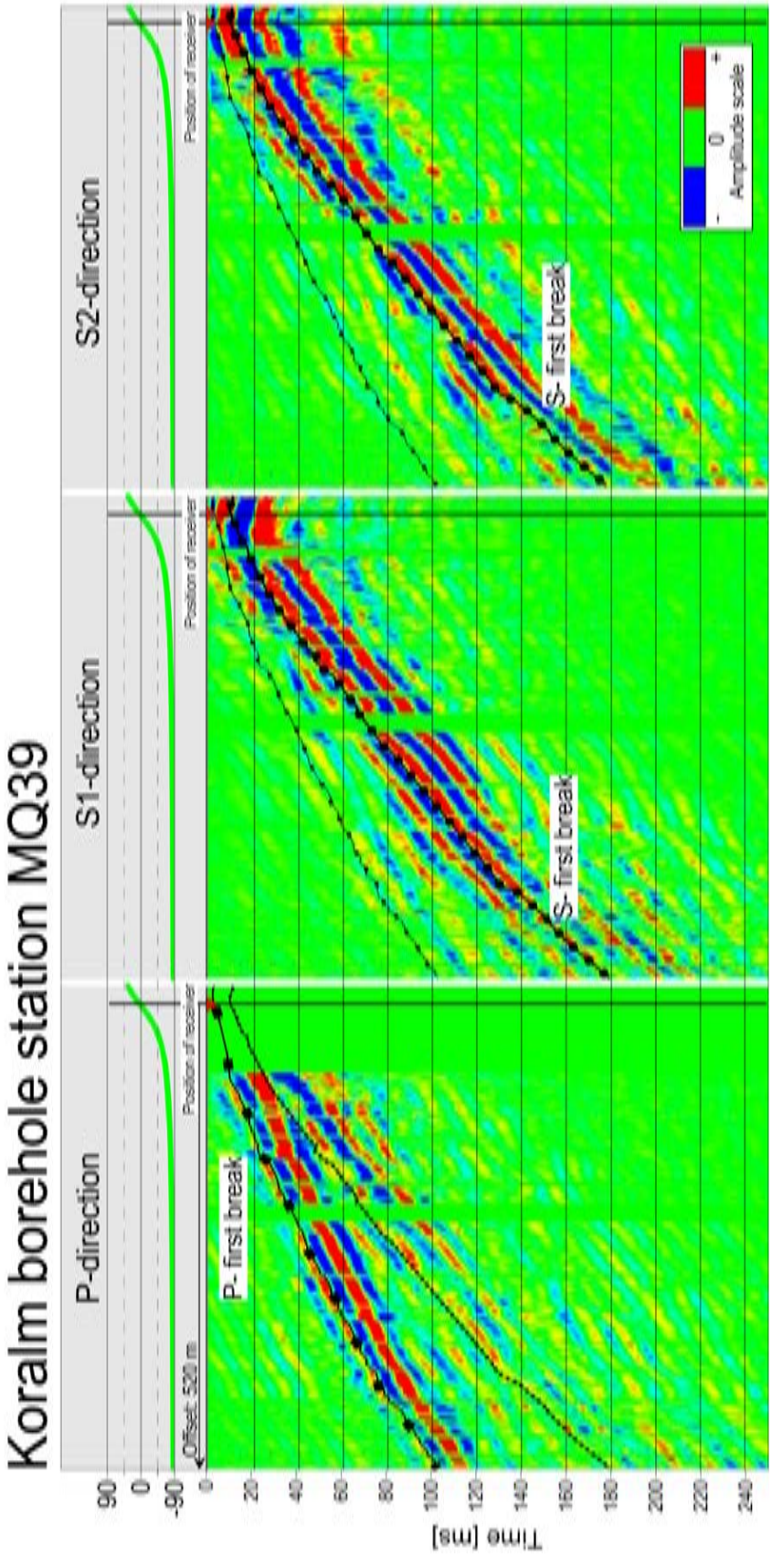

Figure 6.12.: Rotated seismograms of the 3C- borehole-geophone MQ39; above the seismograms the corresponding angle Delta is shown. The black lines indicate the p- and the s-wave first break picks.

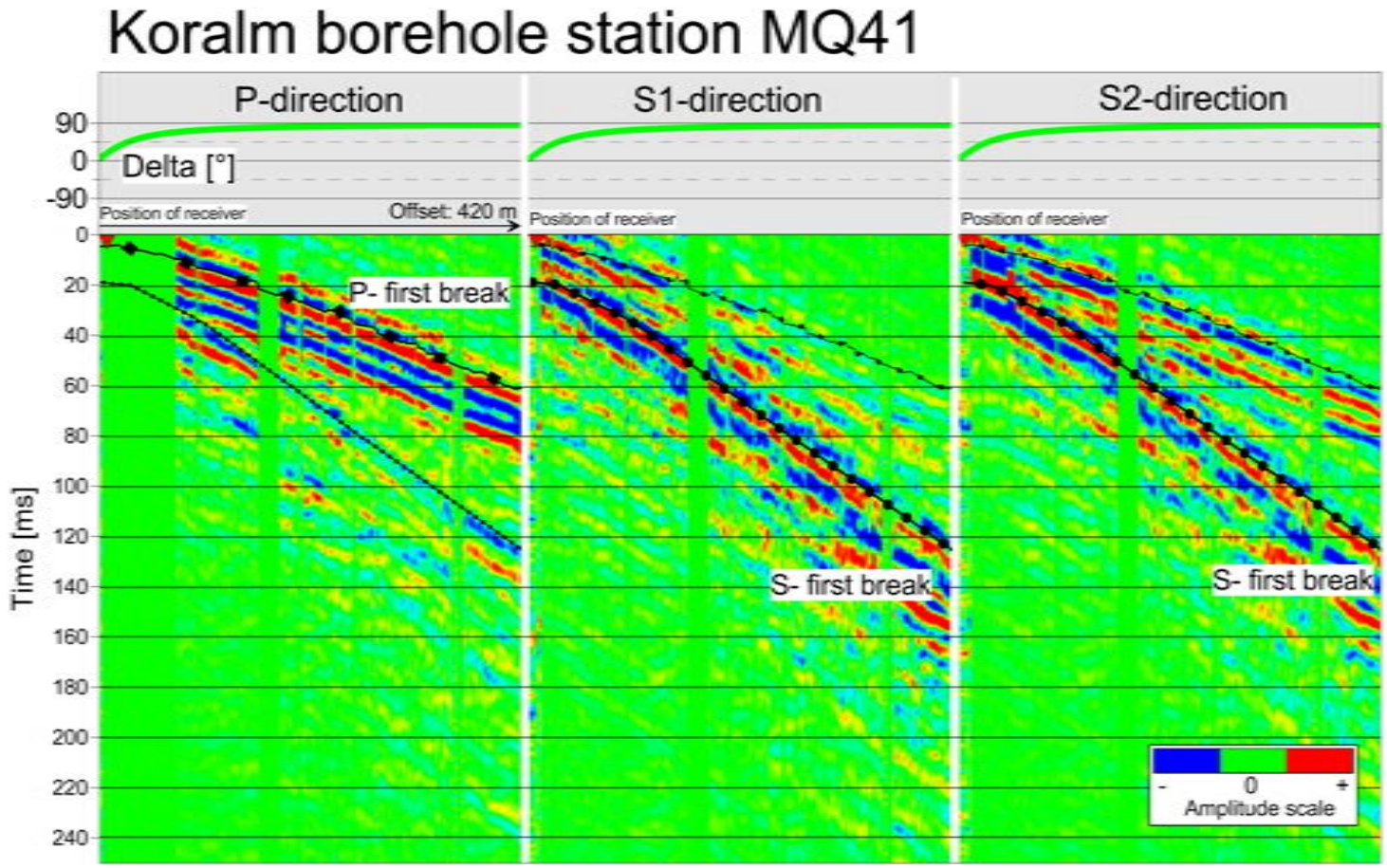

Figure 6.13.: Rotated seismograms of the 3C- borehole-geophone MQ41; above the seismograms the corresponding angle Delta is shown. The black lines indicate the p- and the s-wave first break picks.

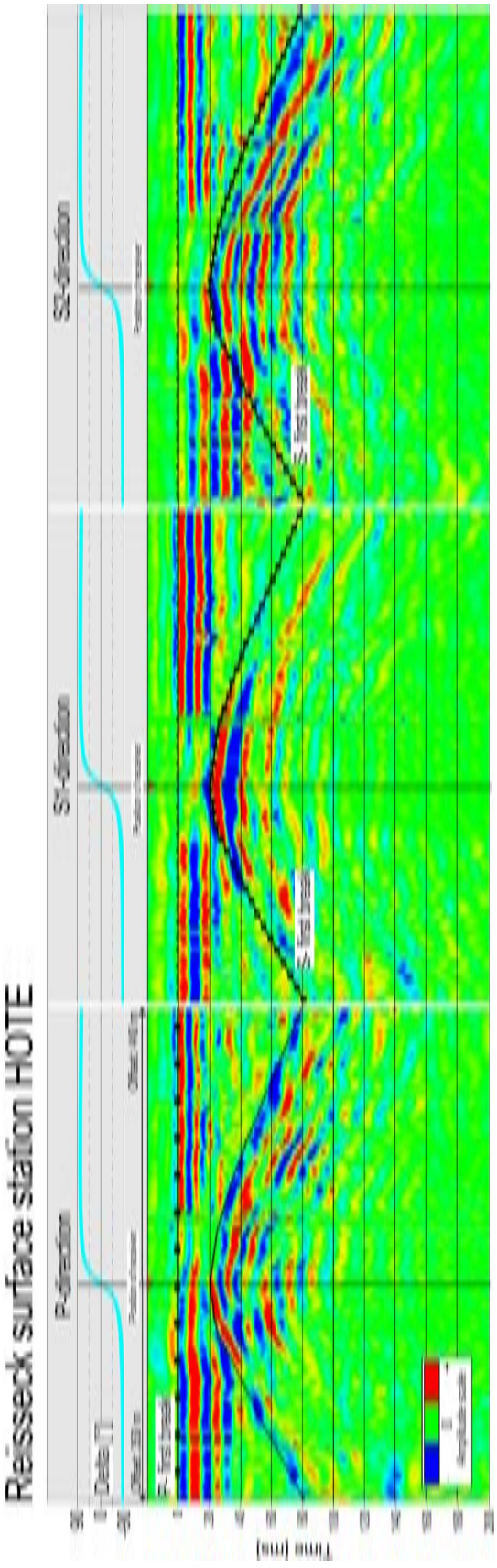

Figure 6.14.: Rotated seismograms of the 3C- surface-geophone HOTE; above the seismograms the corresponding angle Delta is shown. Data is aligned to p-wave, the black lines indicate the p- and the s-wave first break picks.

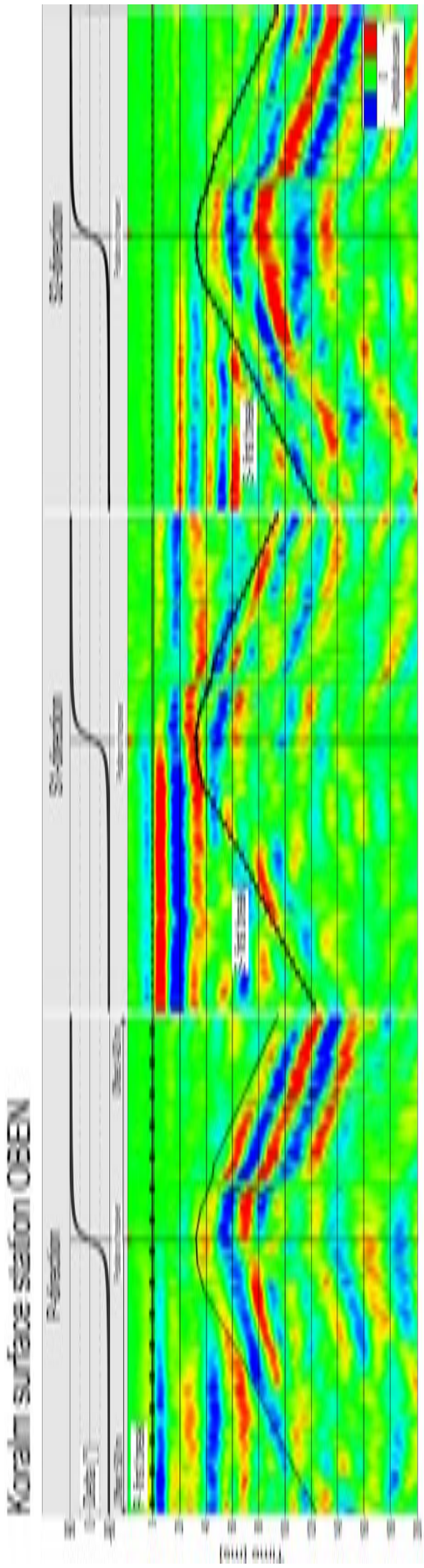

Figure 6.16.: Rotated seismograms of the 3C- surface-geophone OBEN; above the seismograms the corresponding angle Delta is shown. Data is aligned to p-wave, the black lines indicate the p- and the s-wave first break picks.

6.5. Polarization

In the described rotated data the polarizations of the p- and s-wave are mentioned. In order to verify the description an objective determination was introduced. By correlation with a common wavelet out of the data set, which has a clear positive polarization, the sign of the p- and s- wavelet can be read out of the correlated traces. The amplitude value gives information about how distinct the determination of the polarity is.

This common wavelet was generated by stacking the p-wavelet of 40-50 traces of the forward radiated section and reversed traces of the backward section. The wavelets have a length of 25-30 ms. For the receiver MQ39 and OBEN, only the backward section was available. Then the rotated traces were correlated with the common wavelet. Two examples of MQ40 and the surface position HOTE are presented in Figure 6.17. It shows the results after correlation including the picked first breaks. The results of the other receiver stations are shown in Appendix D.

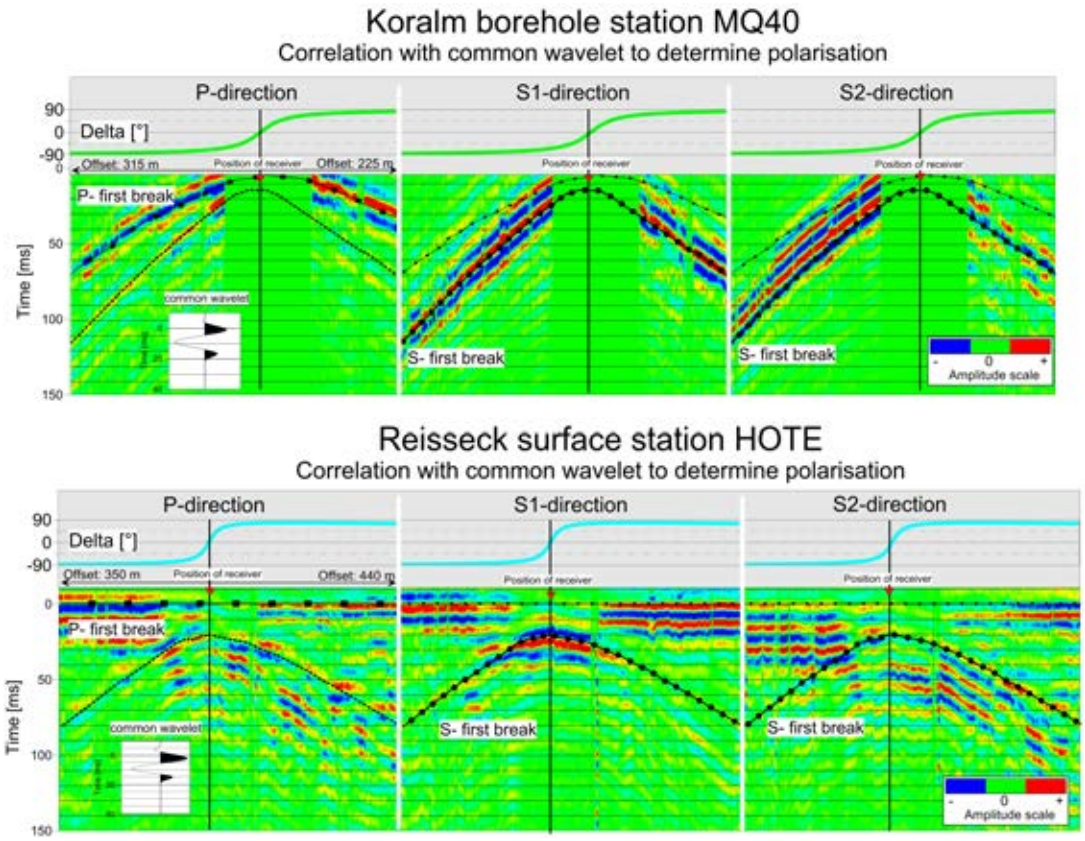

Figure 6.17.: Two examples are shown of MQ40 and HOTE, where the data is correlated with a common wavelet (shown in the white box left). The first breaks of p- and s-wave are given by the black lines; above the seismograms the angle Delta is plotted.

The maximum amplitude of the correlated traces were determined for the p-wave

and the two s-wave directions around the first break picks (+/- 10 ms) and then scaled to the maximum. Values lower than 0.05 were deleted. Figure 6.18 shows the correlation coefficient of the p-wave on the P-component and the s-wave on the S1 and S2 - component over Delta. The data was averaged for each degree. The determination for the borehole data is limited, as there is no separation of p- and s-waves wavelets within near offsets. This section corresponds to -40° until +40° Delta.

The p-wave polarization is clear negative for Delta smaller than 0° and positive for Delta larger than 0°. The absolute correlation factor decrease towards Delta 0°. This correlates with the smaller amplitudes in this section. The highest values are near +/- 90° Delta. The polarization of the S1-wave is positive all over the measured sections. In contrast to the p-wave the highest correlation values are around Delta 0°, and decreases towards +/-90°. In general the determination of S2-polarization was more difficult than on the S1-direction. Therefore the data amount is the smallest. Best results gave the borehole stations in the tunnel, whereas in the data of the surface station OBEN at Koralm the polarization could not be identified. The results of the borehole stations reveal a positive polarization in the S2-direction over the whole measured section, the same is seen in the data at Bärenwerk (CUBE). The resulting polarities at Reisseck (HOTE) jump between positive and negative polarization.

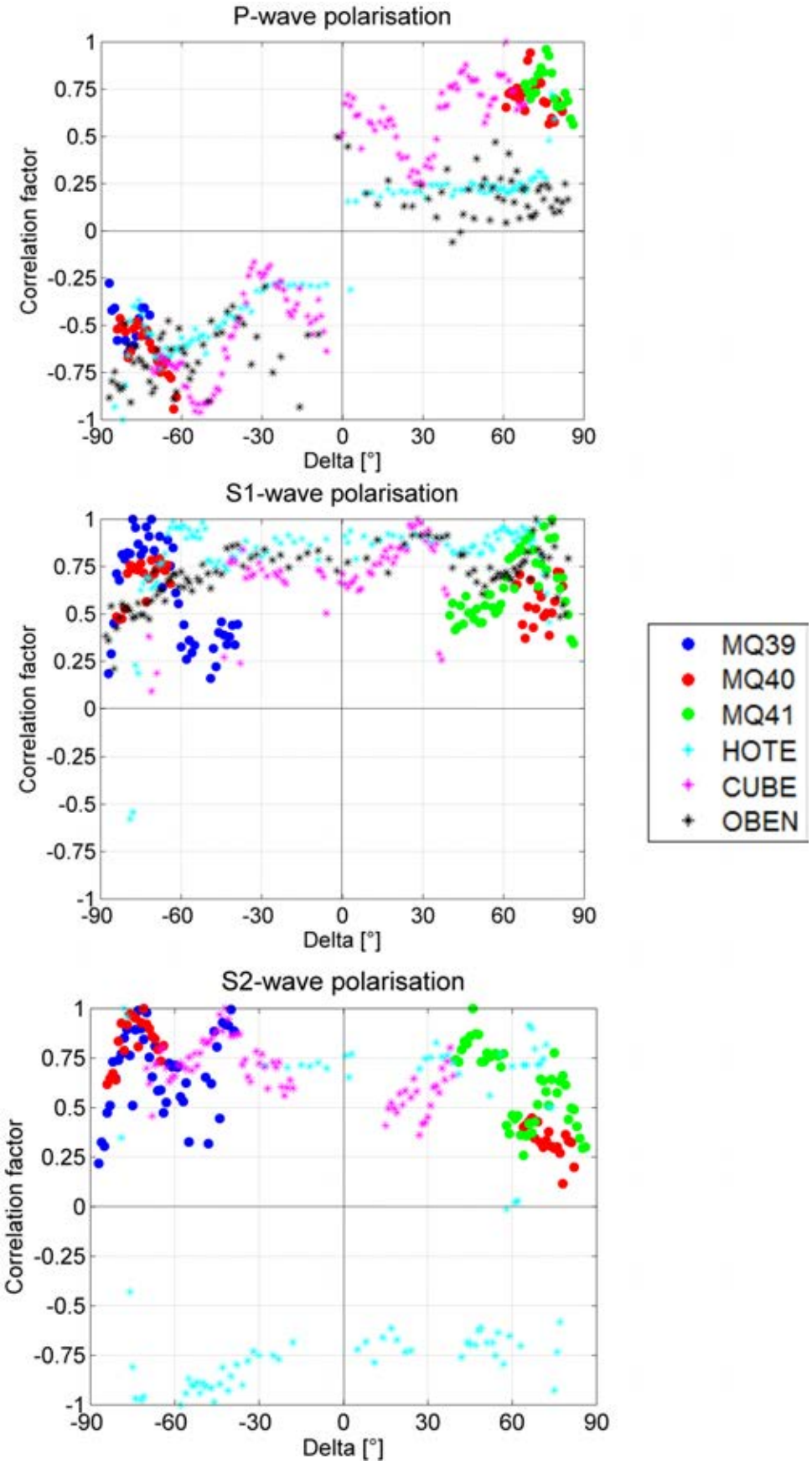

Figure 6.18.: Correlation factor of p-wave and the two s-wave directions are shown over Delta. The values are scaled to the maximum of each data set and averaged for each degree of Delta.

6.6. Amplitude Ratio P-wave to S-wave (P/S ratio)

After rotating the data into the P-S1-S2 direction and first break picking, the root-mean-square amplitude for the p-wave (Ap) and the s-wave (As) along the interpolated first breaks were determined on each component and summed up.

The total amplitude values for the p- and s-waves at each tunnel chainage are:

$$Ap = \sqrt{Ap(P)^2 + Ap(S1)^2 + Ap(S2)^2}; \qquad As = \sqrt{As(P)^2 + As(S1)^2 + As(S2)^2} \tag{6.3}$$

Before calculating the P/S ratio noisy amplitude data was eliminated. The standard deviation of the amplitudes within a given bin size of the offset was calculated along the y-axis. All data points within the bin size, which difference to the mean was greater than 2 times the standard deviation, were deleted (see Figure 6.19). This filtering method was also successfully applied by e.g. Flores Orozco et al. (2012).

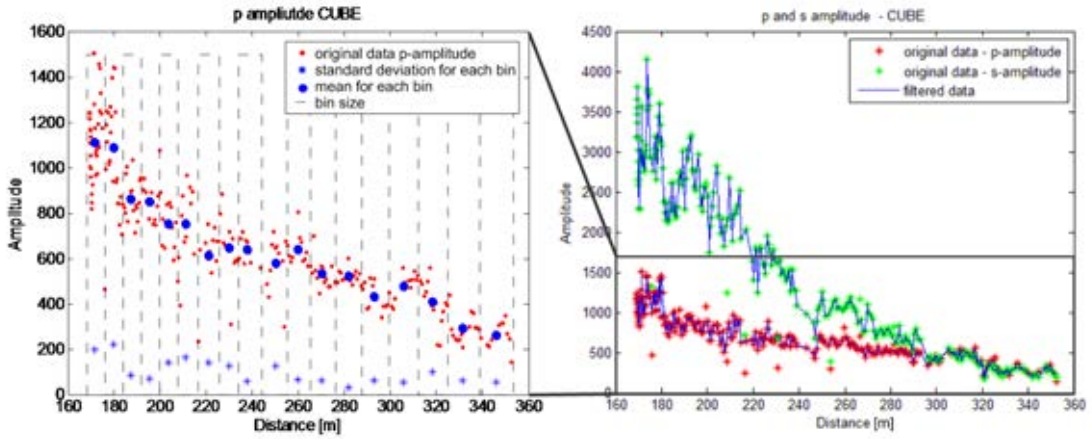

Figure 6.19.: Left:Data for p-amplitude of receiver CUBE and calculated mean and standard deviation for each bin size along the offset. Right: comparison of original data points with filtered data points for p-and s-wave amplitudes.

One important factor for the amplitude is the decrease with larger offsets (geometrical spreading). Elastic waves disperse in a medium and as the energy stays the same, the amplitudes are smaller as the wavefront is larger at greater distances to the source. The amplitude attenuation of body waves due to this geometrical spreading is according to the elastic wave theory r^{-1} in the far-field, which is valid for our data. On the other hand the amplitudes depend also on the damping factor (Q), which corresponds to the energy lost in each cycle because of imperfections in the elasticity of the material (intrinsic damping). Due to both factors the s-wave is more attenuated than the p-wave.

The recorded amplitude at a certain distance A(r) for a wave can be determined after Aki and Richards (2002) as followed:

$$A(r) = \frac{A_0 * e^{-\frac{\omega_0 * r}{2 * c * Q}}}{r} \tag{6.4}$$

A_0 ... amplitude at source point
r .... distance to source
ω_0 .... source frequency of wave
c .... velocity of wave ($v_p : p - wavevelocity$ or v_s: s-wave velocity)
Q .... damping factor (Q_p for p-wave or Q_s for s-wave)

The factor 1/r represents the amplitude decay due to geometrical spreading. The factor $e^{-\frac{\omega_0 * r}{2 * c * Q}}$ corresponds to the intrinsic damping.

By computing the ratio of p-wave amplitude to s-wave amplitude (P/S ratio) for each tunnel chainage the geometrical spreading and a possible different source amplitude A_0 is immediately reduced. So within the scope of this thesis only the ratios are analyzed.

The relative distances within one degree Delta between -90° to -75° and 75° to 90° Delta ranges from 15 m to 149 m (left plot in Figure 6.20). So within one degree the P/S ratio varies also due to the different attenuation. To reduce this, a mean attenuation curve over the distance (r) with an exponent (n) in r^n was determined for all receiver stations. The fitting of the P/S ratio was made separately for backward and forward radiation directions. The exponent ranged between -0.2 and 1.79. Then a median value for the P/S ratio exponent was calculated with n=1.28, as in general the ratio increases with larger distances. The ratios for each Delta within -90° to -75°and 75° to 90° were corrected with the median exponential function and scaled to a reference distance (shortest offset) according to the following equation:

$$P/S(r)_{corr} = P/S(r) * r^{1.28} * r_{ref}^{1.28} \tag{6.5}$$

So the influence of the different amplitude decay of the p- and s-wave is reduced. The comparison of the original ratios to the corrected ones show that the values were only slightly decreased (right plot in Figure 6.20).

For cylindrically symmetrical mechanism, such as single force or tensile fracture, the radiation pattern varies only over the angle Delta, it is equal for all Epsilons. A detailed description of the radiation pattern is given in the following Chapter 7 - Analysis of source mechanism. As only cylindrically symmetrical mechanism are considered the results are compared in regard to the angle Delta.

Figure 6.21 shows the P/S ratio over Delta for the three borehole receivers at Koralm

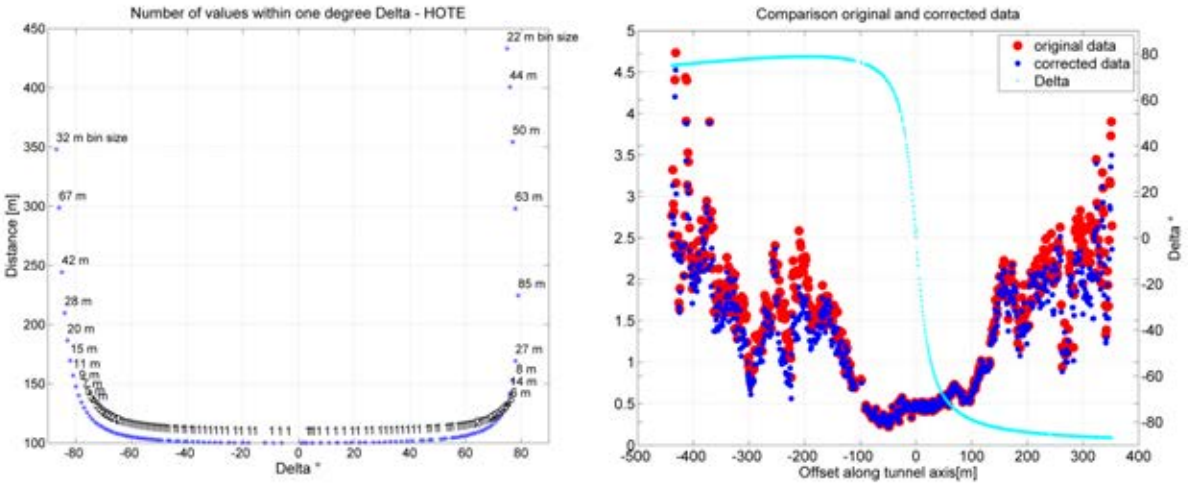

Figure 6.20.: left: distance in meter for one degree of Delta; example Reisseck HOTE; right: original and corrected P/S amplitude ratios and angle Delta plotted against offset; zero offset means that the TBM was just above the receiver station.

and the three surface receivers. All data have an increase towards -90° and +90° Delta. The increase in the forward wave field (positive Delta) starts earlier (around 60°), and the backwards increase is later (around -80°), despite the data of receiver at Bärenwerk. Within -50° and +50° only data of the surface station are available. Specially around Delta 0° least data is available simply due to the geometry of receiver and tunnel axis. The ratio in this section is nearly constant around 0.5. It has to be noted, that for the surface station the influence of the free surface on the amplitudes was not considered.

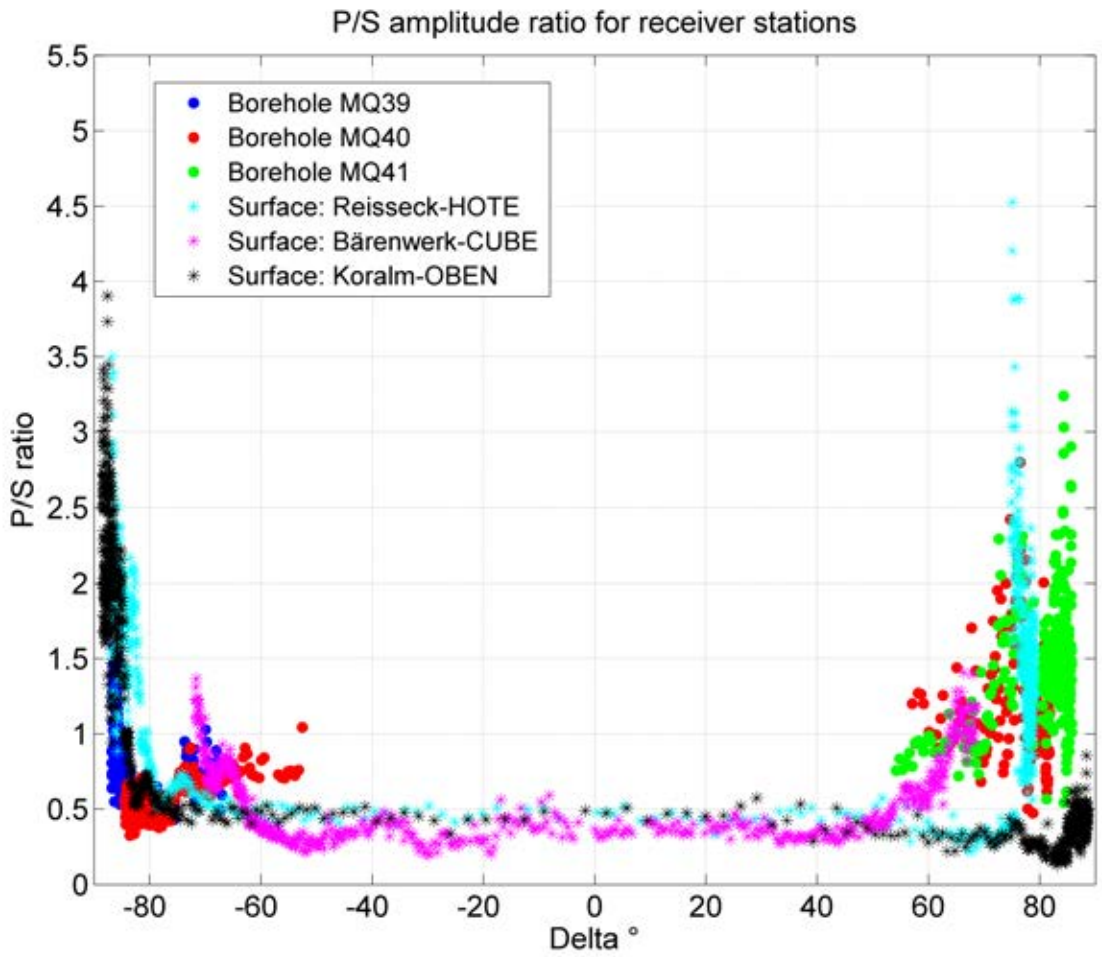

Figure 6.21.: The calculated P/S amplitude ratios are plotted against Delta. The different receivers have different colors. Towards -90 and 90 ° there is an increase in the ratio in all data sets. The increase is in the forward direction (positive Deltas) earlier than on the backward direction. Between -50° and +50° only data of the surface station is available. Here the ratio is around 0.5.

7. Analysis of source mechanism

The spatial distribution of the radiated seismic waves are distinctive for seismic source mechanism. By analyzing the radiation pattern of seismic waves generated by the cutting process, the possible source mechanism can be estimated. On the one hand, the spatial distribution and amplitude values of p- and s-waves are characteristic, on the other hand, the polarization of the radiated waves gives information about the source.

In the following chapter the results of the field data, their polarization and P/S amplitude ratio are compared with the characteristic radiation pattern of a single force. Further, the tensile fracture is considered as an additional source. The combination of both models are shown and related to the recorded data.

7.1. Description of the radiation pattern by single force

It was stated in the hypotheses for TSWD (see Introduction and (Brückl et al., 2008)) that the TBM can be regarded as a single force. During the cutting process the cutters are pressed hard against the rock face and most of the energy (directed normal to the tunnel face) is consumed to form the crushed zone. This is already described in detail in the Chapter 5 - Cutting process - the main seismic source.

Through the rumbling of the discs over the tunnel face, high frequent, abrupt, irregular and discontinuous forces (Entacher et al., 2015) are applied on the rock. This change in energy loading and unloading leads to a sudden break out of the material (kerf forming) and an elastic acceleration of the rock and the cutters.

Seismic source mechanism are described e.g. in Aki and Richards (2002). The formulas to calculate the different radiation pattern are all out of this book. In general they have a term concerning the amplitude, one term for the distance, one for the spatial direction and finally one for the source mechanism. In case of a single force the source mechanism can be described by a force applied in a certain direction.

Equations 7.2 and 7.2 are the equations after Aki and Richards (2002) for the far-field displacement at a sphere with radius one, due to a single force (F) in positive x-direction. It is valid within an infinite homogeneous isotropic medium, characterized by the density (ρ) and the seismic velocities (v_p and v_s) of the p- and s-wave. The ith vector component of the p- and s-wave displacement (u), is written

$$\text{P-wave: } u_i^P(\gamma) = \frac{1}{4\pi\rho v_p^2}\,\frac{1}{r}\,[\gamma_i\gamma_j]\,F_j \tag{7.1}$$

$$\text{S-wave: } u_i^S(\gamma) = \frac{1}{4\pi\rho v_s^2}\,\frac{1}{r}\,[(\delta_{ij}-\gamma_i\gamma_j)]\,F_j \tag{7.2}$$

defined by the direction cosines of the propagation vector γ, whereby the summation convention for repeated indices is used (γ_i,γ_j) and δ_{ij} is the Kronecker delta.

A single force radiates positive polarized p-waves in the direction of the applied force (+x-axis), negative polarized p-waves against the force direction (-x-axis) and no p-wave perpendicular to this axis. The s-wave has its maximum perpendicular to the x-axis and is zero in x-direction. The maximum amplitude of the s-wave is 3 times larger than the maximum of the p-wave for $\frac{v_p}{v_s} = \sqrt{3}$. For a comparison with the field data the x-axis corresponds to the tunnel axis, with the TBM in the source point, and the advance direction in positive x-direction.

Figure 7.1 shows the radiation pattern of a single force in x-direction [F= (1,0,0)] according to equations 7.2 and 7.2 for the p-wave and the s-wave on a sphere, calculated with values for density ρ = 2700 kg/m^3, v_p = 5000 m/s and v_s =2886 m/s (=$\frac{v_p}{\sqrt{3}}$).

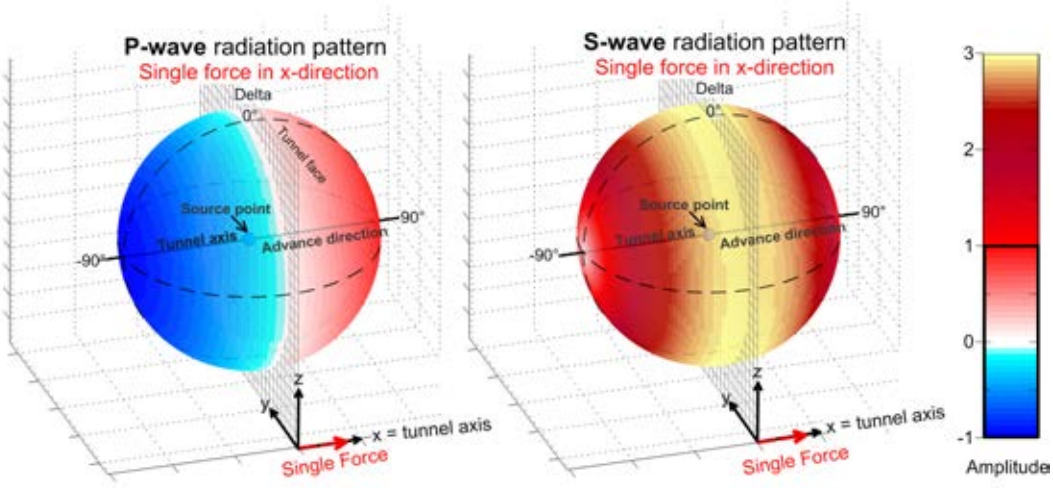

Figure 7.1.: The radiation pattern of the p-wave and s-wave are shown for a single force, applied in x-direction. The amplitudes are scaled to the maximum p-wave value. The gray line indicates the tunnel axis, with a TBM at the source point.

In Figure 7.2 the absolute p-wave and s-wave amplitude and the P/S ratio of the absolute values for a single force over Delta are plotted. Most of the p-wave is radiated within angles of 70° and 90° Delta in the forward direction and -70° until -90° Delta

in backward direction. The maximums are at +/-90°. The s-wave is very low in these sections, it's maximum is at Delta 0°. The P/S ratio for a single force (black dotted line) is symmetrical for positive and negative Deltas. The ratio value 1 is at +/-75° Delta and followed by a very steep increase towards +/-90° Delta. At Delta 0° the ratio is zero.

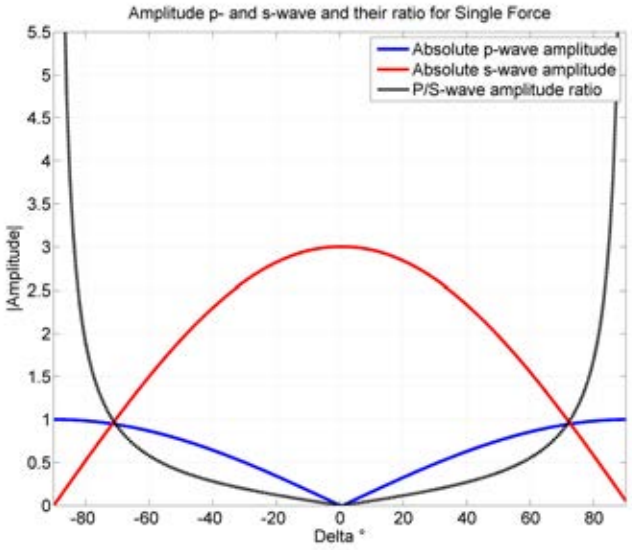

Figure 7.2.: The blue line corresponds to the absolute amplitude value of the p-wave, the red line to the s-wave. The P/S ratio is shown in the dotted black line. All values are scaled by the maximum p-wave amplitude of the single force.

Comparison of results and single force model

If the TBM can be characterized as a single force, the polarization of the p-wave has to change from negative to positive, when the TBM passes a fixed receiver. Most of the p-wave amplitude is radiated parallel to the tunnel axis, perpendicular to the axis no p-wave occur. The s-wave has its radiated maximum perpendicular to the tunnel axis and polarization does not change.

The described polarization of the waves in Chapter 6.5 can be explained by the single force model. The data also shows maximum p-wave amplitudes for large positive Delta (forward section) and negative Delta (backward section) and large s-wave amplitudes, when the TBM passes the position. A detailed plot of the P/S ratio of the field data and the model of single force is illustrated in Figure 7.3. The comparison shows that the model of single force can be used as a first order approximation, mainly in axial direction. The increase of the P/S ratio in the data corresponds to the model within a

certain deviation.

The backward ratios lie always under the model values for large negative Deltas. In the forward section the data is around the modeled values. Within -50° and +50° Delta the model does not fit, the ratio is much higher (around 0.5) than the modeled values. In this case a higher ratio means, that more p-waves are radiated perpendicular to the tunnel axis, which cannot be explained by the single force model.

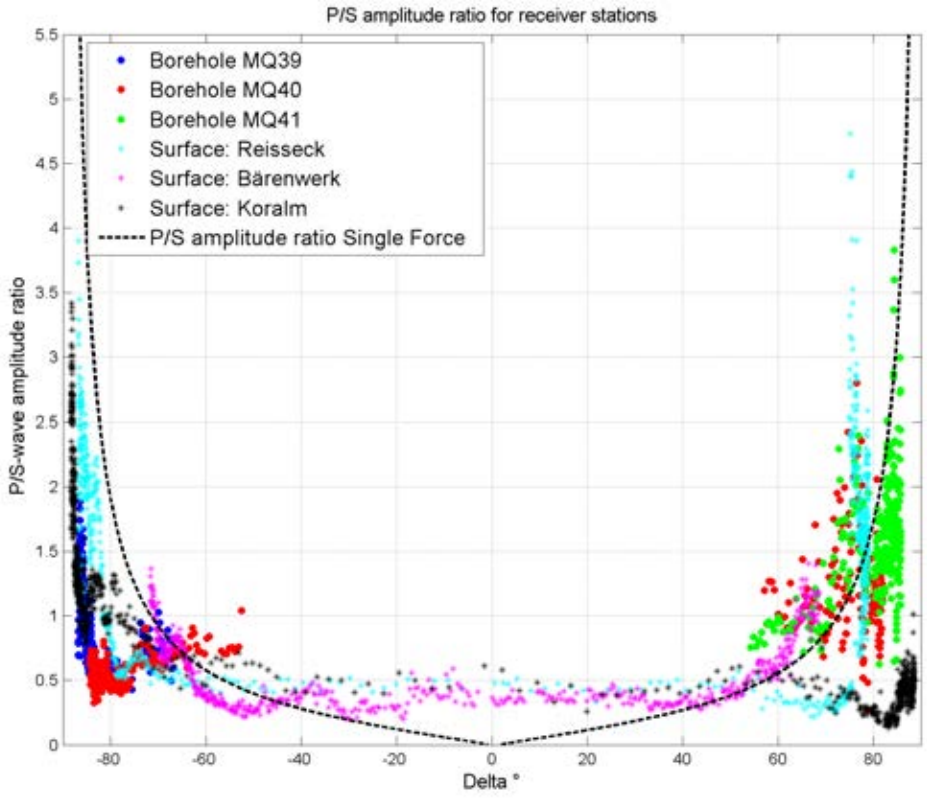

Figure 7.3.: The calculated P/S amplitude ratios are plotted against Delta. The different receivers have different colors. The modeled P/S ratio for a single force is shown in the black dotted line.

7.1.1. Measured and calculated displacements

There is still the uncertainty of the physical meaning of the recorded pilot signal (the measured accelerations) and how good it represents the seismic source.

Within this work it was stated that the recorded accelerations results due to the cutting process. As the rock breaks, the cutters are accelerated axial into the kerfs and gain also a deeper penetration. The maximum accelerations are limited to the rigidity (uniaxial compressive strength) of the material. These accelerations are transmitted

to the pilot sensor location and registered there. Under the consideration that the source mechanism is a single force and the pilot sensor records the generated vibrations properly, the applied force (F) can be determined as the product of the measured accelerations (a) on the pilot signal and the mass (m) of the rotating TBM head. This force applied to the tunnel face is the source for the measured displacement (u) at the receiver cross-sections behind the TBM. If we know the force at the source, the displacement in a distance (r) to the source can be calculated according to Equation (7.2).

As the axial component of the borehole receivers contains most of the p-wave, its displacements can be compared with the calculated displacements. If the values are in the same range, it can be concluded, that the pilot sensor corresponds the applied force. It has to be mentioned that the actual recording positions lead certainly to weaker signals and it is assumed, that the force is applied at one point.

To calculate the maximum displacement the cosines product $\gamma_i\gamma_j$ in Equation (7.2) is set to one, the values estimated for v_p =5000 m/s and ρ =2700 kg/m^3 and the force (F) replaced with the product of the mass (m) of the TBM cutterhead and the measured accelerations (a) of the axial pilot sensor:

$$F = m\ a \tag{7.3}$$

The mass of the different TBM heads were provided by the clients. The measured accelerations have a mean between 4 to 10 m/s^2, with peaks until 50 m/s^2.

The calculated displacement is compared to the measured displacement at certain cross-sections at the tunnel of Koralm and Reisseck. The mean of the envelope of the accelerations and displacements were used for the calculation.

The following table 7.1 lists some examples:

Table 7.1.: Displacements at cross-sections

Distance	**Displacement calculated**	**Displacement measured**
	Koralm; mass of TBM= 220 tons	
200 m	6.9*10-9 m	3.6*10-9 m
	Reisseck; mass of TBM= 80 tons	
250 m	2.7*10-9 m	2.3*10-9 m
478 m	1.7*10-9 m	1.1*10-9 m

In the other direction we used the measured displacement (u) at a cross-section and the measured acceleration (a) to calculate the necessary mass of the TBM cutterhead.

The calculated displacements and the measured values are in the same range. The calculated cutterhead mass of data at Reisseck is around 55 t, and Koralm around 115 t.

These values are smaller than the actual weight, as the comparison of the displacement also showed, that the measured values are always smaller than the calculated ones, but in the range of realistic values.

This confirms, that the accelerations on the pilot sensor times mass represents adequately the single force, as source for the displacements.

7.2. Additional effect of tensile fractures

As stated before, the P/S ratio of the single force does not fully explain the recorded data. A further source mechanism must be added, which radiates p-waves perpendicular to the tunnel axis. Amplitudes of other possible forces, acting in radial and vertical all over the tunnel face would extinguish each other. This is also valid for shear fractures. However, the p-wave amplitudes of the tensile fractures are summed up in every direction, as this mechanism radiates positive polarized p-waves in all directions perpendicular to the crack plane (see Figure 7.5).

Beside the forming of kerfs and crushing the rock, cracks are formed in various direction. After the proposed cutting model in Figure 5.1 median cracks occur in axial direction, which open in the vertical directions. This opening can be described as a tensile fracture. Dependent on the material different major directions of such cracks are dominant. Finally cracks grow also parallel to the tunnel face, in z-direction. Cracks within two cutters coalesce and form a chip. These cracks are also regarded to be tensile fractured.

Various model combinations of single force and tensile fractures in different directions are presented in this chapter. All models explain the increase of the ratio towards +/-90° Delt and have a zero point the change of polarization between -45° and 0° Delta.

Source mechanisms of fractures are expressed by body forces equivalents (Aki and Richards, 2002), which are described by so called moment tensor (M). There exist three modes of failure:

- Mode I - tensile failure
- Mode II and III - shear failure

The tensile failure mode I is equivalent to a superposition of three vector dipoles on the main axes x-y-z (Figure 7.4). The corresponding moment tensor (M) for a tensile

fracture in the x-y plane and opening in z-direction in a solid rock is:

$$\mathbf{M} = \begin{pmatrix} 1 & 0 & 0 \\ 0 & 1 & 0 \\ 0 & 0 & (\lambda + 2\mu)/\lambda, \end{pmatrix} \tag{7.4}$$

where λ and μ are Lamé parameters.
The tensile radiation pattern was computed using this expression with $\lambda = \mu$. Then the moment tensor (M) of a pure tensile source can be rewritten to:

$$\mathbf{M} = \begin{pmatrix} 1 & 0 & 0 \\ 0 & 1 & 0 \\ 0 & 0 & 3 \end{pmatrix} \tag{7.5}$$

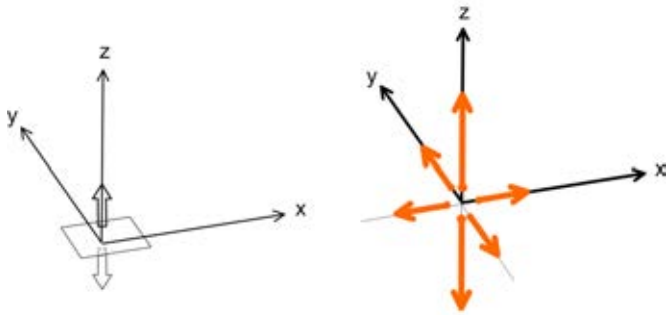

Figure 7.4.: The body-force equivalent for a tension fracture in an isotropic medium.

The displacement (u) due to a tensile fracture in the far-field at a distance 1 is given by equation 7.7 and 7.7 modified after Aki and Richards (2002). This equation is valid within an infinite homogeneous isotropic medium, characterized by the density ρ and the seismic velocities v_p and v_s of the p- and s-wave, along the propagation vector, defined by the direction cosines γ_i γ_j γ_k, whereby the summation convention for repeated indices is used and δ_{ij} is the Kronecker delta.

$$\text{P-wave: } u_i^P(\gamma) = \frac{1}{4\pi\rho v_p^3} \frac{1}{r} \left[\gamma_i\gamma_j\gamma_k\right] M_{j,k} \tag{7.6}$$

$$\text{S-wave: } u_i^S(\gamma) = \frac{1}{4\pi\rho v_s^3} \frac{1}{r} \left[(\delta_{ij} - \gamma_i\gamma_j)\,\gamma_k\right] M_{j,k} \tag{7.7}$$

Figure 7.5 shows the radiation pattern on the focal sphere of a tensile fracture, which opens in z-direction. The p-wave amplitudes (see Figure 7.6) are never zero and the maximum is at 0° Delta, perpendicular to the tunnel axis. The s-wave has two maximums at +/-45° Delta and is only 2 times larger than the p-wave. The P/S

amplitude ratio at +/- 90° Delta is similar, whereas at 0° Delta there is a further maximum. The values are scaled to the maximum of the p-wave of a single force, in order to make it comparable. The smaller amplitudes regard to the single force can be explained by the amplitude factor $\frac{1}{v^3}$, in contrast to the single force with $\frac{1}{v^2}$.

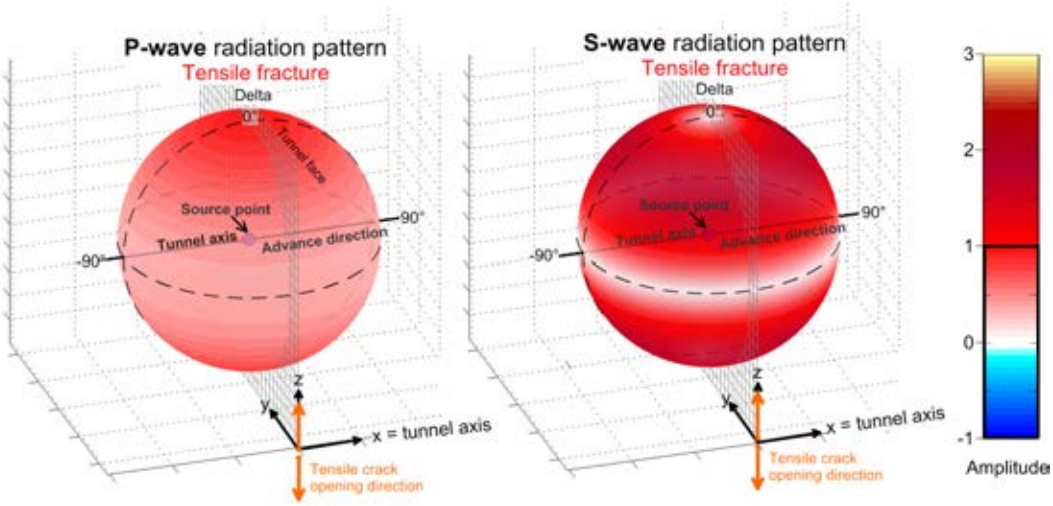

Figure 7.5.: The radiation pattern of the p-wave and s-wave are shown for a tensile fracture, opening in z-direction. The amplitudes are scaled to the maximum p-wave value. The gray line indicates the tunnel axis, with a TBM at the source point.

As the cracks develop in several directions (see Chapter 5 - Cutting process - the main seismic source), four models were analyzed, with different directions of tensile cracks:
(a) only axial crack occur, which opens in vertical direction = vertical opened tensile fracture
(b) only vertical crack occur, which opens in axial direction = axial opened tensile fracture
(c) combination of axial and vertical cracks occur, which open in vertical and axial direction = axial / tangential tensile fracture
(d) combination of two directions, which open in 45° and -45° in the tangential-axial direction = angled tensile fracture

Then the tension models were added to the single force model. Thereby different summation factors were used. The index (R) gives the ratio of single force to tensile fracture models. Index R=1:0 means, that only the amplitudes of single force are counted, for R=1:2, one time single force and 2 times the tensile fracture amplitudes are summed up. The index (T) represents the weighting of the two different directions of the tensile cracks.

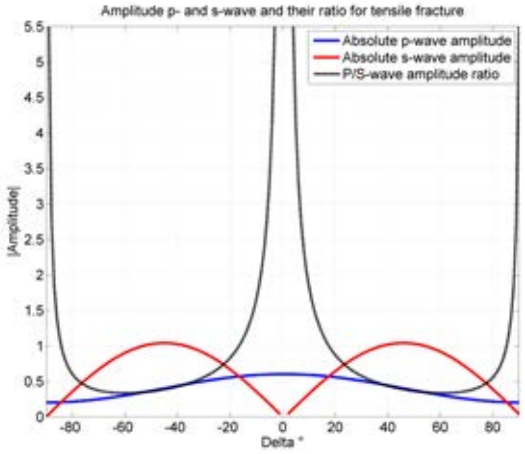

Figure 7.6.: The blue line corresponds to the absolute value of the p-wave, the red line to the s-wave. The P/S ratio is shown in the dotted black line. All values are scaled by the maximum p-wave amplitude of the single force.

In general the addition of tensile fractures increases the ratio around Delta 0°. The distinct increase in the negative Delta section is shifted to the left (smaller Delta values), the increase against +90° is only slightly shifted to the right (larger Delta values). In case a tensile fracture radiates positive p-waves in all directions, the polarization does not change at 0° Delta after summation. It is shifted towards the negative Delta.

Figure 7.7 presents the P/S ratios of various combinations of a single force and additional tensile fractures. In the upper left diagram additional tensile fracture model (a) with different summation index: R:1:0.5, 1 and 2. With factor 2 the high ratios around 0.5 can be explained very well in the positive Delta section, but the polarization of the p-wave changes at -45° Delta. With a weighting factor 0.5 this change in polarization is earlier around -18° but the ratio around Delta 0° is not so high.

In the upper right diagram in Figure 7.7 tensile fracture model (b) was added with different summation indexes: R:1:0.5, 1 and 2. The ratio could not be increased significantly and even with weighting factor 2 the polarities of the p-wave changes for the negative Delta section, which is never observed in the data.

Model (c) is presented in the lower left diagram of Figure 7.7, which is a combination of the first two ones with different weighting factor: 0.5 and 1, for the different directions (T), and 0.75, 1, 1.5 and 2 for the summation (R). The ratios are similar to the model (a), whereas the increase of the ratio around Delta 0° is not so large.

Model (d) is presented in the lower right diagram of Figure 7.7, which is a combination of two angled tensile fractures in +/-45° Delta with different weighting factor: 0.25, 0.5 and 1. The increase on both sides is flattened and only a slight increase around Delta 0° is visible.

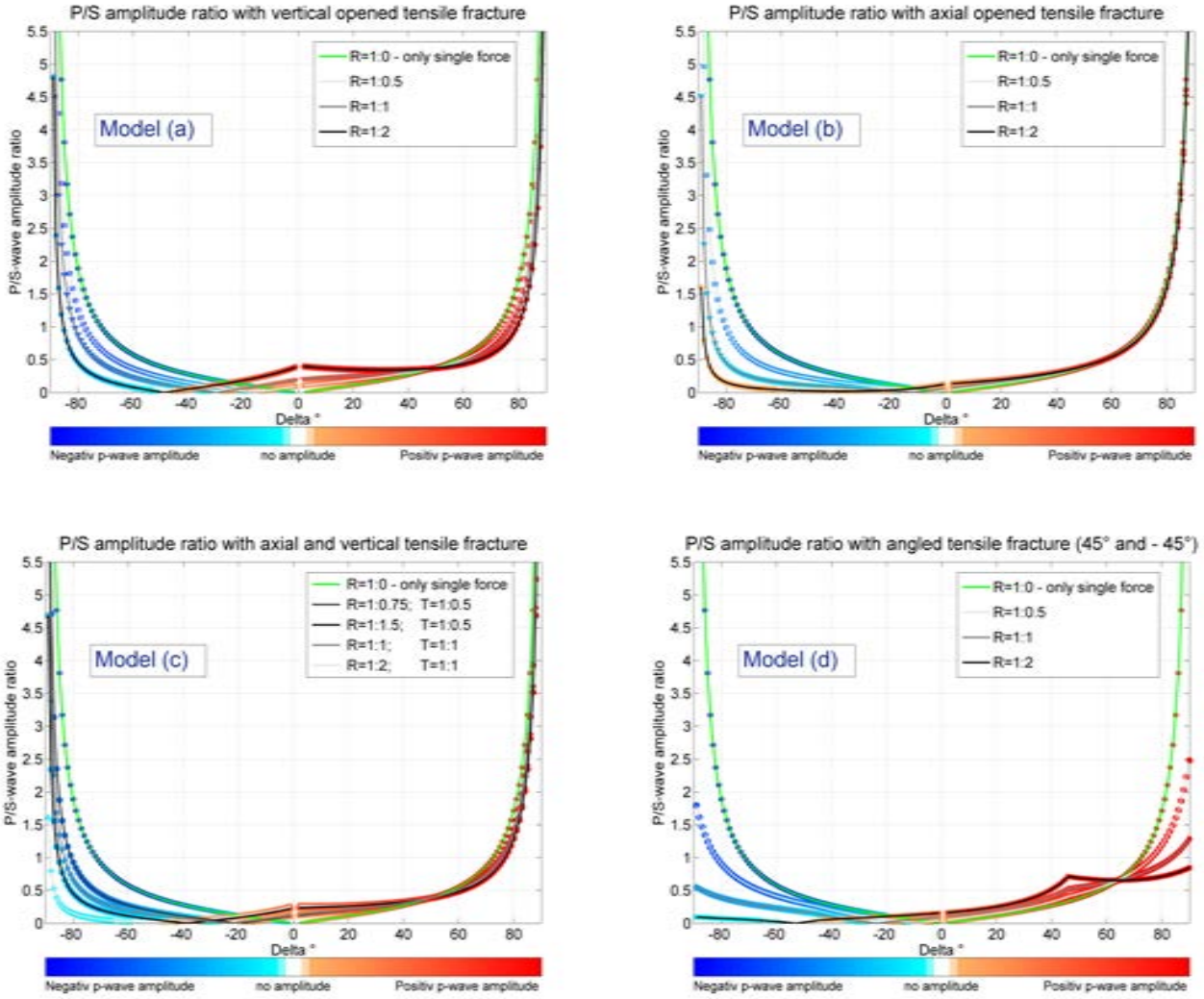

Figure 7.7.: Models (a), (b), (c) and (d) for different P/S amplitude ratios, which include tensile fracture; the lines are colored with the polarization of the p-wave, blue - negative; red - positive. The index R represents the weighting of single force: tensile fracture; the index T the weighting of the two different directions of the tensile fracture.

All models explain the increase of the data towards +/-90° Delta and have a zero point the change of polarization between -45° and 0° Delta. Two combinations out of model (a) and (c) are chosen, which offer the best explanation for the data (Figure 7.8).

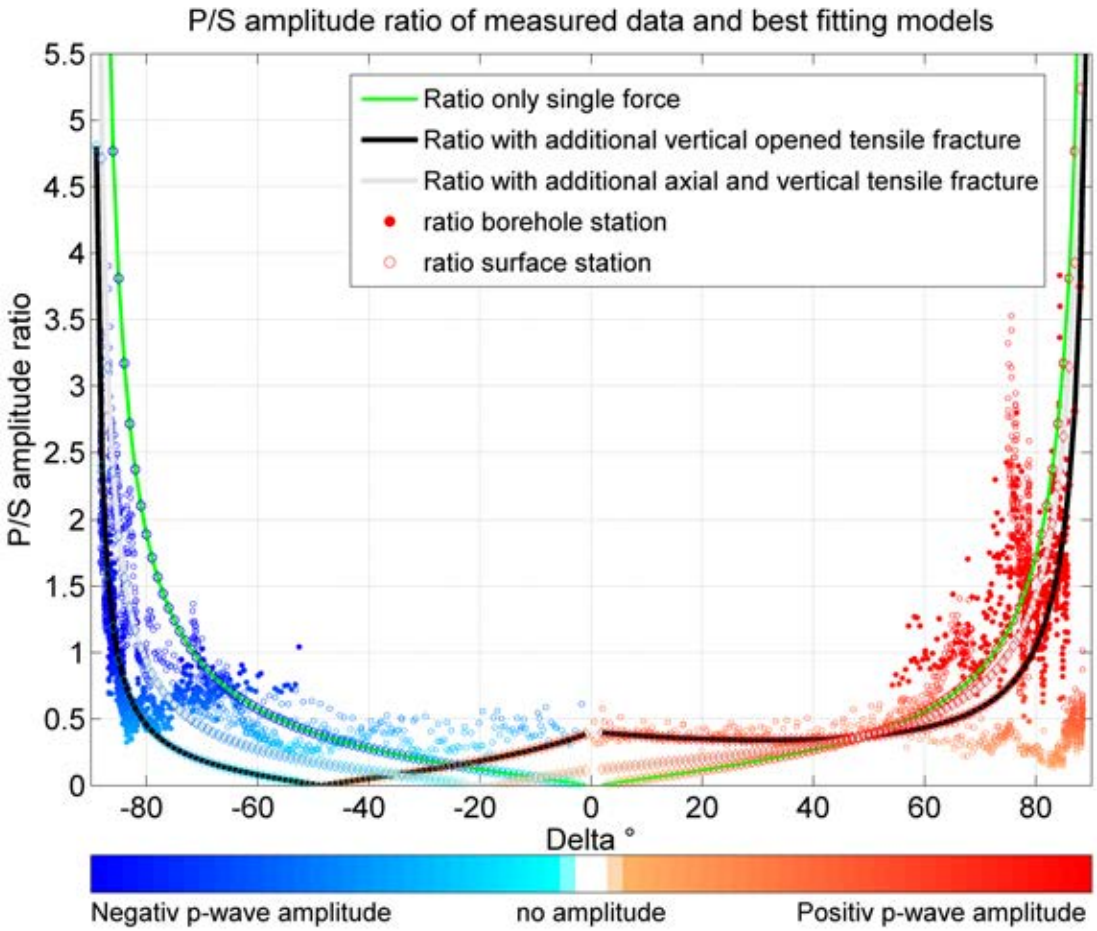

Figure 7.8.: P/S ratio of the borehole receivers and surface stations colored with p-wave polarization and the modeled ratios for single force (green line), single force with axial opened tensile crack (black line) and single force with axial and tangential crack (grey line).

The combination of an axial single force with additional axial crack, which opens in the vertical direction (model (a)=vertical opened tensile fracture) with R=1:2 would explain the data for the forward radiated wave field (positive Deltas), but the polarization of the p-wave is positive until -45° and the increase is shifted nearly to -90° in the negative Delta section, so that the measured values lie above.

The second chosen model is the combination of an axial single force and axial and

tangential cracks (model (c)=axial and vertical tensile fracture), which vertical opened fracture has 2 times larger amplitudes than the axial opened crack (T=1:0.5) and the summation with single force is R=1:0.75. The polarization change of the p-wave is at -20° but the ratio at smaller Deltas is not so high than in model (a). The ratio increase backwards is shifted towards -80°, which fits better the data than the single force model.

Figure 7.10 shows the spatial distribution of the P/S amplitude ratio on a focal sphere around the source point in a view from above and backwards. The measured values for the receivers stations (along lines) are plotted against the models for single force in axial direction (x-axis) and the combinations with the tensile fractures in axial direction and vertical direction (z-axis). The focus in this projection is the forward radiated wave field and the section around Delta 0°. The white zone in the model (P/S ratio = 0) is shifted to negative Deltas but the ratio increases within +/-50°. The ratio for single force is symmetrical in every direction. This symmetry is not given anymore in the combined models.

As a tensile fracture radiates positives p-waves in all directions, the polarization changes not at 0° Delta after summation with the single force model. It is shifted towards the negative Delta.

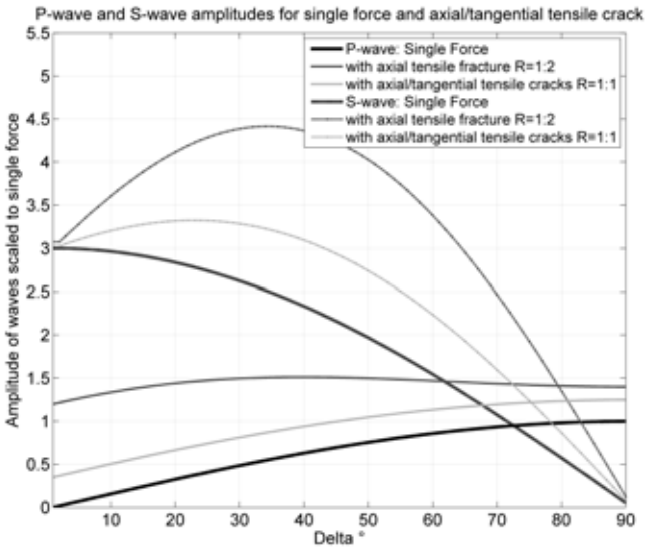

Figure 7.9.: Amplitudes of p-wave and s-wave for single force (black lines), with axial tensile crack (dark gray) and axial/tangential cracks (light gray) only for the forward radiated wave field (positive Deltas).

For TSWD the most interesting part is the forward radiated wave field, as these waves are reflected and interpreted after processing. Figure 7.9 shows the p-wave and s-wave amplitudes for the single force with additional tensile axial cracks and

tensile axial/tangential cracks. From Delta 75° to 90° the p-wave amplitude is only slightly increased. Within 85-90° the p-wave is always larger than the s-wave amplitude. For smaller Deltas the s-wave is dominant, especially for the model with axial tensile fracture.

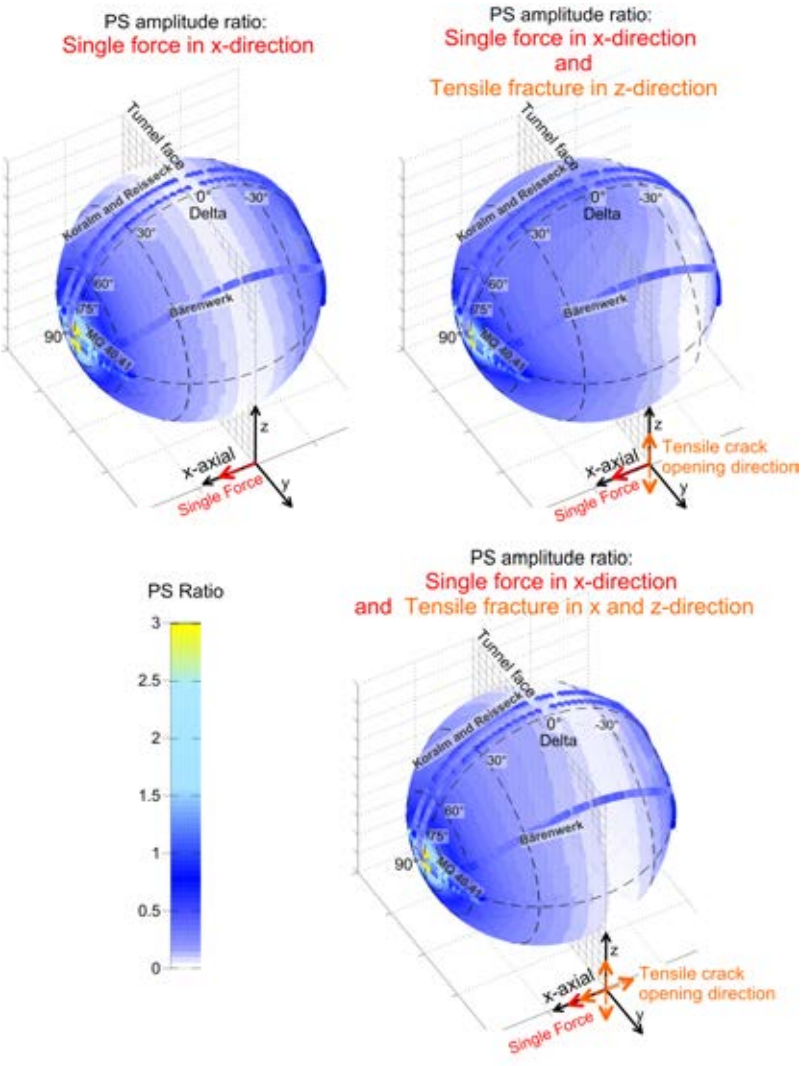

Figure 7.10.: Measured P/S amplitude ratio of the receiver stations along lines above the model for single force, the model for single force and vertical opened tensile fracture and the model for single force and axial and vertical tensile fracture, plotted on the focal sphere.

7.2.1. Attempt to determine crack size

Similar to the comparison of measured and calculated displacements due to the single force, an attempt was made to determine a tensile crack size with the measured velocities of displacements in axial directions. Although these cracks and their opening occur

in several directions this process is partly registered on the pilot sensor. The cutters are accelerated in the axial direction as the opening of the crack and sudden removal of chips lead to a deeper penetration of the cutter. Therefore, it can be concluded that the axial traces after the minimum delay transformation contain also signals of this process.

For shear cracks there exists the following relation between the stress drop ($\Delta\sigma$), the seismic moment (M_0) and size of an circular crack with radius (a) (Stein and Wysession, 2003):

$$\Delta\sigma = \frac{7}{16} * \frac{M_0}{a^3} \tag{7.8}$$

Eaton et al. (2014) adopted this equation for tensile cracks. They define the seismic moment (M_0) as the product of the internal pressure within the crack (P_i), which is equivalently to the tensile stress normal to the crack, and the crack radius (R) as:

$$M_0 = 2P_i a^3 \tag{7.9}$$

The tensile stress normal to the crack corresponds to the tensile strength, which is approx. 10 MPa for gneiss. In general the tensile strength is 10 times smaller than the compressive strength (Prinz and Strauß, 2006).

For the estimation of the magnitude M_0 the Figure 2 in article of McGarr and J. (1990) is used. There the peak-velocity parameter (Rv) is shown as a function of the seismic moment (M_0), R is the distance between the source and receiver and v the measured velocity of displacement. For the chosen examples in Table 7.1 the peak-velocity was calculated with a mean velocity of the axial component and the corresponding distance. Then the seismic moment M_0 was extrapolated out of the trend in Figure 2 of the article. This value is inserted in the equation (7.9) to determine the crack radius (a).

The calculated values for the radius of the crack ranges from 31 - 43 cm. As the chosen signal is the axial component, the calculated values are regarded as the upper limit for the crack radius. We have to consider that the majority of the recorded amplitude is due to a single force and not due to tensile fracturing. For the combined models (see Figure 7.9) the amplitude of the p-wave due to the tensile fracture in the direction of the tunnel axis (Delta = 90°) is only a quarter up to a third of the total value. In the backward direction the amplitude of the p-wave is decreased with the same factor. Therefore the calculated radius can at least be divided by three. Then the radius of the crack is 10 to 15 cm, which is still larger than actual chip size, but approx. in the range of it.

8. Discussion

The discussion outlines the limitations of the findings from to the pilot signal, the gripper as a further source and the observation of the radiation pattern. Further, the final results of the modeling are discussed and uncertainties presented.

Pilot signals

The assumption that the pilot sensor response to an individual event is a minimum delay wavelet is the basis for the processing and interpretation of the TSWD results and the evaluation of the stroke test receiver positions. The results of the TSWD prognosis in regard to the exact determination of structures gave no reasons to change this assumption. The pilot signal was described in detail within this thesis (Chapter 2.2 and Chapter 3.1). With a known transfer function describing the vibration propagation from the cutter position to the pilot sensor position, the assumption would not be necessary.

The pilot sensor positions on the main bearing is efficient for the processing of TSWD, which contains frequencies up to 400 Hz. The limiting factor of the resolution is the recorded signals on the measurement cross-sections. The comparison of the frequency content before and after the minimum delay transformation revealed that the frequencies are decreased between 10 to 30%. The original spectrum may contain local tunnel noies, which results in higher frequencies. The 10 to 30% can be regarded as a maximum improvement of the accuracy.

With the help of the described stroke test a good position for the pilot sensor on the main bearing can be found. However, it was not possible to determine the actual transfer function between the seismic source location at the TBM front and the pilot sensor position at the main bearing. The timing of the test was not perfect. The test should be performed before the machine is working in the tunnel, because when the TBM is in the tunnel space is limited for stroke positions and receiver positions. Further, we were not allowed to hit on the disc cutters and the signal was also recorded at only one position next to the cutters and not at all position. The cutter force measurements while drilling (Entacher et al., 2013) could help to improve the understanding of the transmitted source wavelet, as the actual applied forces are measured on the cutter position. Another approach would be to model the vibrations along the cutterhead and the whole system - TBM head including the main bearing. Models of the TBM

in regard to disc cutter layout and vibration analysis of the TBM already exists (e.g. Rostami (2008), Huo et al. (2010), Zhang et al. (2010), Sun et al. (2013), Li et al. (2014). Other research investigates the influence of geology on the vibration behavior of the TBM - in soft ground and hard rock (e.g. Poisel et al. (2010) and Mooney et al. (2014)).

Gripper as a possible seismic source

The TBM is regarded as a point source (e.g. Brückl et al. (2010)) and a spacial distribution of the seismic source has been neglected for TSWD, although the whole TBM, including the long support sections with containers and the material transporting belt conveyor system to the train, which finally brings the material out of the tunnel, can have a length of over 200 m. The diameter of hard rock TBM can be up to 12.5 m (Herrenknecht). As the gripper transmits the reaction forces during the tunneling into the rock, it should be considered, if they are a further seismic source. The recorded data at the sensor on the gripper (approx. 7 m behind the front face) has significant amplitudes. It cannot be excluded that the transmitted forces into the rock is a relevant factor for the source mechanism. This data set could not be compared with similar data, as no further sensors were placed on the grippers during further projects. It is necessary (Petronio and Poletto, 2006) to measure additionally the forward radiated wave field for a comparison with the backward wave field. The difference in traveltime of a gripper signal in the backward and forward position is about 4 ms, as the gripper positions are approx. 10 m behind the cutters. This is approx. one-third to half of the wavelength, therefore the p-wavelets should be significantly different. The comparison of a recorded p-wavelet at another tunnel station (Koralm) without gripper sensors showed however, that they are very similar. In conclusion, parallel to the tunnel axis, the possible influence of the grippers as a further source can be neglected for TSWD, as the main signals are collected in this direction.

Limitations of the observed radiation pattern

The major task was to record the radiated seismic signals of a TBM in order to determine the radiation pattern with given possibilities at each tunnel projects. First, only surface positions were available. The receiver positions were always on slopes, whereas the underground model to determine the ray paths considered only horizontal layers and surfaces. Mean values for the seismic velocities and densities were assumed for all three surface receivers. A more accurate model would overcome this problem, includ-

ing dipping layers and variable velocities. With the help of a short refraction seismic profile over the receiver station positions the seismic velocities, depths and structures of the surface layer could be obtained. Further, the influence of the free surface has not been considered so far.

The borehole receivers in the tunnel at Koralm were situated in solid rock conditions. These were optimal recording conditions as the second TBM could pass the cross-sections in the other tunnel. However, the traveltimes were to short to separate the p-wave and s-wave wavelets at near offsets to the TBM. Thus, the resulting data within -50° to +50° Delta is limited to surface receivers for the polarization determination and the P/S amplitude ratio. Each degree contains one processed and stacked trace (one meter tunneling). Within -20° until +20° Delta, one meter of advance means even two degrees of Delta. The data quantity within this section is very low, whereas for larger Deltas than +/- 50° Delta the number of data points within one degree increases a lot.

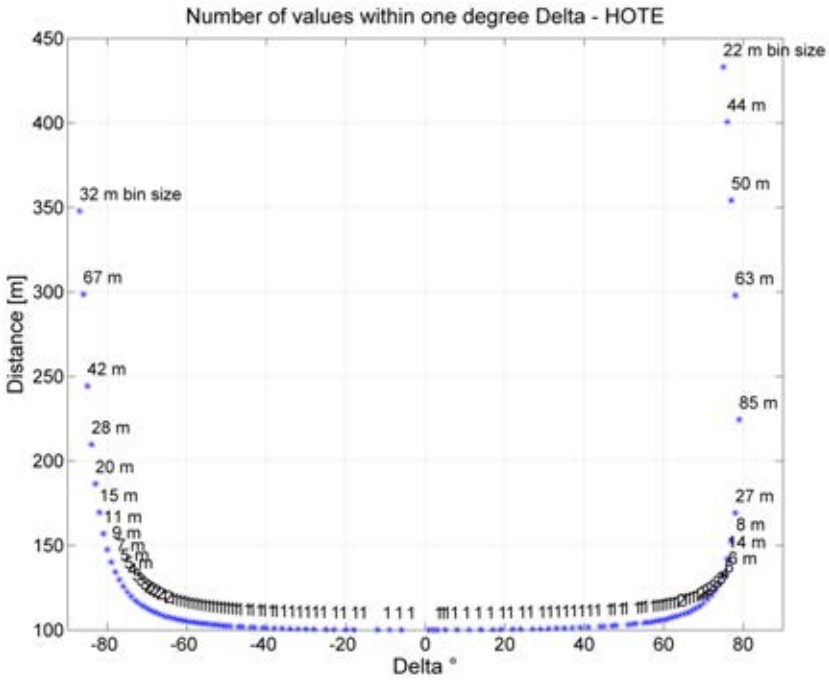

Figure 8.1.: Distance in meter within one degree of Delta for the surface receiver at Reisseck - HOTE; each meter corresponds to one stacked trace.

Therefore, receivers in boreholes from the surface, situated in a depth beneath the weathered zone and with sufficient offsets to the source are necessary for better resolution, especially of the perpendicular to the tunnel axis radiated wave field.

Limitations of the single force model with additional tensile fractures

The stated hypothesis is, that the TBM can be described as a single force source model. As the recorded signals at the cross-sections have wavelengths larger than the tunnel diameter, the source process was presented as a point source applied at the center of the tunnel face. A modeling of multiple source locations on the tunnel face, such as each individual cutter, was not considered.

The radiation pattern of a single force has a cylindrical symmetry, so that the radiation pattern is only dependent on the angle of incidence (Delta). Therefore the comparison of the field data was done only under the consideration of the angle Delta.

The determined polarization of the p-and s-wave confirm the hypothesis. There is a clear change of polarization in the p-wave and no change in the S1-direction of the s-wave (Figure 6.18 in Chapter 6.5). The increasing trend of the P/S ratio is also clearly shown in the datasets (Figure 6.21 in Chapter 6.6). The displacements at the receivers due to a single force was calculated with standard values for a rock and mean values for the measured accelerations of the pilot signal. The values are larger than the measurement displacements at the cross-sections, but are in a plausible range.

However, the increase of the P/S ratio against -90° Delta is not symmetrical to the one against +90° Delta. This is maybe because of the influence of the tunnel in the backward radiated wave field. Uncertainties due to the mentioned limitations exists for the exact location of the change in polarization and for the calculated P/S ratio between -50° and+50°. Nevertheless, the P/S ratios at this location are significant higher than the model values of a single force. P-waves radiated perpendicular to the tunnel axis would explain the higher ratios. The single force model is not sufficient for such waves. This led to the discussion of an additional source mechanism.

The seismic source is related to the cutting process. On the basis of several studies (Chapter 5) Models based on several studies (Chapter 5) of this cutting process are described. Thereby the pressing of the cutters on the tunnel face with normal forces up to 220 kN and the forming of the crushed zone by pulverizing the rock is related to the single force model. Up to 80% of the energy is used for this process. As a possible further source mechanism, the occurring failure modes and directions of cracks within the rock were investigated. The authors proposed different main crack directions and tensile and shear failure modes, depending e.g. on rock conditions and pressure conditions. Mainly single cutters or the interaction of two cutters are described. The exact knowledge of the cutting process performed by various cutters on the TBM is still not completely understood and further research is necessary.

To explain the p-waves in radial directions, a tensile failure mode of the developed crack was chosen. This source mechanism radiates positive polarized p-waves in all direction. Cracks oriented differently would not eliminate their radiated amplitudes. With additional tensile cracks in axial and vertical and 45° angled directions a further approach was presented to explain the ratios around Delta=0°, perpendicular to the tunnel axis. The consideration of shear cracks in various directions is neglected. An axial shear crack does not radiate p-waves in perpendicular direction and, if shear cracks in various directions occur, the p-wave amplitudes would be extinguished.

By adding tensile cracks in various directions the P/S ratio was increased within 0° and +50° Delta. The backward increase was also shifted towards larger negative Deltas. This fits the data better than just the single force model. However, the P/S ratio is decreased within 0° and -50° Delta and the point of the change in the p-wave polarization is shifted towards negative Deltas. The sum of the p-wave amplitude is also zero at this point. The cylindrical symmetry of the radiation pattern is lost at the combined model with only axial tensile fractures. The model with axial and tangential fractures correlate better with the discussed cutting process in Chapter 5 than the model with a dominant axial median crack after Rostami and Ozdemir (1993).

Contrary to the proposed models, the findings from the field data show the change of p-wave polarization always around Delta 0°. There is no point where the p-wave amplitude is zero. A proposed explanation is that the opening of the cracks in various directions may not be at the same time and therefore, after the summation the change of polarization and the zero amplitude varies in the section of 0° until -40°. The number of data points is less in this section and the P/S ratios here are limited to the surface receivers, so a point of zero p-wave might never recorded.

The calculation of the tensile crack radius is based on a rough estimation of the seismic source moment and the tensile rock strength. The ratio of a tensile fracture signal on an axial receiver component is only estimated of the proposed model. Therefore the values for the crack radius with 10-15 cm are still large for a mean disc cutter distance of 6.5 to 10 cm.

Still, the observed data cannot be fully explained with the proposed single force model and with additional tensile cracks too. The interaction of different crack directions and failure modes is apparently more complex and further investigations should be done.

9. Conclusions and outlook

- For the processing and interpretation of TSWD data it was assumed that the response of the pilot sensor to an individual event is a minimum delay wavelet, which is recorded at the main bearing on the TBM. With the help of a stroke test, an optimum position of the pilot sensors can be determined according to the assumption. By comparison of the signal lengths and frequencies unwanted noisy positions can be avoided. The determined transfer function with the data of the sledge test is not sufficient to determine the actual transfer function. The assumption of a minimum delay source wavelet recorded on the pilot signal is valid for TSWD.

- Moreover, the gripper as a further source of seismic waves can be neglected for the presented TSWD projects. The radiated wavelet at Koralm is very similar in both axial directions. It should be different in case of a further source. But, it has to be verified again for further projects.

- The observation of the radiated wave field of several TBM's was successfully recorded by surface and borehole receivers in a tunnel. The polarization of the p-wave and s-wave and the P/S amplitude ratio could be clearly determined, especially for the radiation directions nearly parallel until 40° angled to the tunnel axis. The results are consistent for all sites, independently on the characteristics of the TBM-type and geology on site. The resulting wave polarization strongly support the hypotheses, that the source mechanism of a TBM can be described with the single force model. The maximum p-wave amplitude is radiated parallel to the tunnel axis, positive polarized in advance direction of the TBM and negative polarized against the advance direction. The s-waves amplitude maximum is perpendicular to the tunnel axis.

- The P/S ratio of the data showed that p-waves are radiated perpendicular to the tunnel axis too. This is explained by additional tensile cracks in axial and tangential directions.

- The calculated displacements due to a single force and tensile crack sizes are in the size range with the actual measured displacements and chip sizes.

- The single force is related to the force of the TBM, which presses the cutters against the tunnel face in axial directions and breaks the rock beneath. The

tensile failure mode and directions of the developed cracks correspond to the described mechanism of the cutting process.

The single force model is sufficient within the -90° until -40° and +40° until +90° Delta. The measured and used data for the processing and interpretation of TSWD lie within these Delta sections. Thus, for steeply vertically to the tunnel axis orientated structures (50°-90°), p-wave reflections (PP) parallel to the tunnel axis prevail. If the reflecting structures are ten toward horizontal to the tunnel axis, s-wave to p-wave reflections (SP) must be considered, as many s-wave amplitudes are radiated perpendicular and angled up to 40° to the tunnel axis. With the knowledge of the single force mechanism, the correct wave type (is it a PP or a SP reflection) and thus correct intersections can be determined.

The radiated seismic waves of a TBM in hard rock are now only used for TSWD. But the source is also suitable for other seismic applications, e.g. investigations of the rock above the tunnel, especially with a high overburden as the range of the signals is large (up to 1km). It was assumed that only s-waves are radiated perpendicular to the tunnel axis, however, it could be shown that also p-waves are also radiated in this direction. For possible tomographic measurements this has to be considered and can used for the analyses.

Outlook

There are still uncertainties especially in the section perpendicular to the tunnel axis. Further investigations with borehole receivers in solid rock conditions and enough offset to the source would deliver good data sets to overcome the mentioned uncertainties.

As it is now possible to measure the cutter forces while drilling (Entacher et al., 2013), a comparison of the measured forces and registered accelerations on the main bearing could improve the understanding of the applied forces and the radiated seismic waves. Until now the force measurements were limited to some cutter positions on the TBM head and sampling rate of 100 Hz. More measured cutter positions and higher sampling rates would be necessary to investigate, if the measured actual forces could help to determine the initial source wavelet and a transfer function for the pilot signal.

The grippers as a potential further seismic source could be rarely investigated in the scope of this work. For future projects, sensors should be placed also on the grippers. Moreover, measurements of the wavelets in the forward direction are necessary for the verification of the grippers as a source.

Appendix A.

Original frequency spectrum of receiver signals

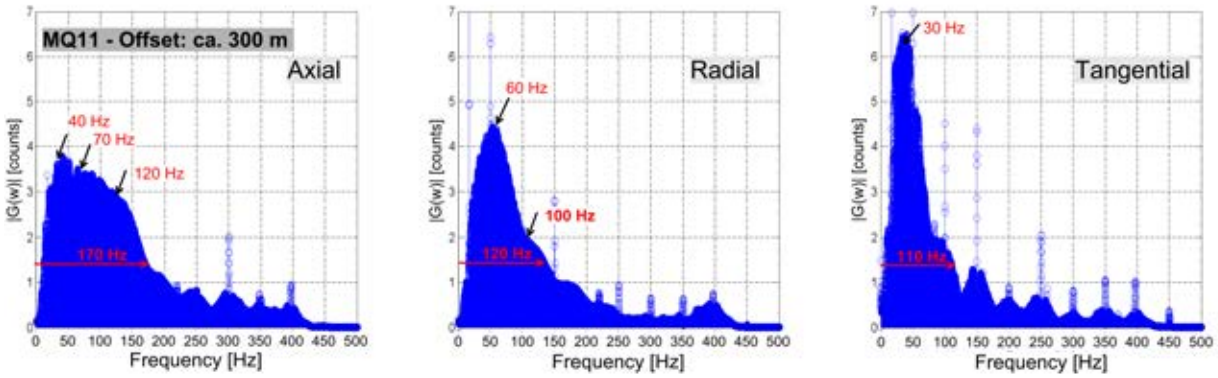

Figure A.1.: Frequency spectrum of receiver station MQ11 at Reisseck, arrows indicate local maximums and range.

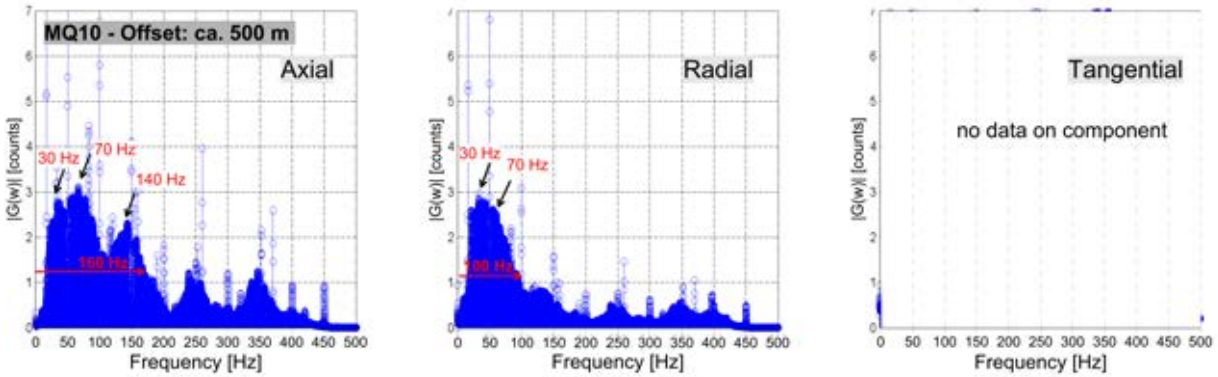

Figure A.2.: Frequency spectrum of receiver station MQ10 at Reisseck, arrows indicate local maximums and range.

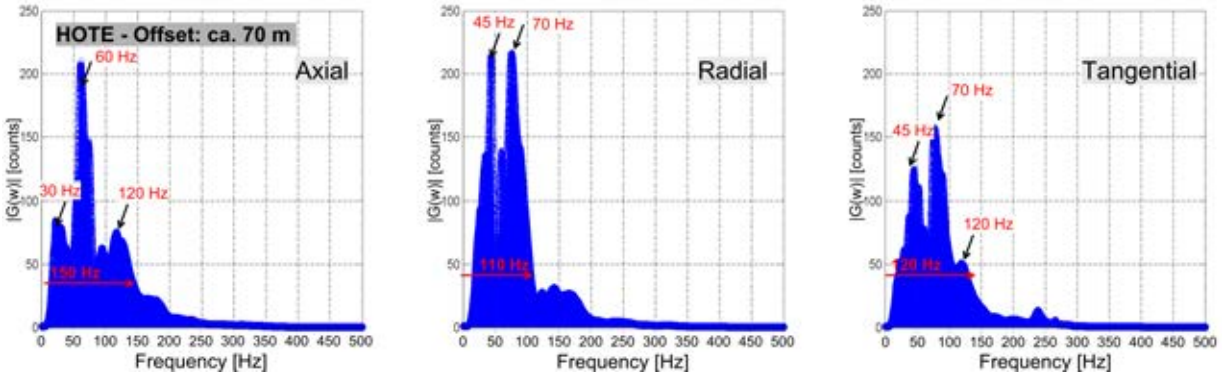

Figure A.3.: Frequency spectrum of receiver stations at Reisseck, HOTE with different offsets; arrows indicate local maximums and range.

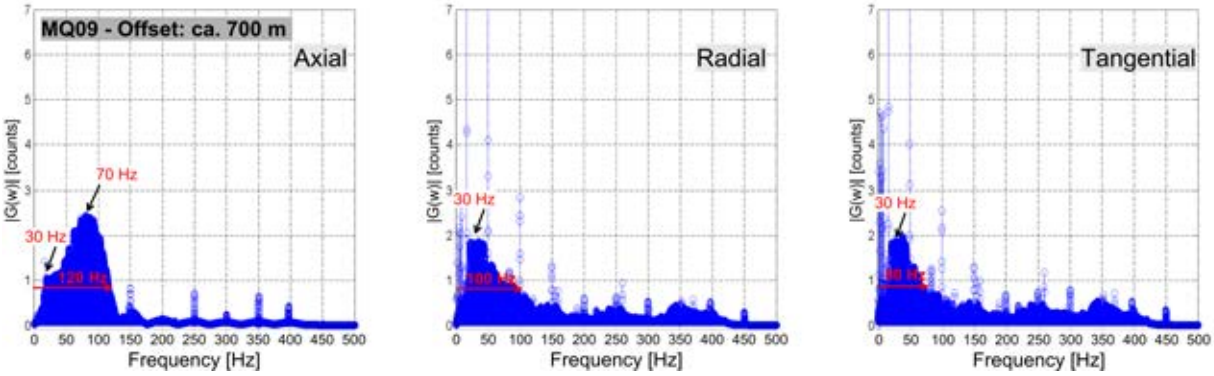

Figure A.4.: Frequency spectrum of receiver station MQ09 at Reisseck, arrows indicate local maximums and range.

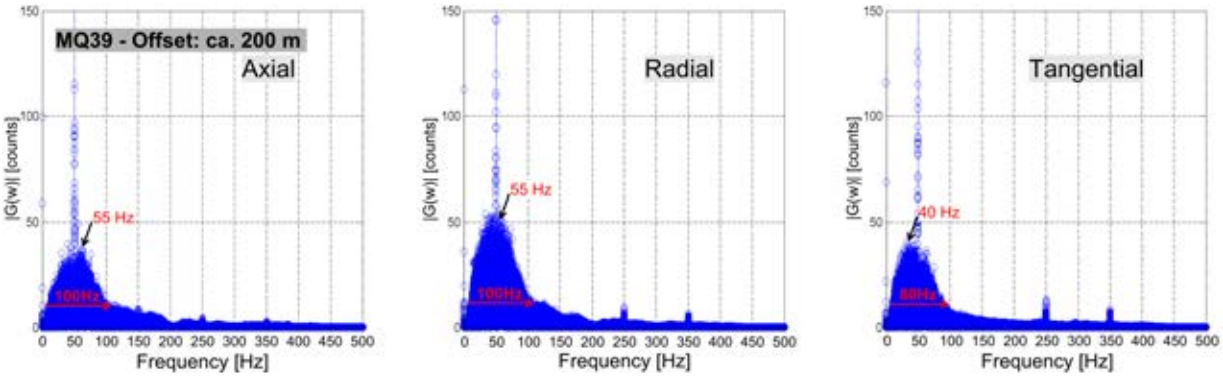

Figure A.5.: Frequency spectrum of receiver stations at Koralm, MQ39, arrows indicate local maximums and range.

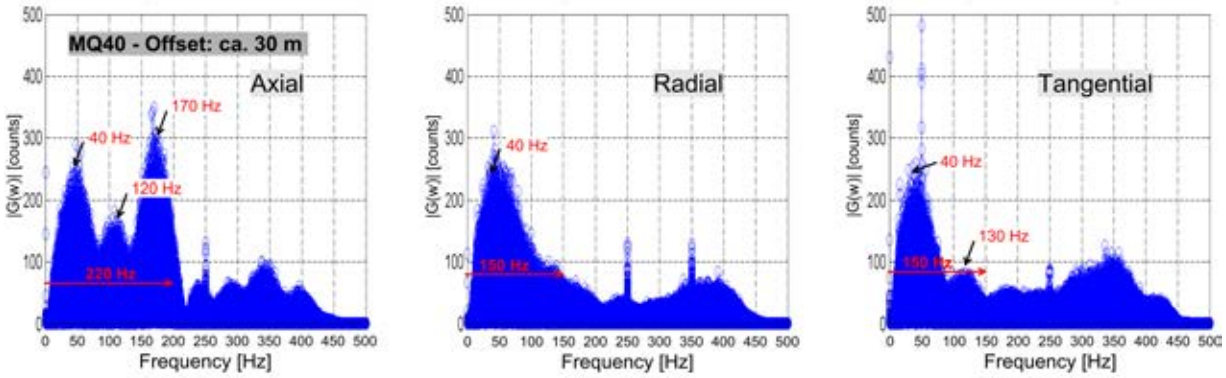

Figure A.6.: Frequency spectrum of receiver stations at Koralm, MQ40, arrows indicate local maximums and range.

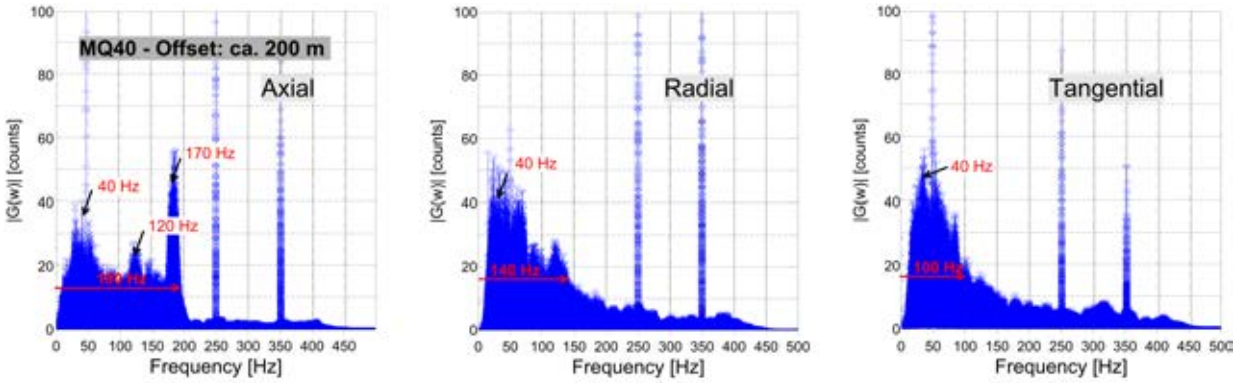

Figure A.7.: Frequency spectrum of receiver stations at Koralm, MQ40 with 200 m offset, arrows indicate local maximums and range.

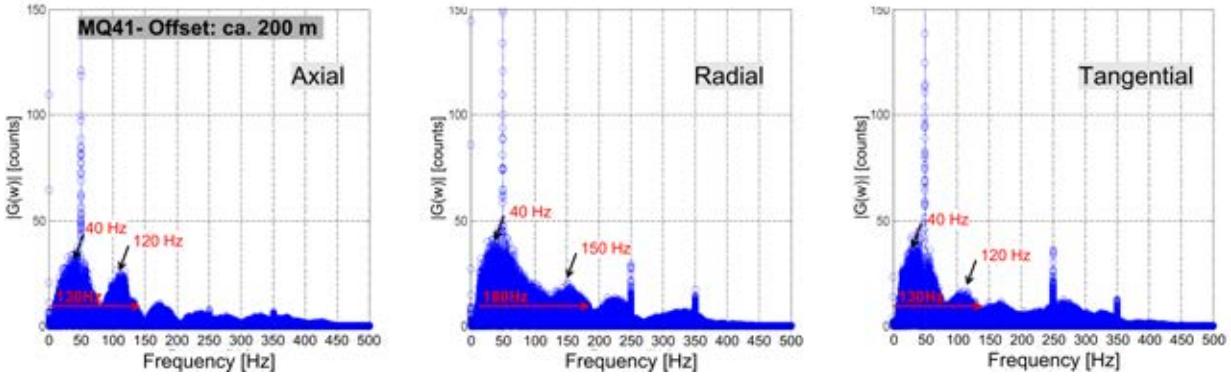

Figure A.8.: Frequency spectrum of receiver stations at Koralm, MQ41, arrows indicate local maximums and range.

Appendix B.

Minimum delay transformation with gripper components

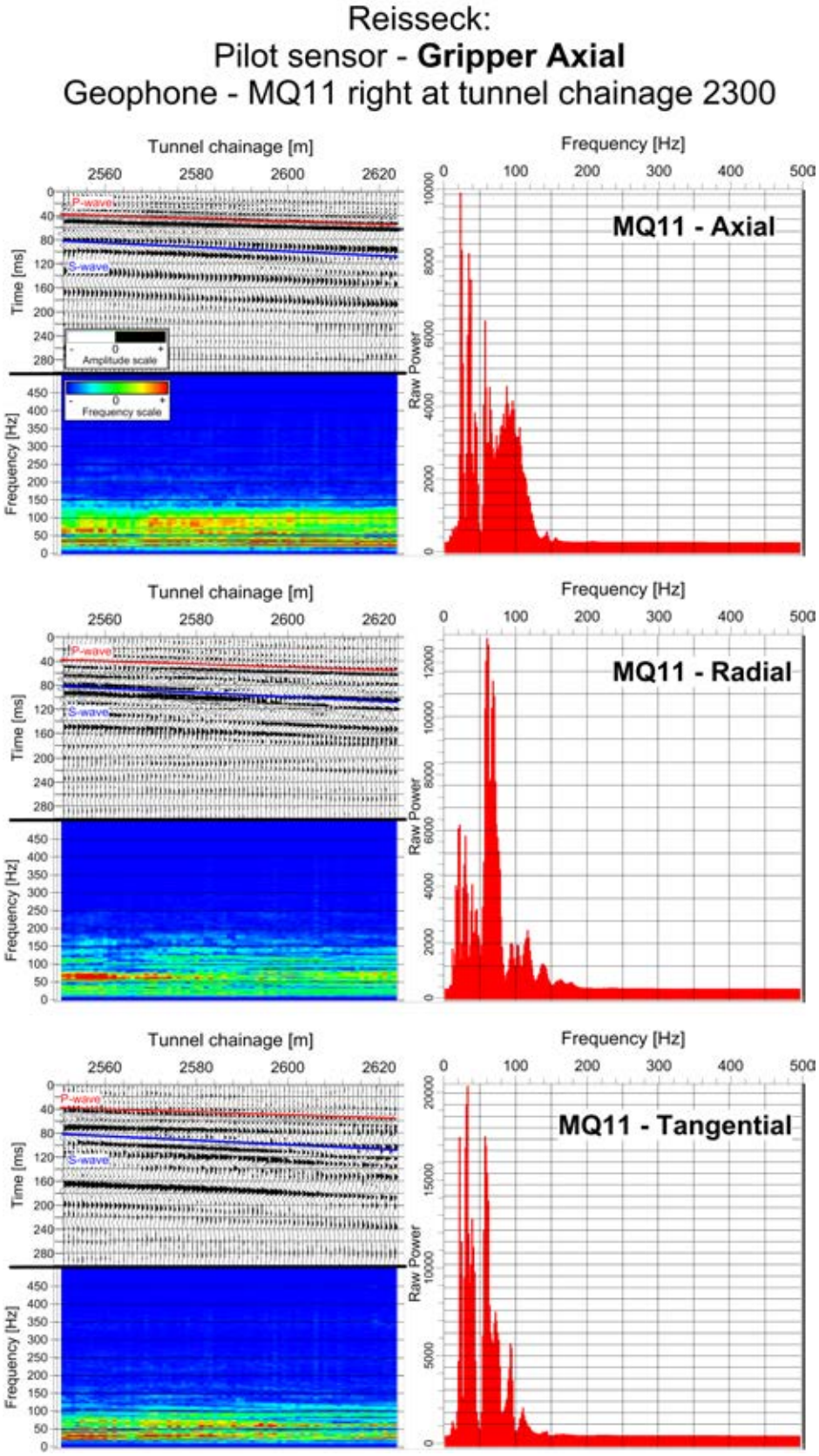

Figure B.1.: Processed traces and their frequency content (offset: 255 - 400 m) of the right geophone components of MQ11 at Reisseck. The minimum delay transformation used the axial component on the gripper. The red and blue lines in the seismic section show the first break of the p- and s-wave.

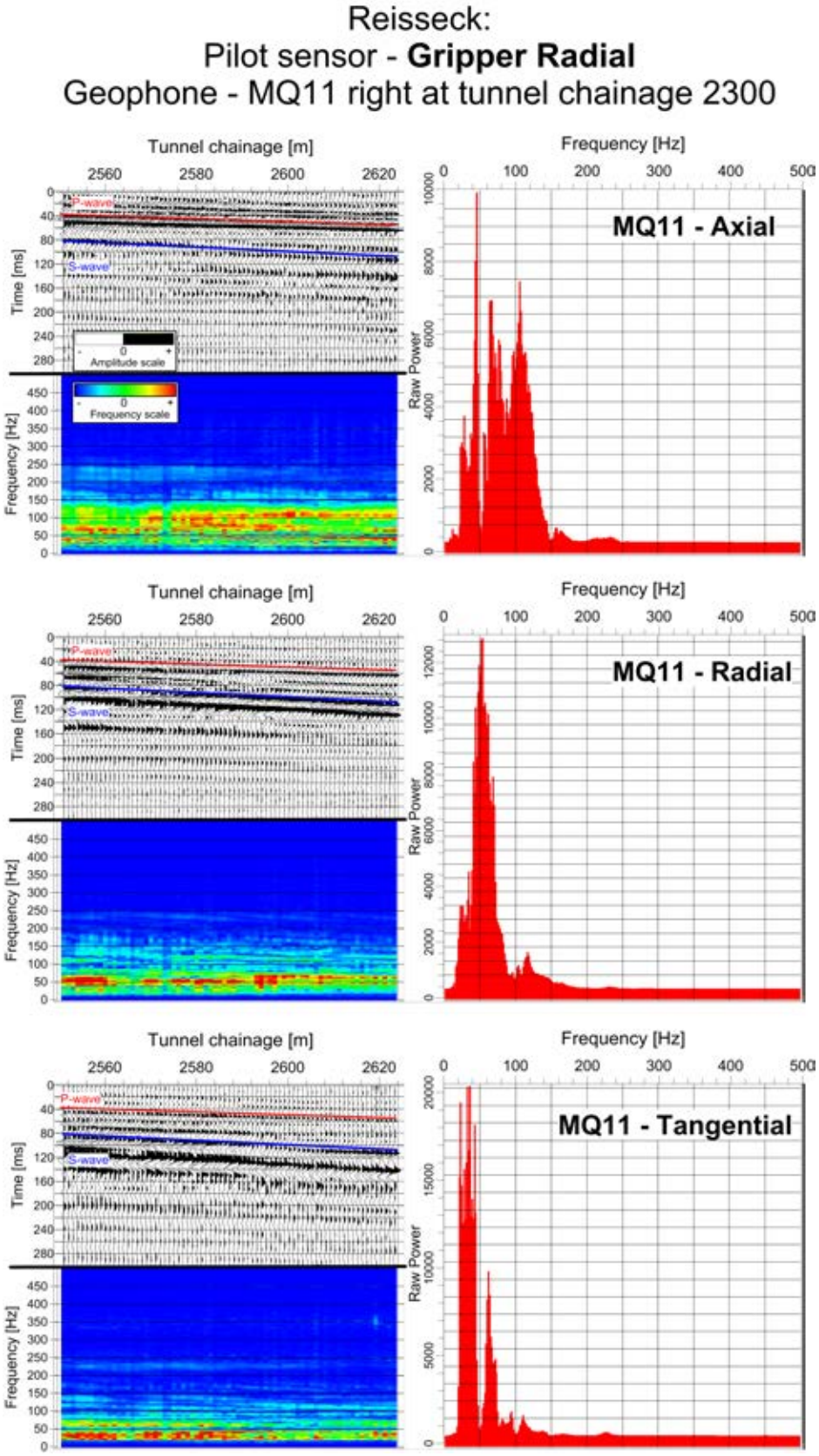

Figure B.2.: Processed traces and their frequency content (offset: 255 - 400 m) of the right geophone components of MQ11 at Reisseck. The minimum delay transformation used the radial component on the gripper. The red and blue lines in the seismic section show the first break of the p- and s-wave.

Appendix C.

First break picking

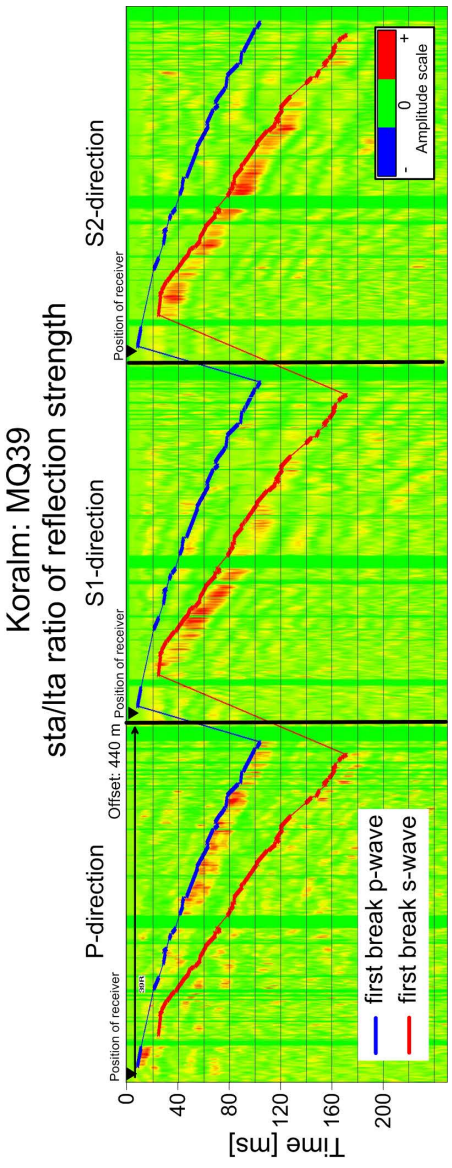

Figure C.1.: sta/lta ratio of receiver stations MQ39, blue line indicates p-wave first break, red line the s-wave first break.

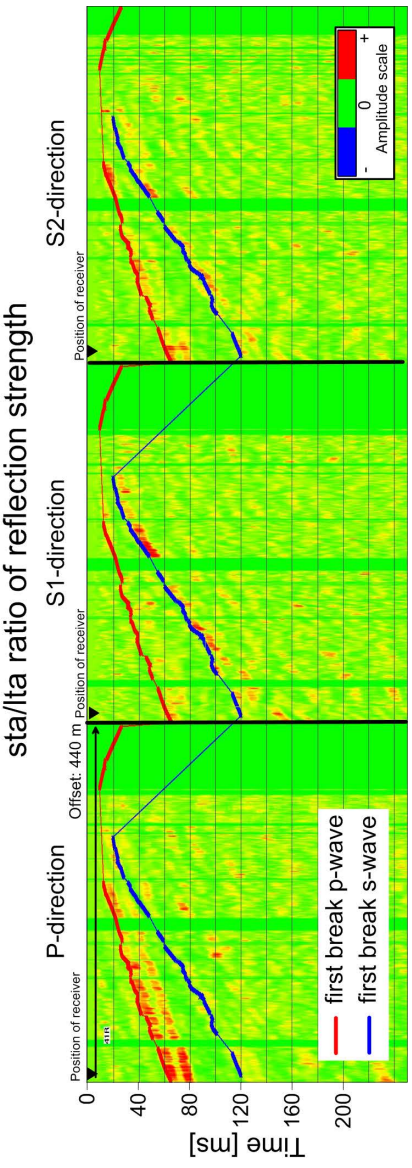

Figure C.2.: sta/lta ratio of receiver stations MQ41, red line indicates p-wave first break, blue line the s-wave first break.

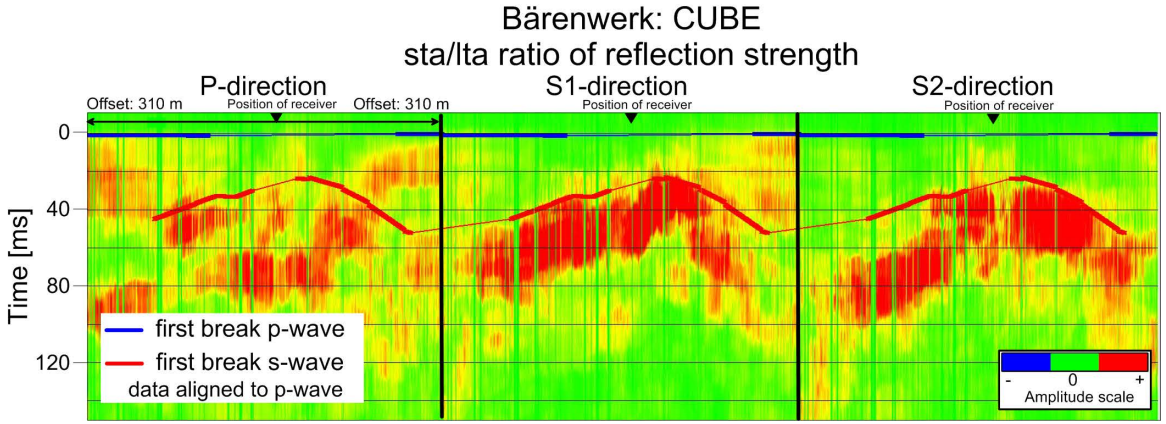

Figure C.3.: sta/lta ratio of receiver stations CUBE, blue line indicates p-wave first break, red line the s-wave first break.

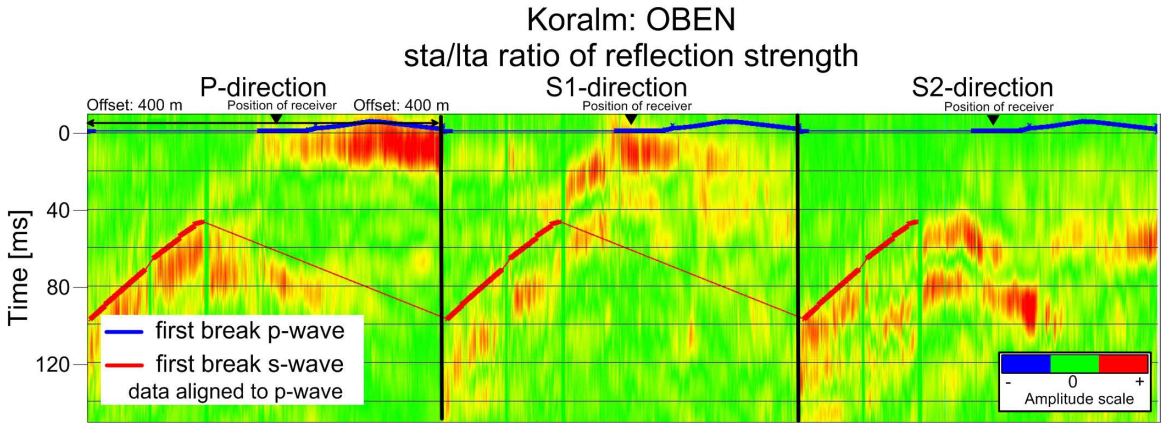

Figure C.4.: sta/lta ratio of receiver stations OBEN, blue line indicates p-wave first break, red line the s-wave first break.

Appendix D.

Correlation with common wavelet

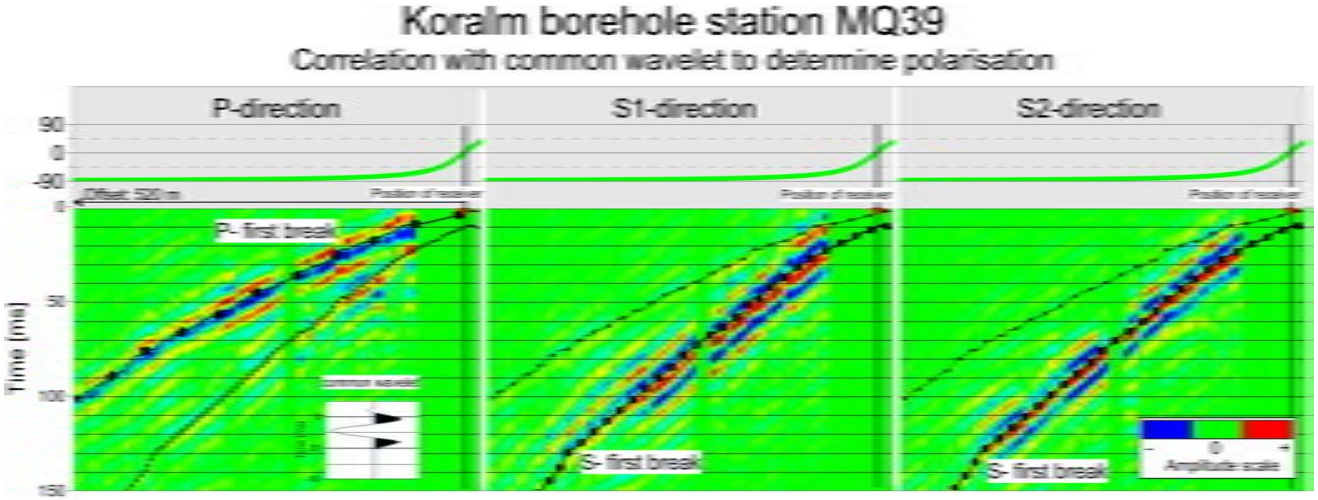

Figure D.1.: Correlation with common wavelet of receiver stations MQ39, blue line indicates p-wave first break, red line the s-wave first break.

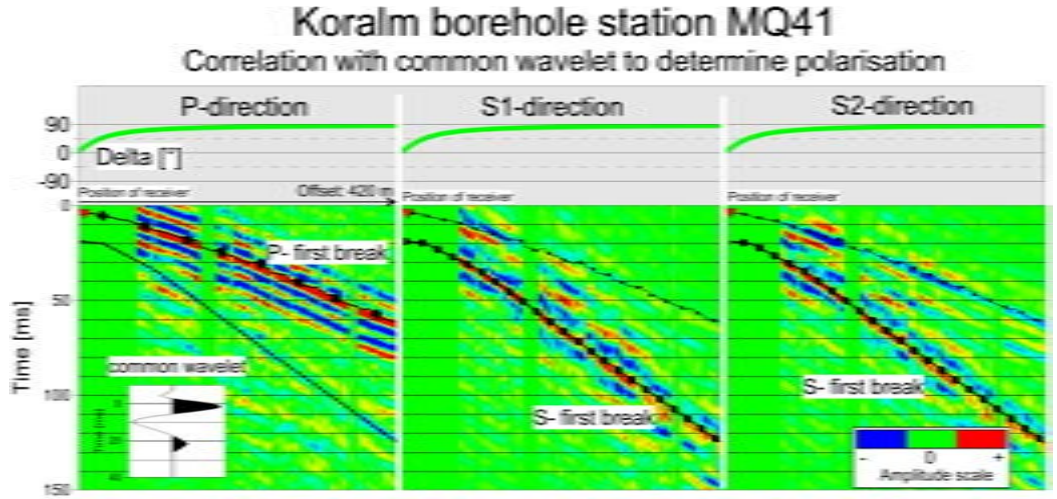

Figure D.2.: Correlation with common wavelet of receiver stations MQ41, red line indicates p-wave first break, blue line the s-wave first break.

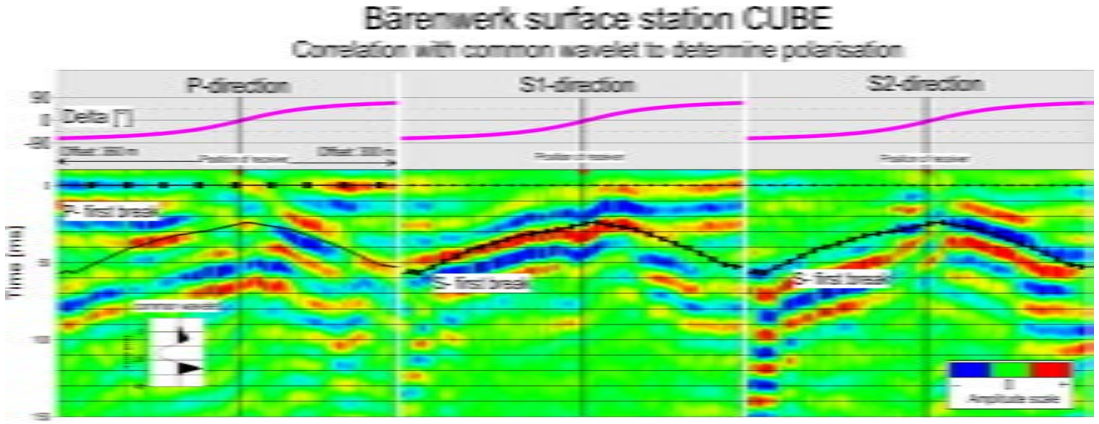

Figure D.3.: Correlation with common wavelet of receiver stations CUBE, blue line indicates p-wave first break, red line the s-wave first break.

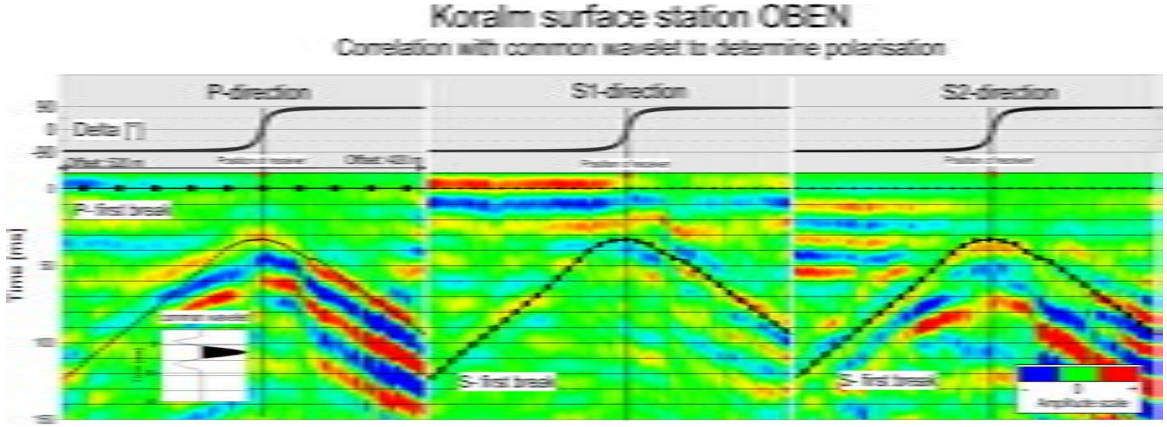

Figure D.4.: Correlation with common wavelet of receiver stations OBEN, blue line indicates p-wave first break, red line the s-wave first break.

Bibliography

Aki, K. and Richards, P. (2002). *Quantitative Seismology*. Universitiy Science Books, 2nd edition.

Benecke, N., Dombrowski, B., and Lehmann, B. (2008). Trust – exploration ahead of the tunnel face for reducing tunnelling risks and supporting decision-making. *World Tunnel Congress - Underground Facilities for Better Environment and Safety*, pages 1124–1129.

Bohlen, T., Lorang, U., Rabbel, W., Müller, C., Giese, R., Lüth, S., and Jetschny, S. (2007). Rayleigh-to-shear wave conversion at the tunnel face — from 3D-FD modeling to ahead-of-drill exploration. *Geophysics*, Volume 72, NO.6:T67–T79.

Brückl, E., Chwatal, W., Dölzmüller, J., and Jöbstl, W. (2001). A study of the application of VSP to exploration ahead of a tunnel. *International Journal of Rock Mechanics and Mining Sciences*, 38:833–841.

Brückl, E., Chwatal, W., Mertl, S., and Radinger, A. (2008). Exploration ahead of a tunnel face by TSWD Tunnel Seismic While Drilling. *Geomechanics and Tunnelling*, Volume 1, Issue 5:460–465.

Brückl, E., Chwatal, W., Mertl, S., and Radinger, A. (2010). Continuous exploration ahead of a tunnel face by TSWD - Tunnel Seismic While Drilling. *Proceedings at 23rd SAGEEP - EEGS Annual Meeting Keystone*, pages 353–360. April 11-15.

Buske, S., Lüth, S., and Giese, R. (2006). Fresnel-volume-migration and reflection-image-spectroscopy of tunnel seismic datasets. *EAGE 68th annual meeting and technical exhibition*, Expanded Abstracts. W9-09.

Chen, L. and Labuz, J. (2006). Indentation of rock by wedge-shaped tools. *International Journal of Rock Mechanics and Mining Sciences*, 43:1023–1033.

Chwatal, W., Radinger, A., Brückl, E., Mertl, S., and Freudenthaler, A. (2011). Tunnel Seismic While Drilling – state of the art and new developments. *Proceedings of the ITA-AITES World Tunnel Congress*. May 20-26.

Cigla, M. and Ozdemir, L. (2000). Computer modeling for improved production of mechanical excavators. *In: Society for Mining, Metallurgy and Exploration (SME) annual meeting, Salt Lake City, Preprint No. 00-65*, pages 1–12.

Cook, N., Hood, M., and Tsai, F. (1984). Observation of crack growth in hard rock loaded by an indenter. *International Journal of Rock Mechanics and Mining Sciences*, 21:165–182.

Dickmann, T. (2005). Seismische Vorauserkundung beim Vortrieb von Tunneln im Festgestein. *65th annual meeting of the German Geophysical Society (DGG)*, Sonderband I. DGG-Kolloquium: Geophysik zur Vorerkundung von Tunneln.

Dickmann, T. (2008). Theoretical and applied case studies of seismic imaging in tunnelling. *Geomechanics and Tunnelling*, Volume 1, Issue 5:436–441.

Dickmann, T. and Krueger, D. (2013). Is geological uncertainty ahead of the face controllable? *Proceedings of the World Tunnel Congress 2013 - Underground -the way to the future!* G. Anagnostou and H. Ehrbar (eds).

Dickmann, T. and Krueger, D. (2014). How to turn geological uncertainty into manageable risk? *Proceedings of the World Tunnel Congress 2014 - Tunnels for a better Life*.

Eaton, D., van der Baan, M., Birkelo, B., and Tary, J.-B. (2014). Scaling relations and spectral characteristics of tensile mircroseisms: evidence for opening/closing cracks during hydraulic fracturing. *Geophysical Journal International*, 196:1844–1857.

Entacher, M., Schuller, E., and Galler, R. (2015). Rock failure and crack propagation beneath disc cutters. *Rock Mechanics and Rock Engineering*, 48:1559–1572.

Entacher, M., Winter, G., Bumberger, T., Decker, K., Godor, I., and Galler, R. (2012). Cutter force measurement on tunnel boring machines - system design. *Tunnelling and Underground Space Technology*, 31:97–106.

Entacher, M., Winter, G., and Galler, R. (2013). Cutter force measurement on tunnel boring machines - implementation at Koralm tunnel. *Tunnelling and Underground Space Technology*, 38:487–496.

Flores Orozco, A., Kemna, A., and Zimmermann, E. (2012). Data error quantification in spectral induced polarization imaging. *Geophysics*, 77(3):E227–E237.

Gehring, K. (1995). Leistungs- und Verschleißprognosen im maschinellen Tunnelbau. *Felsbau 13*, 13:439–448. in German.

Gehring, M., Kassel, and Lorenz, K. (2010). Vortriebsbegleitende Vorauserkundung: Mixschild mit Weitblick. *Tunnel*, Jg.29, Nr. 3:14–29.

Gertsch, R. (2000). *Rock Toughness and Disc Cutting*. PhD thesis, University of Missouri-Rolla.

Gertsch, R., Gertsch, L., and Rostami, J. (2007). Disc cutting tests in colorado red granite: Implications for TBM performance prediction. *International Journal of Rock Mechanics and Mining Sciences*, 44:238–246.

Giese, R., Klose, C., Otto, P., Selke, C., and Borm, G. (2002). Seismische Tomographie-Messungen beim Tunnelbau unter Tage in den Schweizer Zentralalpen. *Zweijahresbericht GFZ Potsdam*.

Gong, Q.-M., Zhao, J., and Jiao, Y.-Y. (2005). Numerical modeling of the effects of joint orientation on rock fragmentation by tbm cutters. *Tunnelling and Underground Space Technology*, 20:183–191.

Hardage, B. (2000). *Vertical Seismic Profiling. Third updated and revised edition*. Handbook of Geophysical Exploration.

Heinö, M. (1999). *Rock Excavation Handbook*. Copyright Sandvik Tamrock Corp.

Herrenknecht. Tunnelling - Single Shield TBM, Double Shield TBM and Gripper TBM. `https://www.herrenknecht.com/en/products/core-products/tunnelling.html`. Accessed: 2015-06-08.

Howarth, D. and Bridge, E. (1988a). Microfracture beneath blunt disc cutters in rock. *International Journal of Rock Mechanics and Mining Sciences and Geomechanics Abstracts*, 25:35–38.

Howarth, D. and Bridge, E. (1988b). Observation of Cracks at the Bottom of Percussion and Diamond Drill Holes. *International Journal of Rock Mechanics and Mining Sciences and Geomechanics Abstracts*, 25:39–43.

Huang, H., Damjanac, B., and Detournay, E. (1998). Normal wedge indentation in rocks with lateral confinement. *Rock Mechanics and Rock Engineering*, 31:81–94.

Huo, J., Sun, W., Chen, J., Su, P., and Deng, L. (2010). Optimal disc cutter plan layout design of the full-face rock tunnel boring machine (tbm) base on a multi-objective genetic algorithm. *Journal of Mechanical Science and Technology*, 24:521–528.

Innaurato, N., Oggeri, C., Oreste, P., and Vinai, R. (2007). Experimental and Numerical Studies on Rock Breaking with TBM Tools under High Stress Confinement. *Rock Mechanics and Rock Engineering*, 40:429–451.

Kneib, G., Kassel, A., and Lorenz, K. (2000). Automatic seismic prediction ahead of the tunnel boring machine. *First Break*, Volume 18, Issue 7:295–302.

Kreutzer, I., Chwatal, W., Echiner, H., Kostial, D., Freudenthaler, A., Randiger, A., and Larcher, M. (2012). Tunnel Seismic While Drilling TSWD als unterstützendes Tool für die geologische Tunnelprognose - Entwicklung und Fallbeispiele. In *PANGEO Austria 2012 Abstracts*, page 82.

Lawn, B. and Wilshaw, R. (1975). Indentation fracture: principles and applications. *Journal of Materials Science*, 10:1049–1081.

Li, X., Yu, H., Zeng, P., Yuan, M., Sun, L., and Zhao, Y. (2014). Dynamic tow-dimensional nonlinear vibration modeling and analysis for shield TBM cutterhead driving system. *Transaction of the Canadian Society for Mechanical Engineering*, 38, No. 4:417–463.

Lindqvist, P.-A., Lai, H., and Alm, O. (1984). Indentation Fracture Development in Rock Continuously Observed with a Scanning Electron Microscope. *International Journal of Rock Mechanics and Mining Sciences*, 21:97–107.

Liu, H., Kou, S., Lindqvist, P.-A., and Tang, C. (2002). Numerical simulation of the rock fragmentation process induced by indenters. *International Journal of Rock Mechanics and Mining Sciences*, 39:491–505.

Lorang, U., Bohlen, T., Rabbel, W., and Müller, C. (2005). Seismic prediction ahead of tunnel construction using rayleigh to body wave conversion. *65th annual meeting of the German Geophysical Society (DGG)*, Sonderband I/2005. DGG-Kolloquium: Geophysik zur Vorerkundung von Tunneln.

Lüth, S., Giese, R., Otto, P., Krüger, K., Mielitz, S., and Borm, G. (2005). Seismische Vorauserkundung im Tunnelbau mit konvertierten Oberflächenwellen. *Zweijahresbericht GFZ Potsdam*.

Lüth, S., Giese, R., and Rechlin, A. (2008). A seismic exploration system around and ahead of tunnel excavation – Onsite. *World Tunnel Congress - Underground Facilities for Better Environment and Safety*.

Ma, H., Yin, L., and Ji, H. (2011). Numerical study of the effect of confining stress on rock fragmentation by TBM cutters. *International Journal of Rock Mechanics and Mining Sciences*, 48:1021–1033.

Marji, M., Nasab, H., and Morshedi, A. (2009). Numerical modeling of crack propagation in rocks under TBM disc cutters. *Journal of Mechanics and Materials and Structures*, 4, No.3:605–627.

McGarr, A. and J., B. (1990). Estimation of the near-fault ground motion of mining-induced tremors from locally recorded seismograms in South Africa. *Rockburtsts and seismicity in mines*, pages 245–248.

Mishnaevsky JR, L. (1995). Physical mechanisms of hard rock fragmentation under mechanical loading: A review. *International Journal of Rock Mechanics and Mining Sciences and Geomechanics Abstracts*, 32:763–766.

Mooney, M., Walter, B., J., S., and D., C. (2014). Influence of Geological Conditions on Measured TBM Vibration Frequency. In *North American Tunneling: 2014 Proceedings*, pages 32–41. Society of Mining, Metallurgy & Exploration Inc.

Pang, S. and Goldsmith, W. (1990). Investigation of crack formation during loading of brittle rock. *Rock Mechanics and Rock Engineering*, 23:53–63.

Petronio, L. and Poletto, F. (2002). Seismic-while-drilling by using tunnel-boring-machine noise. *Geophysics*, Volume 67:1798–1809.

Petronio, L. and Poletto, F. (2006). Tunnel Seismic while Drilling (TSWD) Method – A New Approach to Predict Interfaces ahead of the Tunnel Front. In *68th EAGE Conference and Exhibition incorporating SPE Europec 2006, Workshop 9.* From Alpine to Urban Tunnels.

Petronio, L., Poletto, F., Schleifer, A., and Morino, A. (2003). Geology prediction ahead of the excavation front by Tunnel-Seismic-While-Drilling (TSWD) method. In *Society of Exploration Geophysicists, Expanded Abstracts.* 73rd Annual International Meeting.

Poisel, R., Tentschert, E., Preh, A., Ostermann, V., Chwatal, W., and Zettler, A. (2010). The interaction of machine and rock mass analysed using TBM data and rock mass parameters. *Geomechanics and Tunnelling*, 3, No. 5:510–519.

Poletto, F. and Miranda, F. (2004). Seismic while drilling. Fundamentals of drill-bit Seismic for exploration. Handbook of seismic exploration. *Seismic exploration series*, Volume 35.

Prinz, H. and Strauß, R. (2006). *Abriss der Ingenieurgeologie.* Elsevier, 4. edition.

Rabensteiner, S. (2012). Numerische Berechnungen für eine bessere Erkennung von reflexionsseismischen Strukturen bei der TSWD-Methode. B.s.thesis, Technische Universtität Wien, Department für Geodäsie und Geoinformation.

Radinger, A., Fasching, F., Pack, G., Kreutzer, I., and Kostial, D. (2014). Consistent exploration by probe drilling and TSWD through the example of the Koralm tunnel. *Geomechanics and Tunnelling*, Volume 7, No.4:540–550.

Rostami, J. (2008). Hard Rock TBM Cutterhead Modeling for Design and Performance Prediction. *Geomechanics and Tunnelling*, Volume 1, Issue 1:18–28.

Rostami, J. and Ozdemir, L. (1993). A new model for performance prediction of hard rock TBMS. *In: Proceedings of the Rapid Excavation and Tunneling Conference, Boston, USA*.

Samuel, A. and Seow, L. (1984). Disc Force Measurements on a Full-face Tunnelling Machine. *International Journal of Rock Mechanics and Mining Sciences*, 21:83–96.

Schneider, E., Thuro, K., and Galler, R. (2012). Forecasting penetration and wear for TBM drives in hard rock – results from the ABROCK research project. *Geomechanics and Tunnelling*, Volume 5, Issue 5:537–546.

Stein, S. and Wysession, M. (2003). *An introduction to seismology, earthquakes and earth structure*. Blackwell Publishing Ltd.

Su, O. and Akcin, N. (2011). Numerical simulation of rock cutting using the discrete element method. *International Journal of Rock Mechanics and Mining Sciences*, 48:434–442.

Sun, W., Ling, J., Huo, J., Guo, L., Zhang, X., and Deng, L. (2013). Dynamic characteristics study with multidegree-of-freedom coupling in TBM cutterhead system based on complex factors. *Mathematical Problems in Engeneering*, 2013. Article ID 63509, 17 pages.

Tan, X., Lindqvist, P.-A., and Kou, S. (1997). Application of a splitting fracture model to the simulation of rock indentation subsurface fractures. *International Journal for Numerical and Analytical Methods in Geomechanics*, 21:1–13.

Thuro, K. and Schormair, N. (2008). Fracture propagation in anisotropic rock during drilling and cutting. *Geomechanics and Tunnelling*, Volume 1, Issue 1:8–17.

Walter, B. (2013). Detecting changing geologic conditions with tunnel boring machines by using passive vibration measurements. Phd thesis, Colorado School of Mines, College of Engineering and Computational Science.

Wang, S., Sloan, S., Liu, H., and Tang, C. (2011). Numerical simulation of the rock fragmentation process induced by two drill bits subjected to static and dynamic (impact) loading. *Rock Mechanics and Rock Engineering*, 44:317–332.

Zhang, K., Xia, Y.-M., Tan, Q., and Xu, Z.-J. (2010). Establishment and dynamic analysis of vibration model of TBM disc cutter in the rolling direction. *International Conference on Electrical and Control Engineering*, pages 919–921.

Zhang, Z., Kou, S., and Lindqvist, P.-A. (2003). In-situ Measurements of Cutter Forces on Boring Machine at Äspö Hard Rock Laboratory Part II.Characteristics of Cutter Forces and Examination of Cracks Generated. *Rock Mechanics and Rock Engineering*, 36:63–83.

CURRICULUM VITAE

Name: **DI Ingrid SCHLÖGEL**
Née Kreutzer
Date of birth: 19.04.1983
Nationality: Austria
Address: Schickgasse 25/2/3
1220 Wien

EDUCATION:

2011 – 2015	Doctoral programme in Engineering Sciences Surveying and Geoinformation; TU Wien - Vienna University of Technology Dissertation thesis: A better understanding of the tunnel boring machine as a seismic source for Tunnel Seismic While Drilling.
2001 – 2008	Montan University of Leoben – Applied Geosciences Master thesis: Geophysical surveys to verify the groundwater situation along the river Aschach at the egde of the Molassebasin of Eferding - Water protection zone Hartkirchen.
1997 – 2001	Oberstufenrealgymnasium Vöcklabruck

WORK EXPERIENCE:

2008 – 2011	Geophysicist at Pöyry-Infra GmbH, Salzburg, Austria. Team leader and project leader of geophysical measurements (Seismic, Ground Penetrating Radar, Magnetic, Geoelectric) in Austria, Czech Republic and Slovenia.
2011 – 2015	Research assistance at TU Wien – Vienna University of Technology Department for Geodesy and Geoinformation, Research group Geophysics

Additional Qualifications

Blasting licence
Driving licence B +E, F
Knowledge of specific software (Office, Reflexw, Promax, Res2DInv, AutoCAD, Golden Software, Matlab, etc.)

Oral and Poster Presentations:

2015	EGU- European Geosciences Union, General Assembly in Vienna, Austria. Poster: Kreutzer, I., Brückl, E., Radinger, A.: *Seismic source characterisation of a Tunnel Boring Machine (TBM).* Geophysical Research Abstracts. Vol. 17, EGU2015-3749
2014	Geomechanik Kolloquium, Salzburg, Austria. Oral Presentation: *Consistent exploration by probe drilling and TSWD through the example of the Koralm tunnel.*
2014	SAGEEP- Symposium on the Application of Geophysics to Engineering and Environmental Problems, Boston, USA. Poster: Kreutzer, I., Radinger, A., Brückl, E., Chwatal, W., and Kostial, D: *TSWD – state of the art and current developments.* ID 17.
2014	EGU- European Geosciences Union, General Assembly in Vienna, Austria. Poster: Kreutzer, I., Chwatal, W., Radinger, A. and Brückl, E.: *The use of a Tunnel Boring Machine (TBM) as a seismic source*. Geophysical Research Abstracts. Vol. 16, EGU2014-3768
2010	16th European Meeting of Environmental and Engineering Geophysics; Near Surface EAGE, Zürich, Switzerland. Oral Presentation: Kreutzer, I., Freudenthaler, A.,: *Determination of the ice-thickness of the Brandner glacier in Vorarlberg, Austria.*

Publications:

2014	Radinger, A., Fasching, F., Pack, G., Kreutzer, I., Kostial, D. (2014): *Consistent exploration by probe drilling and TSWD through the example of the Koralm tunnel.* Geomechanics and Tunnelling, Volume 7, No.4:540–550.
2014	Kreutzer, I., Radinger, A., Brückl, E., Chwatal, W., Kostial, D (2014). *TSWD – State of the art and current developments.* Expanded Abstracts SAGEEP 2014 ID17.
2013	Freudenthaler, A., Chwatal, W., Kreutzer, I., Kompein, N., (2013): *Looking ahead of the face with TSWD.* Tunnelling Journal, Feb/March 2013, p. 42-45.
2012	Kreutzer, I., Chwatal, W., Eichiner, H., Kostial, D., Freudenthaler, A., Radinger, A., Larcher, M. (2012): *Tunnel Seismic While Drilling TSWD als unterstützendes Tool für die geologische Tunnelprognose - Entwicklung und Fallbeispiele.* In PANGEO Austria 2012 Abstracts, page 82.